Title
Diffusionally-accommodated Grain Boundary Sliding: Effects on Seismic Wave Attenuation

Permalink
https://escholarship.org/uc/item/49s1m3wt

Author
Lee, Lik Chuan

Publication Date
2010

Peer reviewed|Thesis/dissertation

Diffusionally–accommodated Grain Boundary Sliding: Effects on Seismic Wave Attenuation

by

Lik Chuan, Lee

A dissertation submitted in partial satisfaction of the
requirements for the degree of
Doctor of Philosophy

in

Mechanical Engineering

in the

GRADUATE DIVISION
of the
UNIVERSITY of CALIFORNIA at BERKELEY

Committee in charge:

Professor Stephen Morris, Co-chair
Professor Tarek Zohdi, Co-chair
Professor Barbara Romanowicz
Professor Jon Wilkening

Fall 2010

Diffusionally–accommodated Grain Boundary Sliding: Effects on Seismic Wave Attenuation

Abstract

Diffusionally–accommodated Grain Boundary Sliding: Effects on Seismic Wave Attenuation

by

Lik Chuan, Lee

Doctor of Philosophy in Mechanical Engineering

University of California at Berkeley

Professor Stephen Morris, Co-chair
Professor Tarek Zohdi, Co-chair

According to existing experiments on fine–grained polycrystalline mantle materials, in the seismic frequency band, mechanical loss Q^{-1} decreases with increasing angular frequency ω in an absorption background; roughly $Q^{-1} \sim \omega^\alpha$ with different investigators reporting values of α ranging from ~ -0.35 to ~ -0.2. There is inconclusive evidence that, under some conditions, a weak local maximum may be superposed on that absorption background. To understand this behaviour, we use a combination of analytical and numerical methods to analyze the Raj–Ashby bicrystal model of diffusionally–accommodated grain boundary sliding on a finite slope interface. In that model, two perfectly elastic layers of finite thickness are separated by a given fixed spatially periodic interface; dissipation is confined to that interfacial (grain boundary) region having an effective viscosity. It occurs by two processes: time–periodic shearing of the interfacial region; and time–periodic diffusion of matter along the interface. Two timescales govern these processes; namely, a characteristic time t_η taken for the interfacial shear stress to relax and a characteristic time t_D taken for matter to move by grain–boundary diffusion over distances of order the grain size.

Of particular interest is the case when the timescales are widely separated. Under that condition, we established two previously unrecognized features of the mechanical loss spectrum. First, the mechanical loss Q^{-1} in the seismic frequency band $\omega t_D \gg 1$ can be described by a strict power–law $Q^{-1} \sim \omega^\alpha$ if corners along the interface are geometrically

identical. For the two orthogonal sliding modes found in a regular array of hexagonal grains, the values of α is roughly -0.3. Second, our analysis reveals a mechanism allowing the magnitude of α to decrease slowly as ω is increased; when the corner angle varies from one corner to another along the interface , the rate of decrease in Q^{-1} gradually slows. Ultimately Q^{-1} is controlled by the corner having the most singular stress behaviour. Though these results are obtained from the idealized bicrystal model, we argue physically that similar behaviour will be found in numerical models of polycrystal. Overall, our analysis suggests that the range of α–values found empirically may, in part, reflect the differing ranges of ωt_D covered in different experiments.

Because in experiments conducted on certain materials, a weak and broad peak superposed onto the power–law absorption background is observed in the loss spectrum whereas in others, the peak is completely absent, we evaluate three proposed factors that may weaken and broaden the peak. We show that the peak can be weaken moderately by (i) sharpening of corners along the interface, (ii) spatial variation in grain size and (iii) spatial variation in interfacial (grain boundary) viscosity. Reduction of the peak by these factors, however, does not suggest it to be completely hidden in the absorption background. By contrast, we show that the loss peak can be markedly broadened if the interfacial viscosity differs by an order of magnitude across adjacent interfaces. The shape of the loss peak is insensitive to the other two factors.

Professor Stephen Morris
Professor Tarek Zohdi
Dissertation Committee Chair

This dissertation is dedicated to my wife, Didiana, and my parents for their constant support and encouragement.

Contents

List of Figures

List of Tables

Acknowledgements

I would like to thank my advisors, Professor Stephen Morris and Professor Tarek Zohdi, who have been unstinting in their support and guidance during my four years in Berkeley. This work will not be possible without their kind support and encouragement. I am grateful to Professor Jon Wilkening for all the helpful discussions and advice, especially for taking time off to explain his research to me. I also like to express my gratitude to Professor Barbara Romanowicz for agreeing to serve as my dissertation committee member.

Thanks also to my office–mates, George Mseis, Doron Klepach, Tim Kostka and Ryan Krone, who have made our office into a more hospitable and lively place to work in. They have been wonderful colleagues. Last but not least, I would also like to thank the many warm and helpful people in the departmental office, Donna Craig, Pat Giddings (who has retired), Shareena Samson and Yawo Dagbevi Akpawu.

Chapter 1

Introduction

1.1   Background

Knowledge of the physical conditions in the earth interior is essential to understand its dynamics. Because direct access of geophysical data is limited by depth of $\sim$ 200km, if we consider geological samples from volcanic eruption [20] (compared to the earth radius $\sim$ 6000km), seismic velocity tomography and seismic attenuation tomography are frequently used to infer conditions in the deep earth's interior. These techniques have been used to deduce physical conditions and chemical composition in the earth. For example, Ishii & Tromp [15] and Cammarano *et al.* [6] have used seismic data to determine, respectively, the density variation and the thermochemical structure in the earth's mantle while Shito *et al.* [39] have used attenuation tomography to determine water/hydrogen content in the mantle. In order to accurately constrain the physical and chemical conditions in the earth using seismic tomography, the effects of high–temperature viscoelasticity on seismic wave attenuation and seismic wave dispersion must be known.

High–temperature viscoelastic effects on the attenuation and dispersion of seismic waves manifest themselves in the form of a quality factor Q. Physically, the quality factor Q is defined as the ratio of 4π times the average stored energy to the energy dissipated per cycle in viscoelastic media [30]. The mechanical loss $\mathcal{L}$ is the inverse of the quality factor i.e Q^{-1}. When the attenuation is caused by thermally activated processes occurring in the earth interior, the mechanical loss Q^{-1}, in general, depends on temperature T, pressure P

and angular frequency ω through the expression [21]

$$Q^{-1} \propto \omega^{\alpha} \exp\left(\frac{\alpha H}{RT}\right). \tag{1.1}$$

In Eq. (1.1), H is the activation enthalpy that depends on pressure, R is the gas constant and α is a dimensionless exponent that governs the seismically observed power–law dependence of Q^{-1} to frequency ω i.e. $Q^{-1} \sim \omega^{\alpha}$. To infer physical and chemical conditions in the earth using seismic data, it is therefore necessary to know the temperature dependence of Q which in turn, requires knowledge of the physical mechanisms causing seismic waves to attenuate.

The quality factor Q, on the other hand, also affects seismic wave velocity c that is used to estimate the elastic properties of the earth. From Minster & Anderson [25], the elastic wave velocity c_0 is related to wave velocity c and the quality factor Q by

$$\frac{c}{c_0} = 1 - \frac{1}{2}\cot\left(\frac{\pi\alpha}{2}\right)Q^{-1}. \tag{1.2}$$

Because the elastic wave speed c_0 is a function of the mechanical properties of the medium through which seismic waves propagate, one can, in principle, improve the estimates on the earth elastic properties using measured seismic wave velocity c, if the global mapping of the quality factor Q^{-1} is known accurately.
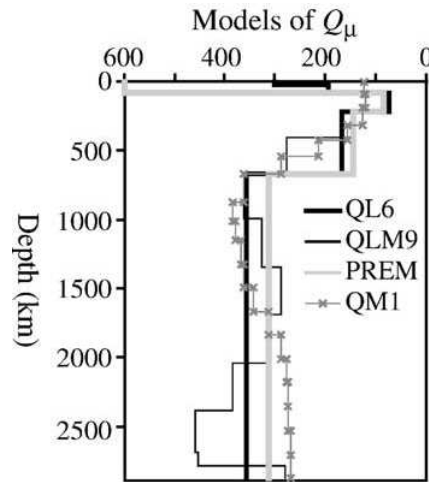
Figure 1.1: Q as a function of depth in Earth's mantle taken from Lawrence & Wysession [24]. Upper mantle: < 410km. Transition zone: $410 - 610$km. Lower mantle: > 610km.

Figure 1.1 shows the variation of the shear–wave quality factor Q with depth in the earth mantle where the different curves indicate the radial profiles of Q obtained using different models. From the figure, we find that the mechanical loss Q^{-1} in the upper mantle ranges between 0.005 to 0.01 and we also note that the lateral variation in Q can also be as large as the depth variation [14]. The frequency–dependent exponent α, on the other hand, is observed to lie within the range $-0.4 \leq \alpha \leq -0.2$ by Shito *et al.* [1] in the upper mantle.

Many different physical processes can give rise to seismic wave attenuation (or equivalently, produce high temperature viscoelastic behaviour). For example, an elastic wave can be attenuated by the local motion of point defects, by diffusional creep caused by bulk diffusion or grain boundary diffusion, by dislocation motion and by elastically–accommodated (or viscous) grain boundary sliding. Further details of these processes can be found in Karato [21] and Nowick & Berry [29].

To evaluate the contribution of these physical processes to seismic wave attenuation, experiments have been conducted on geological materials. According to the accepted "pyrolite" model by Ringwood [36], olivine $(Mg, Fe)_2SiO_4$ contributes nearly 60% of the mass in the upper mantle. Fine–grained polycrystalline olivine and its aggregates have been the subject of recent forced–torsional oscillation experiments at seismic frequencies e.g. Gribb & Cooper [13] and Jackson *et al.* [18]. Results from these experiments suggest that in the earth upper–mantle, attenuation of seismic wave may possibly be caused by elastically and diffusionally accommodated grain boundary sliding [18]. These results show a similar mild–frequency dependent behaviour of the mechanical loss Q^{-1} observed in the upper mantle. Extrapolating these results to mantle conditions also produce a level of attenuation Q^{-1} comparable to that observed in the upper mantle.

Though these experimental studies have attributed the mild–frequency dependent behaviour of the mechanical loss to elastically and diffusionally accommodated grain boundary sliding, these processes are still poorly understood and predictions using current theoretical models are inadequate to reconcile with experimental observations. Two prominent features in the attenuation experiments require reinforcements and/or supplements to the existing theories; (i) the mild–frequency dependence of the mechanical loss Q^{-1} and (ii) the presence of a dissipation peak in melt–bearing polycrystalline olivine.

Mild–frequency dependent behaviour of the mechanical loss Q^{-1} has been attributed to transient creep originating from diffusionally–accommodated grain boundary

sliding by Gribb & Cooper [13]. Its effects on the mechanical loss spectrum has been investigated recently by Morris & Jackson [26] using the Raj–Ashby bicrystal model [35] for a small–slope interface. In that model, two perfectly elastic grains are separated by a fixed spatially periodic interface where dissipation of energy occurs. It occurs by two processes; time–periodic shearing of interfacial region and time–periodic diffusion of matter along the interface. Morris & Jackson show that at frequencies corresponding to transient creep i.e. when diffusive transport is limited to distances smaller than grain size, the mechanical loss Q^{-1} decreases with frequency as $1/\ln \omega$. They show that the logarithmic behaviour of Q^{-1} is an outcome of corner stress concentrations. Though the loss scaling that they obtained is significantly milder than that observed in the experiments, where $Q^{-1} \sim \omega^{-(0.2-0.4)}$, that scaling is expected to change for a finite–slope interface because the behaviour of stresses near corner changes with corner angle. There is thus a need to evaluate the effects of slope angle on the mechanical loss spectrum due to diffusionally–accommodated grain boundary sliding.

The broad dissipation peak found in the mechanical loss spectrum of melt–bearing olivine that is absent in melt–free olivine has been attributed to dissipative time–periodic shearing of the interfacial region i.e. elastically–accommodated grain boundary sliding by Faul *et al.* [9]. Because the peak is observed even at temperature below the crystallization temperature of the melt, Faul *et al.* eliminate the possibility that the dissipation peak observed in their experiment is caused by grain–scale pressure–driven flow of melt i.e. melt–squirt. To explain this contrasting behaviour of the mechanical loss found in melt–free and melt–bearing olivine, they proposed that the dissipation peak is enhanced in melt–bearing polycrystal because corners at the triple junctions are rounded by melt which facilitates grain boundary sliding. In melt-free polycrystal, grain boundary sliding is inhibited by sharp corner at triple junctions and the peak weakened as a result. The peak thus becomes inconspicuous in the presence of the high temperature background. Current theoretical models are, however, insufficient to confirm Faul's explanation. Though a study using the bicrystal model of elastically–accommodated grain boundary sliding by Jackson *et al.* [16] suggests that the peak vanishes when corners become infinitely sharp, their study is limited to a small–slope interface. It is unclear as to whether a finite–slope interface will modify that conclusion. In order to assess Faul's explanation and any other factors that may help weaken the peak, it is necessary to extend the analysis of the bicrystal model of

elastically–accommodated grain boundary sliding to a finite–slope interface.

1.2 Objective

With these motivations, we solve here for the bicrystal model with finite–slope interface for diffusionally–accommodated and elastically–accommodated grain boundary sliding to study the effects of slope angle. There are two main purposes of this study, namely, (i) to give insights into the physical mechanisms controlling the mechanical loss spectrum found in the experiments, and (ii) to provide reliable solutions that can be used to verify numerical solutions for polycrystals.

1.3 Outline

We begin in chapter 2 with a survey of the results from relevant experiments that are compiled over the years showing evidence of diffusionally–accommodated and elastically–accommodated grain boundary sliding. These are attenuation experiments and creep experiments conducted using various materials, ranging from pure metals to geological materials. Theoretical models of grain boundary sliding are also discussed in the context of these experiments

In chapter 3, we state the boundary value problems (b.v.p.'s) of the bicrystal model for which we extend the analysis to a finite–slope interface. Specifically, the b.v.p.'s are stated for diffusionally–accommodated grain boundary sliding and elastically–accommodated grain boundary sliding.

In chapter 4, we discuss the numerical procedure used to solve the b.v.p.'s. Solving the b.v.p. of diffusionally–accommodated grain boundary sliding numerically is challenging, in particular, because the problem requires calculation of stress spatial derivatives along interface having corners. Due to the presence of corner stress concentration, numerical evaluation of stress derivatives will incur large errors and requires excessively fine mesh near corners. A fine mesh, on the other hand, requires a small time step if explicit methods are used. Consequently, a large number of iterations is required to compute the mechanical loss. To circumvent this difficulty, we reformulate the b.v.p. in the language of operators acting on functions defined on the grain boundary. The problem of finding the entire loss

spectrum for a given geometry is then reduced to one of finding the eigenvalues and the eigenfunctions of an evolution operator. To avoid issues caused by stress derivatives as stated above, these eigenvalues and eigenfunctions are found using a constructed pseudo–inverse of the evolution operator. By contrast, the b.v.p. of elastically–accommodated grain boundary sliding does not require calculation of the stress derivative and can be solved directly using conventional finite element method.

In chapter 5, we discuss the numerical results of diffusionally–accommodated grain boundary sliding from the bicrystal model. To verify our numerical results, we also derived analytical constraints of our numerical solution in that same chapter. These constraints are, namely, the high and low frequency asymptotes in the mechanical loss spectrum. We show that our numerical results are consistent with these constraints. Our results show that there exists a band of frequencies where the mechanical loss decreases slowly with frequency. That slowly–varying region is an outcome of corner stress concentration and the behaviour of the mechanical loss in that region is shown to be sensitive to slope angle. For the two orthogonal sliding modes found in a regular array of hexagonal grains, we predict the mechanical loss Q^{-1} to vary approximately as $\omega^{-0.3}$. Our results also show that the slope in the loss spectrum decreases with increasing frequency if corner angle varies along the interface. That result is consistent with the experiments.

In chapter 6, we discuss the numerical results of elastically–accommodated grain boundary sliding. We also derive constraints to the b.v.p. of elastically–accommodated grain boundary sliding and show that our numerical solution satisfy these constraints. We then evaluate three suggestions proposed to explain for the weakened and broadened loss peak observed in certain experiments. They are, namely, (i) variation in grain sizes d, (ii) variation in boundary viscosity η and (iii) sharp corners at triple junctions. We show that these proposed explanations are only able to account for a moderate reduction in peak height, and is unlikely to produce a large reduction necessary to completely conceal the loss peak within the absorption background. We also show that the loss peak can be significantly broaden by a variation in boundary viscosity η.

Finally in chapter 7, we summarize our chief findings of our analysis on the bicrystal model having finite–slope interface. We also discuss briefly possible future extensions of this work.

Chapter 2

Survey of experiments

Here, we survey experiments providing evidence of both elastically and diffusion-ally accommodated grain boundary sliding. These are attenuation and creep experiments conducted on metals, ceramics and geological materials. In the attenuation experiments, mechanical loss Q^{-1} is measured either by using a forced–torsional oscillation method e.g. in Gribb & Cooper [13], Schaller & Lakki [37] and Jackson *et al.* [18] or by using a torsion pendulum method e.g. in Kê [22] and Pezzotti *et al.* [32]. In forced–torsional oscillation method which allows robust measurement at frequencies of 10^{-3} – 1Hz [19] , an oscilla-tory torque is applied to the sample and its dynamic torsional modulus is obtained. The mechanical loss Q^{-1} is then the tangent argument of the modulus. By contrast in torsion pendulum method where robust measurements can be made within the range 1–30 Hz [31], the sample is allowed to vibrate freely and the logarithmic decrement δ is obtained. For small δ, the mechanical loss Q^{-1} is approximately equal to δ/π. Existing theoretical models and their predictions are also discussed here in relation to the experiments.

2.1   Elastically–accommodated grain boundary sliding

In theoretical models of elastically–accommodated grain boundary sliding, dis-sipation occurs in polycrystal due to shearing along the thin disordered grain boundary regions. Because these regions behaved like a thin layer of viscous fluid [2], interfacial shear stresses relaxed at a timescale t_η of order $\mu\ell/\eta d$; here d is the grain size, ℓ is the thickness of the disordered boundary region, μ is the rigidity of the grains and η is the

effective viscosity of the boundary region. Dissipation thus vanishes both at very low frequencies i.e. $\omega \ll t_\eta^{-1}$, and at very high frequencies $\omega \gg t_\eta^{-1}$ and the effect of elastically–accommodated grain boundary sliding manifests itself in the simple form of a dissipation peak in the mechanical loss spectrum. Though that peak is expected to be easily observed in experiments, that is not so; the peak has been observed clearly only in some experiments.

2.1.1 Experiments on pure metals

An example of a dissipation peak arising from elastically–accommodated grain boundary sliding can be found in the experiments by Kê [22] [23], who used torsion pendulum method to investigate the behaviour of mechanical loss Q^{-1} found in pure polycrystalline Al. To establish the effects of grain boundaries, he measured the mechanical loss Q^{-1} in polycrystalline Al and single crystal Al.
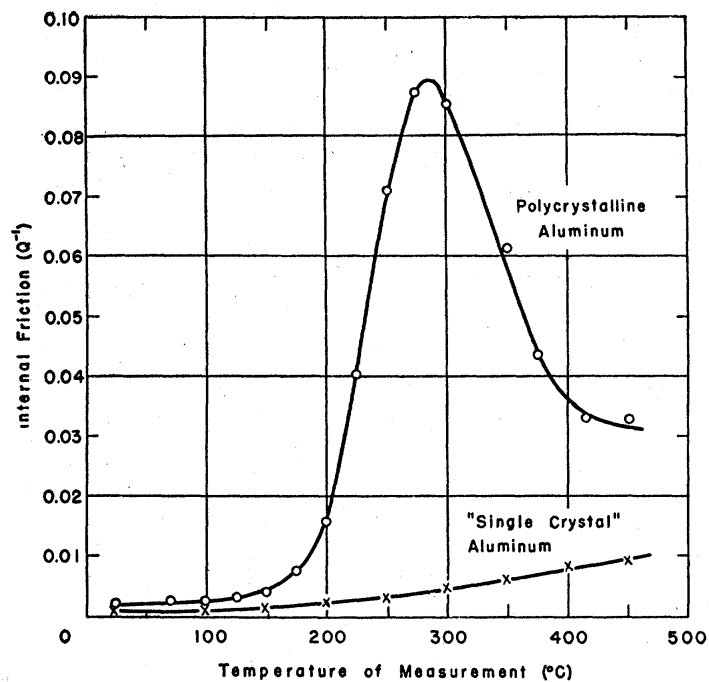
Figure 2.1: Q^{-1} as a function of T at 0.8Hz for Al taken from Kê [22].

Figure 2.1 shows the result from his experiment. In single crystal Al, the mechanical loss Q^{-1} increases exponentially with temperature T whereas the behaviour of Q^{-1} is non–monotonic with respect to T in polycrystalline Al. For the latter, the $Q^{-1} - T$

plot contains a strong Debye peak which he attributes to elastically–accommodated grain boundary sliding. That peak has a magnitude of about 0.09 and stands out from the absorption background. Because creep experiments conducted on the same polycrystalline samples show that dissipation is thermally activated, i.e. Eq. (1.1) applies, similar features are also expected to be found in the mechanical loss spectrum. To prove that the loss peak is not unique to Al, Kê also conducts experiment on pure Mg and he shows that a loss peak of ~ 0.06 is found in pure polycrystalline Mg.

2.1.2 Experiments on ceramics–based materials

Subsequent experiments conducted on ceramics, however, do not show a pronounced peak in the mechanical loss spectrum that is observed in pure metals. Instead, the mechanical loss spectrum is described by Cooper [8] in his review to contain "a broad absorption peak of low magnitude in the polycrystalline material, one barely 'competing' to be seen over the power–law background absorption". Behaviour of the mechanical loss fitting such a description can be found in ceramic–based materials e.g. Si_3N_4 by Pezzotti *et al.* [32], Al_2O_3 and MgO by Pezzotti [31] and Barnhoorn *et al.* [3], and Zirconia ZrO_2 by Schaller & Lakki [37]. [1]

Figure 2.2 shows an example of the Cooper's description of a "broad absorption peak of low magnitude" found in MgO from Pezzotti [31]. In his experiment (as well as those in Schaller & Lakki), the peak is isolated by subtracting the experimental curve from the absorption background and is studied separately. This procedure is shown in the figure. In comparison with the loss peak found in pure metals by Kê, the peaks found in ceramic–based materials are located at a higher temperature (~ 1600*K*) and do not stand out from the absorption background. These peaks are also broader than the single Debye peak found in pure metals discussed above.

2.1.3 Experiments on melt–bearing geological materials

A weak and broad mechanical loss peak has also been observed in geological materials at seismic frequencies (~ 10^{-3}Hz to 1 Hz) and elevated temperature (~ 1300*K*) by

---

[1]The experiments by Schaller & Lakki [37] on 3 types of ceramics consistently show a mild and broad absorption peak. However, only in the case of Zirconia, was the peak attributed to viscous grain boundary sliding
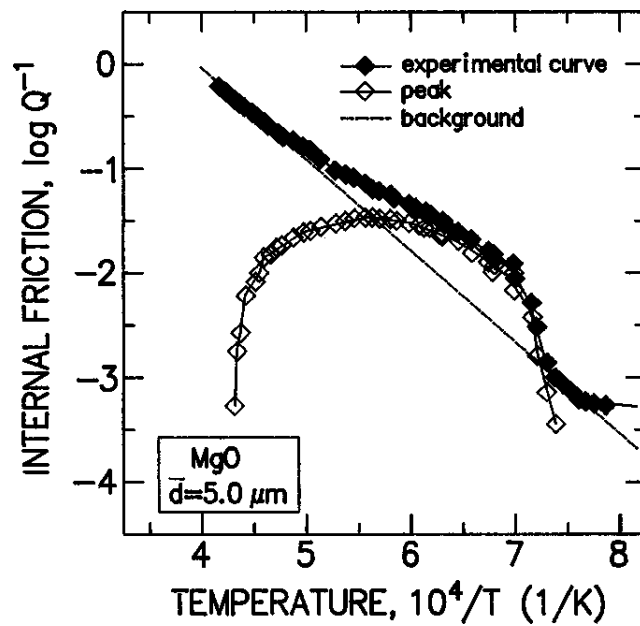
Figure 2.2: Q^{-1} as a function of T for MgO at 13Hz taken from Pezzotti [31].

Jackson *et al.* [17]. In fine–grained melt–bearing polycrystalline olivine $(Mg,Fe)_2SiO_4$ speci-mens prepared from natural olivine and sol–gel derived Fo_{90} precursors, a peak superposed onto the absorption background in the mechanical loss spectrum is consistently observed. By contrast, the peak is absent in the loss spectrum obtained from melt–free polycrystalline olivine, where the mechanical loss decreases monotonically with frequency. The results of melt–free polycrystalline olivine are discussed later. Because the peak, as discussed in chapter 1, is observed even at temperatures below the crystallization temperature of melt, and its height is significantly larger than that predicted for grain–scale pressure–driven flow or melt–squirt, Faul *et al.* [9] eliminate melt–squirt as a possible mechanism causing the peak. Instead, they attribute the peak to elastically–accommodated grain boundary sliding.

Figure 2.3 shows the mechanical loss behaviour for one of the melt–bearing spec-imen found in the experiments by Jackson *et al.* [17]. Similar to ceramics discussed above, the superposed peak found in the figure is broad and does not stand out from the absorp-tion background. We note here that in forced–torsional oscillation experiments conducted on fine–grained peridotite (fabricated using natural dunite and orthopyroxene) with a melt fraction of ~ 0.015 by Sundberg & Cooper [40], they too observed a non–monotonic be-
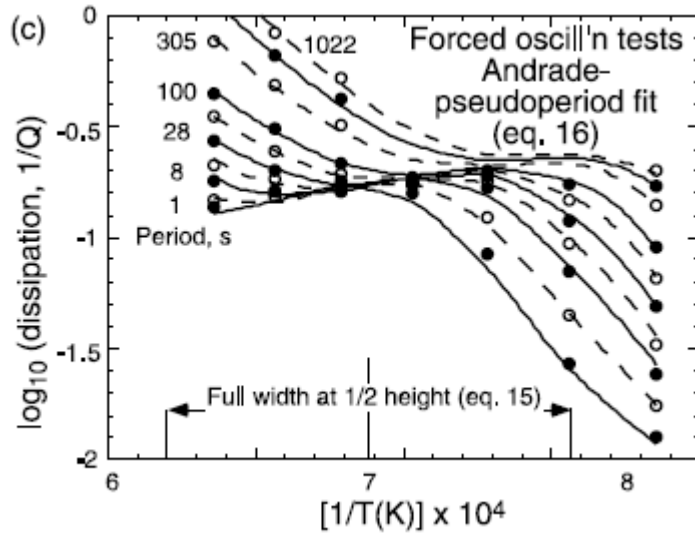
Figure 2.3: Q^{-1} as a function of T for melt–bearing $(Mg,Fe)_2SiO_4$ taken from Jackson *et al.* [17]. Melt fraction: 0.037. Sol–gel specimen.

haviour of the mechanical loss spectrum resembling the inception of a loss peak. They attribute that non–monotonic behaviour to elastically accommodated grain boundary sliding.

2.1.4 Relating experiment to theory

Several suggestions have been proposed to explain the broader and weaker peak found in other materials as opposed to the single Debye peak observed in pure metals, which is well–predicted by existing theoretical models e.g. Ghahremani [12]. These suggestions can be categorized into two broad classes: (i) grain–wise variation of parameters controlling the timescale t_η taken for shear stress to relax and (ii) grain boundary geometry.

In the first case, a broader and weaker dissipation peak is envisaged to be caused by a widely distributed sliding timescale t_η that is due to a variation in grain size d and a variation in boundary viscosity η suggested by Pezzotti [31] and Cooper [8], respectively. For the latter, η is an intrinsic viscosity, as explained by Ashby [2], that depends on the degree of misalignment between adjacent grain lattices at the boundary interfaces. The intrinsic viscosity η is used to model the effects of elastically–accommodated grain boundary sliding and is measured indirectly in experiments using the Debye peak found in the loss

spectrum. That viscosity is not to be confused with a viscosity ascribed to the presence of an amorphous silicate (e.g. SiO_2 in Pezzotti *et al.* [32]) found in grain boundaries of e.g. Si_3N_4. Unlike the intrinsic boundary viscosity, the viscosity of the amorphous silicate residing along the grain boundaries can be measured independently of the attenuation spectrum. We also note that because the viscosity of the amorphous silicate does not vary along grain boundaries, it cannot produce a variation in timescale t_η described by Cooper [8].

The second class of explanation concerns geometrical features that physically affect sliding across grain boundaries. Faul *et al.* [9] suggest that the loss peak may be weakened if corners at the triple junctions are sharp. Comparing triple junctions found in their melt–bearing and melt–free polycrystalline olivine samples, they observed that the junction corners are significantly rounded when melt is present, as opposed to the tight corners found in their melt–free samples. Because the loss peak is absent in their melt–free polycrystalline olivine sample as discussed in §2.1.3, they proposed that the peak is significantly weakened and is concealed in the absorption background when sliding across grain boundaries is inhibited by the sharp triple junction corners. This result is also broadly consistent with the results found in existing theoretical models. In an analysis of the Raj–Ashby bicrystal model using a small–slope interface by Jackson *et al.* [16], they show that the loss peak vanishes as corners become infinitely sharp. In chapter 6, we evaluate the sensitivity of the loss peak to these proposed factors.

2.2 Diffusionally–accommodated grain boundary sliding

In diffusionally–accommodated grain boundary sliding, dissipation occurs in polycrystal due to the transport of matter along grain boundaries from regions under compression to regions in tension. To accommodate that transfer of atoms, grain boundaries slide relative to one another at a characteristic time t_D taken for matter to be transported across distances of order the grain size. A polycrystal therefore creeps at a constant rate determined by a creep viscosity η_{ss} only after a time $t \gg t_D$ has lapsed upon which a constant load is applied. Note that the creep viscosity η_{ss} is not to be confused with the boundary viscosity η discussed previously. Correspondingly, that steady–state creep behaviour is translated into an inverse relation between mechanical loss and frequency i.e. $Q^{-1} \sim \omega^{-1}$

when a time–periodic load is applied at frequencies $\omega \ll t_D^{-1}$.

2.2.1 Experiments on geological materials

Steady–state creep behaviour is however, not observed in the attenuation experiments conducted on geological materials. Instead, a mild frequency–dependent absorption background in the mechanical loss spectrum has been observed consistently in fine grained $O(\mu m)$ geological materials deforming under small strain $O(10^{-6})$ at seismic frequencies and elevated temperature $\sim 1300K$. In forced–torsional oscillation experiments conducted on olivine aggregates fabricated from natural material, specifically peridotite by Sundberg & Cooper [40] and dunite ($> 90\%$ olivine) by Gribb & Cooper [13] and Bunton [5], the mechanical loss Q^{-1} is observed to vary approximately as $\omega^{-0.35}$ in the absorption background.[2] By comparison, a slightly milder frequency–dependent absorption background $Q^{-1} \sim \omega^{-0.26}$ is also observed in the experiment by Jackson *et al.* [18] using melt–free polycrystalline olivine specimens prepared from both natural olivine and sol–gel derived Fo_{90} precursors. Because the grain size d is kept small $\sim O(\mu m)$ in these experiments to exclude any effects caused by dislocations (and to prevent microcracking in the specimens), the mild–frequency dependent absorption background is attributed by the different investigators to diffusional creep originating from grain boundary diffusion.

Figure 2.4 shows the mechanical loss spectra obtained in these experiments obey the similarity principle dictated by diffusional creep stated in Gribb & Cooper [13]: if the behaviour of the mechanical loss Q^{-1} is controlled solely by diffusional creep, Q^{-1} should depend on steady state creep viscosity η_{ss}, grain rigidity μ and the angular frequency ω through a single dimensionless variable $\omega\eta_{ss}/\mu$. From the figure, we find that the mechanical loss Q^{-1} measured in the different experiments described above collapse onto a single curve defined by a power law $Q^{-1} \sim (\omega\eta_{ss}/\mu)^{\alpha}$, albeit with some scatter in the data. The cause of that scatter is discussed later.

In the figure, the steady–state creep viscosity η_{ss} used to normalize the frequency ω for the data from Bunton [5] and Sundberg & Cooper [40] is measured using torsional microcreep test on the same specimens used in their attenuation experiments. By contrast, the creep viscosity η_{ss} used to graph the data from Jackson *et al.* [18] is calculated using Eq.

---

[2]Note: In these experiments, the melt content is not reported except in the case of Sundberg & Cooper, where they reported a modest melt fraction of ~ 0.015 in their specimens.
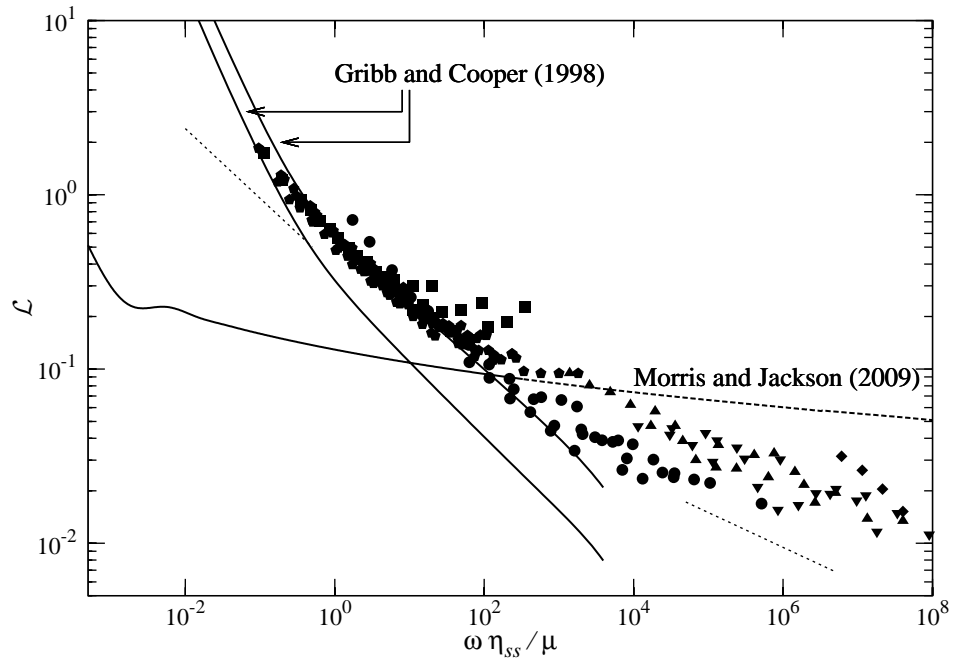
Figure 2.4: Mechanical loss spectrum of the experiments. Jackson *et al.* [18]: • 2.9μm, △ 12.4μm, 30 ▼ 23.4μm, ◊ 165.1μm. Bunton [5] ×. Sundberg & Cooper [40] ■. Broken lines have slopes -0.2 and -0.4. Solid lines: Prediction by Gribb & Cooper [13] and Morris & Jackson [26]. Refer to text for explanation.

(6) in Morris & Jackson [27]. That equation describes a relation between creep viscosity η_{ss}, grain size d and temperature T that is obtained by fitting the results of a separate uniaxial compression microcreep test on fine–grained (3–6 μm) polycrystalline olivine aggregates given in Faul & Jackson [10]. We note that the result in the microcreep experiments showing creep rate $\dot{e}$ varying as the third power of grain size i.e. d^3 supports the argument that the dominant dissipative mechanism operating in these attenuation experiments is grain boundary diffusion.

As explained in Morris & Jackson [27], the scatter found at high frequencies is, in fact, a systematic offset in $\omega\eta_{ss}/\mu$ of the data from Jackson *et al.* [18] corresponding to different grain sizes. They suggest that the offset is a systematic error introduced when using the fit given by their Eq. (6) to extrapolate the creep viscosity η_{ss} to larger grain sizes. The scatter found in the data from Sundberg & Cooper [40] at $\omega\eta_{ss}/\mu \sim 10^2$ is attributed by them to be the inception of a loss peak caused by elastically–accommodated grain boundary sliding as discussed below Figure 2.3.

From the figure, the power–law exponent α has different values depending on the frequency range. As indicated by the broken lines, the value of α varies from ~ -0.4 to ~ -0.2 as frequency ω is increased. This range of exponent α is comparable with that observed in the earth upper mantle [1]. In chapter 5, we show that this gradual decrease in slope may, in part, be caused by a variation of triple junction corner angles in polycrystals.

2.2.2 Relating experiment to theory
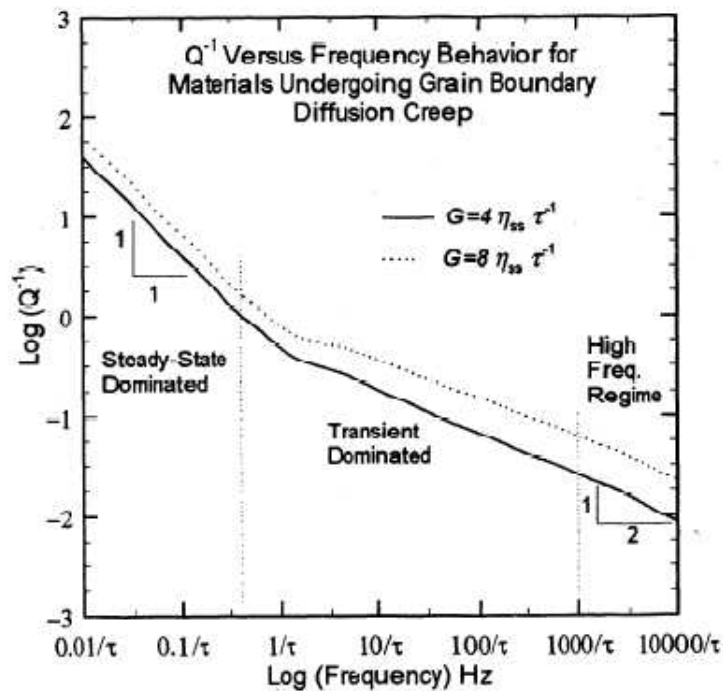
Figure 2.5: Mechanical loss spectrum predicted by Gribb & Cooper [13]. Refer to text for explanation

The Raj–Ashby bicrystal model of diffusionally–accommodated grain boundary sliding has been used by Gribb & Cooper [13] to interpret the results from their experiment. Following Raj's approach [34] of using a perturbation method, they calculate the creep rate $\dot{e}$ as a function of time t for a truncated sawtooth interface with slope angle $\varphi = 60°$. In their calculation, they used the resultant interfacial normal stress σ_{nn} when the interfacial shear stresses are fully relaxed under elastically–accommodated grain boundary sliding as an initial condition to compute the creep rate i.e. they assumed grain boundary diffusion proceeds only upon the completion of elastically–accommodated grain boundary sliding.

By time–integrating the creep rate $\dot{e}$ and applying numerical Laplace transform to the resultant creep response $e(t)$, they obtain the frequency–response of the mechanical loss Q^{-1}.

Figure 2.5 shows the prediction of the mechanical loss spectrum by Gribb & Cooper [13]. Their predicted spectrum contains 3 distinct regions, namely, a steady–state regime in the low frequencies where $Q^{-1} \sim \omega^{-1}$, a transient regime at intermediate frequencies and a high–frequency regime where $Q^{-1} \sim \omega^{-0.5}$. In the transient regime, the mechanical loss Q^{-1} decreases slowly and varies as $\omega^{-(0.25-0.4)}$. According to Gribb & Cooper, the differing values of the exponent in the power–law description of the transient regime reflects an error that arises when extrapolating their small–slope perturbation solution to a finite–slope interface as described in Raj's calculation [34].

To evaluate the prediction by Gribb & Cooper in terms of the attenuation experiments, we digitized their curves given in Figure 2.5 and rescale the frequency with the dimensionless variable $\omega\eta_{\mathrm{SS}}/\mu$. The steady state creep viscosity η_{SS} used to rescale the frequency is obtained from Raj & Ashby calculation of the steady state creep rate for a 2-D hexagonal array of grains [35]. According to Gribb & Cooper, the creep viscosity η_{SS} is related to the timescale τ found in Figure 2.5 by $\tau \approx 4\eta_{\mathrm{SS}}/\mu$. These curves are graphed with the experiments using solid lines in Figure 2.4. In the figure, we find that their prediction is close to the experiments in the frequency range $10^0 \leq \omega\eta_{\mathrm{SS}}/\mu \leq 10^3$. At higher frequencies i.e. $\omega\eta_{\mathrm{SS}}/\mu > 10^3$, their prediction of the power–law behaviour $Q^{-1} \sim \omega^\alpha$ starts to deviate from the experiments; α increasing to -0.5 in their prediction whereas α decreases to roughly -0.2 in the experiments. At low frequencies i.e. $\omega\eta_{\mathrm{SS}}/\mu \sim 10^0$, results from the attenuation experiments start to deviate from the prediction by Gribb & Cooper. Specifically, the results from the experiments do not exhibit a sharp transition between steady–state regime and the transient regime predicted by them.

The prediction by Gribb & Cooper [13] is different from the prediction by Morris & Jackson [26] who also analyze the bicrystal model using a perturbation method that is accurate only for a small–slope interface. Unlike Gribb & Cooper who transform the time–response of the bicrystal model deforming under creep to obtain its frequency–response i.e. mechanical loss spectrum, they solve for the spectrum directly by imposing a time–periodic displacement at the boundaries of the model. For a small–slope interface, they predict the mechanical loss Q^{-1} to vary as $1/\ln\omega$ at frequencies $\omega \gg t_D^{-1}$. That scaling is independent

of the interface type and is shown in Figure 2.4. They also show that the logarithmic scaling is an outcome of corner stress concentration where $\sigma_{nn} \sim r^{-1}$ near corners; here r is the distance measured away from the corner along the interface. Because the behaviour of the interfacial normal stress σ_{nn} is predicted to change with interface slope angle by a local analysis of Picu & Gupta [33], the logarithmic scaling does not hold for a finite–slope interface. We show in chapter 5 that our numerical results for small–slope interfaces agree with that from the perturbation solution of Morris & Jackson [26] and the loss scaling is, indeed, sensitive to the slope angle at frequencies $\omega \gg t_D^{-1}$.

Comparing the prediction by Morris & Jackson [26] to that from Gribb & Cooper [13], we find that the mechanical loss Q^{-1} is more sensitive to frequency ω in the latter's prediction. The high–frequency regime loss scaling $Q^{-1} \sim \omega^{-0.5}$ is also not predicted by Morris & Jackson. Given that both predictions are obtained from a perturbation analysis that assume the solution as a power–series of interface slope to the same order, we expect the mechanical loss Q^{-1} computed from the two solutions to behave similarly in the spectrum even though different slope angles are used; the slope angle should cancel off in the calculation of Q^{-1} which is the tangent argument of the model shear modulus G.
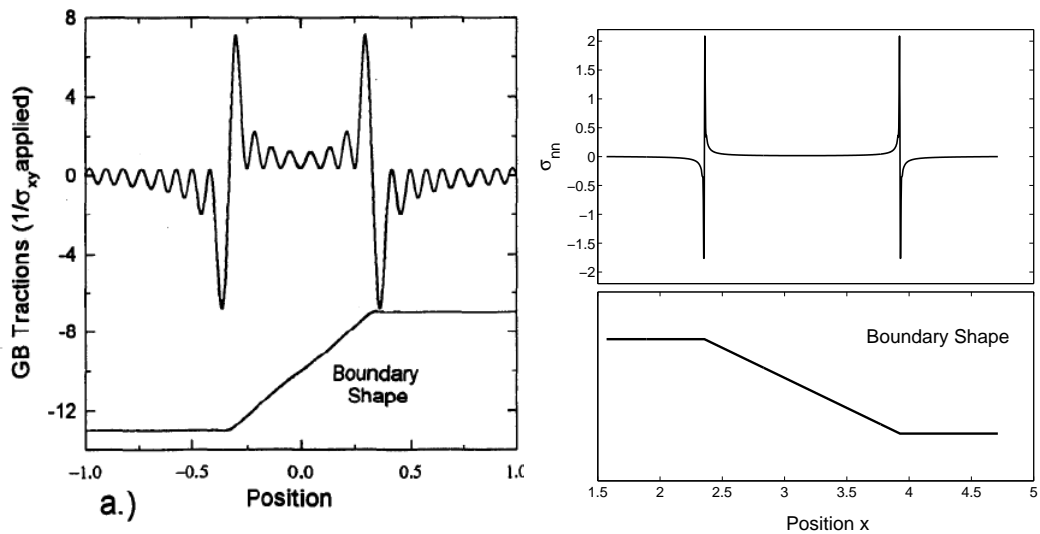
(a) Gribb & Cooper   (b) Morris & Jackson

Figure 2.6: Comparison of interfacial normal stress σ_{nn} in Gribb & Cooper's [13] and Morris & Jackson [26]. Morris & Jackson: Eq. (24) $\omega = 10^8, N = 1000$. Refer to text for explanation

There is one inconsistency, however, between the normal interfacial stress $\sigma_{nn,\,\omega\to\infty}$ found in the solution of Morris & Jackson at high frequency extreme and the stress $\sigma_{nn,\,t=0}$ used to initiate the creep response calculation by Gribb & Cooper. In order for the predictions to be consistent with one another, $\sigma_{nn,\,\omega\to\infty}$ must be equal to $\sigma_{nn,\,t=0}$ and should serve as an initial condition for the creep response calculation. However, that is not so.

Figure 2.6 shows the initial stress distribution $\sigma_{nn,\,t=0}$ used in Gribb & Cooper's calculation and the stress distribution from Morris & Jackson [26]. The oscillation is an artifact from the Fourier series approximation of the truncated sawtooth interface. Compared to the prediction by Morris & Jackson where the normal stress $\sigma_{nn,\,\omega\to\infty} \sim r^{-1}$ near corners, we find that $\sigma_{nn,\,t=0}$ does not exhibit that singularity behaviour near corners. Note in Figure 2.6b, $\sigma_{nn} \sim r^{-1}$ only at distance $r \gg \omega^{-1/3}$ measured from the corners for finite frequencies. The behaviour of $\sigma_{nn,\,t=0}$ is significantly weaker. This disparity between $\sigma_{nn,\,\omega\to\infty}$ and $\sigma_{nn,\,t=0}$ may be a possible cause for that discrepancy between the prediction by Morris & Jackson [26] and Gribb & Cooper [13] We show later that a weaker stress concentration is, in fact, translated to a stronger frequency–dependent behaviour of Q^{-1} that is consistent with the differences between the two analysis.

Chapter 3

Boundary value problems of the bicrystal model

B.v.p.'s of diffusionally–accommodated grain boundary sliding and elastically–accommodated grain boundary sliding are now formulated. Here and subsequently, we use asterisks to denote dimensional variables.
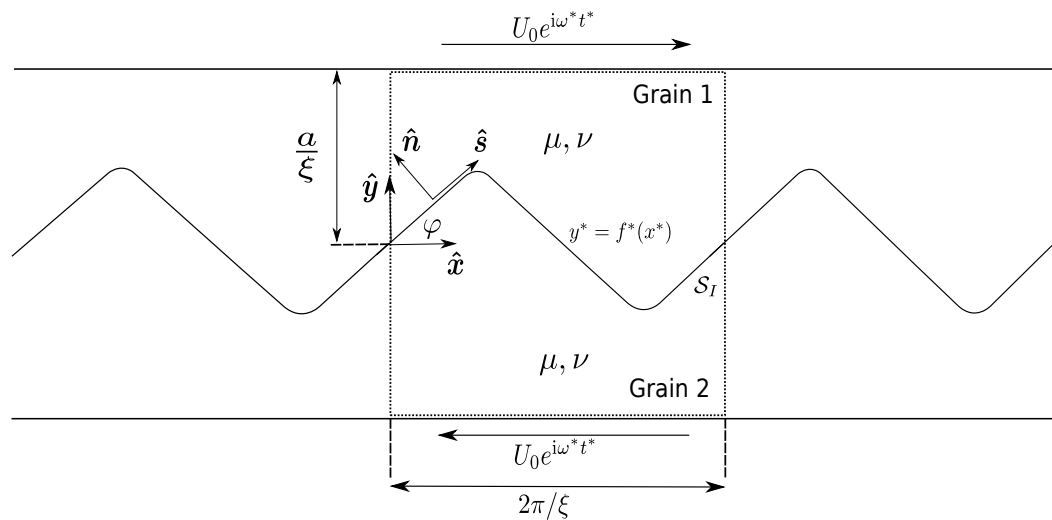
Figure 3.1: Model schematic

Figure 3.1 shows the geometry of the bicrystal model. The sample consists of two linear elastic grains having elastic shear modulus μ and Poisson ratio ν. The interface is periodic with a wavelength $2\pi/\xi$, where $\xi \sim 1/d$ is the wavenumber. We assume

the interface position to be a given time–independent function $f^*(x^*)$ because the strains occurring in the attenuation experiments are small in order to model the propagation of seismic wave. Unit vectors in the coordinate directions are denoted by $\hat{x}$ and $\hat{y}$. The unit tangent and unit normal vectors of the interface are denoted by $\hat{s}$ and $\hat{n}$, respectively. At the upper and lower boundaries at $y^* = \pm a/\xi$, the displacement varies sinusoidally in time t^* with angular frequency ω^* and amplitude U_0, i.e. $\boldsymbol{u}^* = \hat{x}U_0 e^{i\omega^* t^*}$. The grains are assumed to be undergoing plane deformation and the x and y components of the displacement vector $\boldsymbol{u}^*$ are denoted by $u_1^*(x^*, y^*)$ and $u_2^*(x^*, y^*)$, respectively. Similarly, the Cartesian components of the stress and strain tensors (i.e. $\boldsymbol{\sigma}$ and $\boldsymbol{e}$) are denoted by $\sigma_{ij}^*(x^*, y^*)$ and $e_{ij}^*(x^*, y^*)$.

There are two rate-dependent constitutive equations on the grain boundary $\mathcal{S}_I$. The first constitutive equation is given in (3.1) and describes the viscous sliding along interface $\mathcal{S}_I$ caused by the presence of a boundary phase. In that equation, the interfacial shear stress σ_{ns}^* is proportional to the discontinuity in tangential velocity $[\dot{u}_s^*]$ across $\mathcal{S}_I$ and is given by

$$\ell \sigma_{ns}^* = \eta \left[\dot{u}_s^* \right] . \tag{3.1}$$

Here, ℓ and η are, respectively, the thickness and the viscosity of the interface; both assumed to be constant. We note that constitutive equation (3.1) is analogous to that of Couette flow and the interface $\mathcal{S}_I$ therefore acts as if it contains a thin film of Newtonian fluid.

The second constitutive equation describes the effects of grain boundary diffusion. Volumetric flow rate (per unit z–length) along the interface j^* occurs in the presence of a normal stress gradient $d\sigma_{nn}^*/ds^*$. From Fick's first law, this flow rate is given by

$$j^* = \frac{V\ell D}{kT} \frac{d\sigma_{nn}^*}{ds^*} , \tag{3.2}$$

where matter flows from region under compression to region in tension along the interface $\mathcal{S}_I$. Balancing mass along the interface i.e.

$$[\dot{u}_n^*] + \frac{dj^*}{ds^*} = 0 , \tag{3.3}$$

leads to the final form of the constitutive equation for grain boundary diffusion that is given by

$$[\dot{u}_n^*] + \frac{V\ell D}{kT} \frac{d^2\sigma_{nn}^*}{ds^{*2}} = 0 . \tag{3.4}$$

Because time–derivatives enter these two constitutive equations i.e. Eq. (3.1) and (3.4), we can define two timescales t_η and t_D from them. Following Mosher & Raj [28] and

Parameters	Values	References
Temperature T	$1500K$	
Grain size d	5μm	Jackson *et al.* [17]
Grain rigidity μ	0.05TPa	
Grain boundary thickness ℓ	1 nm	
Frequencies $\omega/2\pi$	$10^{-3} - 1$ Hz	
Steady–creep viscosity η'	50 TPa s	Faul & Jackson [10];
		Morris & Jackson [27]
Molecular volume v	0.05 nm^3	Frost & Ashby [11]
Diffusivity ℓD	10^{-23}m^3/sec	Eq. (14) in Coble [7]: $\eta' = \frac{1}{148}\frac{d^3kT}{\ell Dv}$
Diffusive timescale t_D	10^5 sec	
Diffusive lengthscale ℓ_d	$0.05 - 0.5\ \mu$m	

Table 3.1: Estimates of diffusive timescale t_D and lengthscale ℓ_d based on Mg$_2$SiO$_4$. Refer to text for explanation.

Raj [34], the timescales are defined as:

$$t_\eta = \frac{\eta}{\xi\ell\mu}\,, \qquad t_D = \frac{kT}{\mu V\ell D\xi^3}. \qquad (3.5a, b)$$

Physically, t_η and t_D are the timescales on which the two sides of (3.1) and (3.4) balance. In Eq. (3.5b), the terms balance if the derivative along the interface scales with its wavelength. Thus at high frequencies i.e. $\omega \ll t_D^{-1}$, diffusion only operates within a distance that is small compared with the wavelength. At a given frequency ω, the effects of diffusion on an interface with sharp corners is then limited to within a distance ℓ_d measured away from the corner given by

$$\ell_d = \left(\frac{\mu V\ell D}{kT\omega}\right)^{1/3}. \qquad (3.6)$$

In Table 3.1, we estimate the diffusive timescale t_D and the diffusive distance ℓ_d in the attenuation experiments. From the table, we find that the diffusive lengthscale ℓ_d is at least order of magnitude smaller than the grain size. Consequently, diffusion does not occur at a grain–scale level in the attenuation experiments.

We now define the following dimensionless variables (without asterisks):

$$(x^*, y^*) = (x, y)/\xi\,, \qquad (3.7a)$$

$$\boldsymbol{u}^* = U_0\boldsymbol{u}\,, \qquad (3.7b)$$

$$f^* = \varepsilon f / \xi \,, \tag{3.7c}$$

$$\sigma^*_{ij} = \mu \xi U_0 \sigma_{ij} \,, \tag{3.7d}$$

$$t^* = t_D t \,. \tag{3.7e}$$

In Eq. (3.7c), ε is the characteristic slope of the interface.

The dimensionless b.v.p. of diffusionally–accommodated grain boundary sliding is stated as follows:

in grain 1 and grain 2 ,

$$\nabla(\nabla \cdot \boldsymbol{u}) + (1 - 2\nu)\nabla^2 \boldsymbol{u} = 0 \,; \tag{3.8a}$$

on $y = \pm a$,

$$u_1 = \pm e^{i\omega t} \,, \tag{3.8b}$$

$$u_2 = 0 \,; \tag{3.8c}$$

on $y = \varepsilon f(x)$,

$$\mathcal{M}[\dot{u}_s] = \sigma_{ns} \,, \tag{3.8d}$$

$$[\dot{u}_n] + \frac{\mathrm{d}^2 \sigma_{nn}}{\mathrm{d}s^2} = 0 \,; \tag{3.8e}$$

$$[\sigma_{ns}] = 0 = [\sigma_{nn}] \tag{3.8f, g}$$

on $x = 2\pi$ and $x = 0$,

$$u_1(0, y) = u_1(2\pi, y) \,, \tag{3.8h}$$

$$u_2(0, y) = u_2(2\pi, y) \,. \tag{3.8i}$$

In (3.8d), the viscosity parameter $\mathcal{M}$ is defined as

$$\mathcal{M} = t_\eta / t_D \,. \tag{3.9}$$

When $\mathcal{M} \to 0$ (for fixed frequency), the interface $\mathcal{S}_I$ becomes effectively inviscid on the interface i.e. $\sigma_{ns} = 0$ and dissipation occurs solely through grain boundary diffusion.

Conversely when there is no diffusion, energy is dissipated solely through the boundary viscosity η. This specific case is referred to as elastically–accommodated grain

boundary sliding described below §2.1. For this case, the normal displacement u_n becomes continuous across the interface $\mathcal{S}_I$ and Eq. (3.8e) is replaced by

$$[u_n] = 0. \tag{3.10a}$$

Rescaling time t with the sliding timescale t_η by setting $\mathcal{M} = 1$, Eq. (3.8d) becomes

$$[\dot{u}_s] = \sigma_{ns}. \tag{3.10b}$$

Eq. (3.8a) – (3.8c), (3.8f) – (3.8i) and (3.10) thus form the b.v.p. of elastically–accommodated grain boundary sliding for the bicrystal model.

Because the elastic wavelength for our frequencies of interest is large compared to the sample size, we used the plane elastostatic equation in (3.8a) instead of the dynamical equation. With a grain interface $\mathcal{S}_I$ that is fixed in time, problem (3.8) is then linear and separable in time. Consequently, the solution to (3.8) for a time–periodic boundary displacement is also time–periodic with the same angular frequency ω.

Because the constitutive equations (3.8d) and (3.8e) contain time derivatives, the displacements within the sample lag the displacements imposed at the sample boundaries. Consequently, the stress at the boundary lags the displacement there. That resulting phase lag between the imposed boundary displacement and the resultant boundary stress is an expression of dissipation occurring at the interface $\mathcal{S}_I$.

By solving the b.v.p.'s (diffusionally and elastically accommodated grain boundary sliding), we are able to obtain the x–averaged shear stress τ applied at $y = \pm a$. The averaged shear stress τ is defined as

$$\tau(t) = \frac{1}{2\pi} \int_0^{2\pi} \sigma_{xy}(x, a, t) \, dx. \tag{3.11}$$

The sample shear modulus G is then defined by the equation:

$$G = \tau(t)/\gamma(t), \tag{3.12}$$

where $\gamma(t) = e^{i\omega t}/a$ is the sample shear strain. Because both τ and γ are proportional to $e^{i\omega t}$ in (3.12), the modulus G is independent of t and is a function of frequency ω.

The mechanical loss $\mathcal{L}$ is defined, as usual, by the equation

$$\mathcal{L} = \tan \arg G. \tag{3.13}$$

We note that $\mathcal{L}$ is a dimensionless quantity. If the material can be modelled as a network of springs and dampers, the quantity defined by (3.13) is equal to the ratio of the loss per cycle to 4π times the mean strain energy stored within the grains (see O'Connell & Budiansky [30] and Bland [4]).
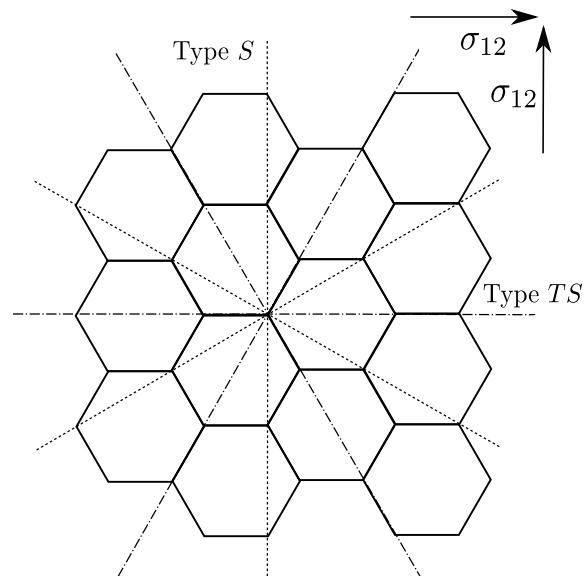
(a) Array of hexagonal grains
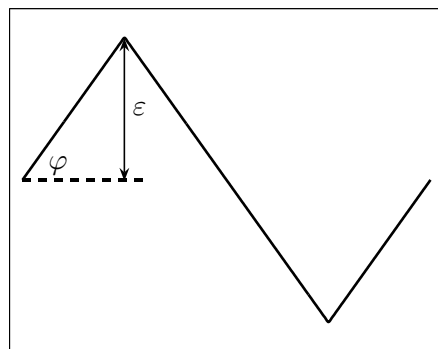
(b) Type *S* interface
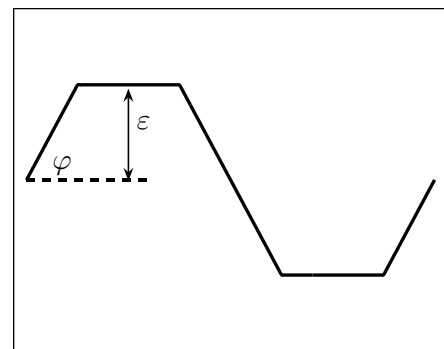
(c) Type *TS* interface

Figure 3.2: Polycrystal microstructure idealized as an array of hexagonal grains

We consider the type S interface and the type TS interface shown in Figure 3.2. These interfaces correspond to two orthogonal sliding surfaces found in an array of regular hexagonal grains. Corners of the interface are rounded over a distance $r_c < d$ and we define N as the ratio of the interface wavelength d with the corner radius r_c so that

$$N = \frac{d}{r_c} \,. \tag{3.14}$$

When interfaces have sharp corners (i.e. $r_c = 0$ or $N \to \infty$), these interfaces can be represented using piecewise functions defined by

$$f = \begin{cases} x/\pi\alpha & \text{if} \quad 0 < x < \pi\alpha \,; \\ 1 & \text{if} \quad \pi\alpha < x < \pi(1-\alpha) \,; \\ (\pi - x)/\pi\alpha & \text{if} \quad \pi(1-\alpha) < x < \pi \,, \end{cases} \tag{3.15}$$

where the specific values $\alpha = 1/2$ and $\alpha = 1/4$ correspond to a type S and a type TS interface, respectively. To relate the characteristic slope ε to the interface slope angle φ, we use (3.16a) and (3.16b) for the type S and the type TS interface, respectively.

$$\tan\varphi = \frac{2\varepsilon}{\pi}, \qquad\qquad \tan\varphi = \frac{4\varepsilon}{\pi}. \tag{3.16a,b}$$

 We note that because there are 3 axes that correspond with each of the two sliding surfaces (See Figure 3.2a), the response of that sample has a 3–fold rotational symmetry.

Chapter 4

Numerical method

Here we discuss the numerical method used to solve the b.v.p.'s of the bicrystal model stated in the previous chapter. Using conventional finite element to solve b.v.p. (3.8) of diffusionally–accommodated grain boundary sliding is challenging, in particular because of the boundary condition (3.8d). As a result of corner stress concentrations described in §5.1, numerical approximation of the term $\mathrm{d}^2\sigma_{nn}/\mathrm{d}s^2$ found in (3.8d) will incur a large numerical error and requires excessively fine mesh near corners.

To circumvent this difficulty, we use the method of eigenfunction expansion described in Sethian & Wilkening [38]. In order to apply that method, we need to decompose the b.v.p. stated in (3.8) into two separate b.v.p.'s, namely, b.v.p$^{(1)}$ and b.v.p$^{(2)}$. These b.v.p.'s are described in §4.1. B.v.p$^{(1)}$ has a trivial solution given in §4.2, whereas b.v.p$^{(2)}$ is solved using eigenfunction expansion method discussed in §4.3. In §4.4, we describe the method used to extract the required eigenvalues and eigenvectors. That method requires finite element method which is described in §4.5. In that same section, we also describe the finite element method used to solve the b.v.p. posed below 3.10 of elastically–accommodated grain boundary sliding.

4.1 Decomposition of boundary value problem: b.v.p$^{(1)}$ and b.v.p$^{(2)}$

Because the interface $\mathcal{S}_I$ is time-independent and the b.v.p. given in (3.8) is linear, the principle of superposition applies. We decompose the b.v.p. into two separate b.v.p.'s, namely, b.v.p$^{(1)}$ and b.v.p$^{(2)}$. These two b.v.p.'s share the same geometry with the original

problem that is shown in Figure 3.1. Using superscripts 1 and 2 to denote, respectively, variables associated with b.v.p.$^{(1)}$ and b.v.p.$^{(2)}$, the stress field σ_{ij}, strain field e_{ij} and the displacement field u_1, u_2 in (3.8) can be obtained by superposing the solution of the two b.v.p.'s, i.e.

$$\sigma_{ij} = \sigma_{ij}^{(1)} + \sigma_{ij}^{(2)}, \tag{4.1a}$$

$$e_{ij} = e_{ij}^{(1)} + e_{ij}^{(2)}, \tag{4.1b}$$

$$(u_1, u_2) = (u_1^{(1)}, u_2^{(1)}) + (u_1^{(2)}, u_2^{(2)}). \tag{4.1c}$$

To simplify the notation, we use g_n and g_s to denote, respectively, the normal gap $[u_n]$ and the tangential gap $[u_s]$ of interface $\mathcal{S}_I$ in this chapter. Interfacial stresses and gaps are also denoted here, using 2×1 vectors of functions $\sigma_n = [\sigma_{nn}, \sigma_{ns}]^T$ and $g = [g_n, g_s]^T$, respectively.

The plane elastostatic equation in Eq. (3.8a), the periodic boundary conditions in Eqs. (3.8h,i) and the requirement that normal and tangential stresses across the grain boundary are continuous in Eqs. (3.8f,g) all apply in b.v.p.$^{(1)}$ and b.v.p.$^{(2)}$. The other boundary conditions are stated below.

4.1.1 Boundary conditions in b.v.p.$^{(1)}$

In b.v.p.$^{(1)}$, the boundary conditions at $y = \pm a$ are

$$u_1^{(1)} = \pm e^{i\omega t}, \qquad u_2^{(1)} = 0, \tag{4.2a,b}$$

and the boundary conditions along the interface $\mathcal{S}_I$ on $y = \varepsilon f(x)$ are

$$\sigma_{ns}^{(1)} = 0, \qquad \sigma_{nn}^{(1)} = 0. \tag{4.3a,b}$$

4.1.2 Boundary conditions in b.v.p.$^{(2)}$

Conversely in b.v.p.$^{(2)}$, boundary conditions at $y = \pm a$ are

$$u_1^{(2)} = 0, \qquad u_2^{(2)} = 0, \tag{4.4a,b}$$

whereas the boundary conditions along the interface $\mathcal{S}_I$ on $y = \varepsilon f(x)$ are

$$\mathcal{M}\dot{g}_s^{(2)} = \sigma_{ns}^{(2)}, \qquad \dot{g}_n^{(2)} + \frac{d^2\sigma_{nn}^{(2)}}{ds^2} = 0. \tag{4.5a,b}$$

4.2   Exact solution of b.v.p.$^{(1)}$

By inspection of b.v.p.$^{(1)}$, the two grains do not interact with one another through their interface $\mathcal{S}_I$. Hence, the two grains moved rigidly across one another and the displacement field u of the upper grain and the lower grain are $\hat{x}e^{i\omega t}$ and $-\hat{x}e^{i\omega t}$, respectively. The displacement fields satisfy all equations given in b.v.p$^{(1)}$ and the resulting normal gap and the tangential gap across the interface $\mathcal{S}_I$ are, respectively,

$$g_n^{(1)} = 2e^{i\omega t}\hat{x} \cdot \hat{n}\,, \qquad\qquad g_s^{(1)} = 2e^{i\omega t}\hat{x} \cdot \hat{s}\,. \qquad\qquad \text{(4.6a,b)}$$

4.3   Eigenfunction expansion solution of b.v.p.$^{(2)}$

To solve b.v.p.$^{(2)}$, we use eigenfunction expansion. In essence, we reduce a 2–dimensional problem given in b.v.p.$^{(2)}$ to a 1–dimensional problem defined along interface $\mathcal{S}_I$. We define a linear operator S that maps a given interfacial gaps $g^{(2)}$ onto the interfacial stresses $\sigma_n^{(2)}$ in b.v.p.$^{(2)}$. Because interfacial stresses in b.v.p.$^{(1)}$ are zero i.e. $\sigma_n^{(1)} = 0$, the interfacial stresses in b.v.p$^{(2)}$ are equivalent to that in the original b.v.p. i.e. $\sigma_n^{(2)} = \sigma_n$. The operator S is defined as follows

$$\mathsf{S} : g^{(2)} \to \sigma_n^{(2)}\,. \qquad\qquad \text{(4.7)}$$

We also define a differential operator L given as

$$\mathsf{L} : [\sigma_{nn},\, \sigma_{ns}]^{\mathrm{T}} \to \left[\frac{\mathrm{d}^2\sigma_{nn}}{\mathrm{d}s^2},\; \mathcal{M}^{-1}\sigma_{ns}\right]^{\mathrm{T}}\,. \qquad\qquad \text{(4.8)}$$

Using the definition given in (4.7) and (4.8), we find from the constitutive equations of the original b.v.p. given in (3.8d) and (3.8e) that $\mathsf{L}\mathsf{S}g^{(2)} = \dot{g}$. Applying the principle of superposition $\dot{g} = \dot{g}^{(1)} + \dot{g}^{(2)}$ to that equation, the 2-dimensional problem given in b.v.p.$^{(2)}$ is condensed into a single equation defined on the interface $\mathcal{S}_I$:

$$\dot{g}^{(2)} + \mathsf{L}\mathsf{S}\,g^{(2)} = -\dot{g}^{(1)}\,. \qquad\qquad \text{(4.9)}$$

The r.h.s. term in (4.9) can be calculated using (4.6). We also note that without the forcing term $\dot{g}^{(1)}$, $g^{(2)}$ is bounded in the limit $t \to \infty$, if the eigenvalues of $\mathsf{L}\mathsf{S}$ are greater than or

equal to zero. We show, using an example in Figure 4.2, that the eigenvalues are, indeed, positive.

Time evolution of the interfacial gap $g^{(2)}$ defined in (4.9) can thus be obtained by eigenfunction expansion if the eigenvalues γ_k and the eigenfunctions $Z_k(s)$ associated with the composite operator LS are known i.e.

$$\mathsf{LS}\, Z_k(s) = \gamma_k Z_k(s)\,. \tag{4.10}$$

Note: the eigenfunctions $Z_k(s)$ are 2×1 vector of functions, where its first and second components are associated with $g_n^{(2)}$ and $g_s^{(2)}$, respectively. Using N_z eigenfunctions, the solution to the homogeneous part of (4.9) (i.e. with $\dot{g}^{(1)} = 0$) can be written in a separable form

$$g_h^{(2)}(s,t) = \sum_{k=1}^{N_z} \beta_k\, e^{-\gamma_k t} Z_k(s)\,, \tag{4.11}$$

where β_k are coefficients determined by the initial condition $g_0^{(2)}(s)$. The coefficients β_k are found by requiring them to satisfy

$$\sum_{k=1}^{N_z} \beta_k Z_k(s) = g_0^{(2)}(s)\,. \tag{4.12}$$

Letting $\boldsymbol{\Phi}_Z$ be a $1 \times N_z$ vector containing these eigenfunctions,

$$\boldsymbol{\Phi}_Z = [Z_1(s), Z_2(s), \ldots, Z_N(s)]\,; \tag{4.13}$$

and $\boldsymbol{\Phi}_Z^*$ be the adjoint operator of $\boldsymbol{\Phi}_Z$ so that $\boldsymbol{\Phi}_Z^* g_0^{(2)}$ is a $N_z \times 1$ vector of scalars defined as

$$\boldsymbol{\Phi}_Z^* g_0^{(2)} = \int_{\mathcal{S}_I} \left[Z_1 g_0^{(2)}, Z_2 g_0^{(2)}, \ldots, Z_N g_0^{(2)} \right]^{\mathrm{T}} \mathrm{d}s\,, \tag{4.14}$$

the coefficients $\boldsymbol{\beta} = [\beta_1, \beta_2, \ldots, \beta_N]^{\mathrm{T}}$, upon solving (4.11) for β_k, can be written compactly as

$$\boldsymbol{\beta} = (\boldsymbol{\Phi}_Z^* \boldsymbol{\Phi}_Z)^{-1} \boldsymbol{\Phi}_Z^* g_0^{(2)}\,. \tag{4.15}$$

Substituting (4.15) into (4.11), the latter equation becomes

$$g_h^{(2)}(s,t) = \mathsf{E}(t) g_0^{(2)}(s)\,, \tag{4.16}$$

where $\mathsf{E}(t)$ is defined as the source operator or evolution operator

$$\mathsf{E}(t) = \boldsymbol{\Phi}_Z\, e^{-\boldsymbol{\Lambda} t}\, (\boldsymbol{\Phi}_Z^* \boldsymbol{\Phi}_Z)^{-1} \boldsymbol{\Phi}_Z^* \tag{4.17}$$

and Λ is a diagonal matrix defined as $\Lambda = \text{diag}\,[\gamma_1, \gamma_2, \ldots, \gamma_{N_z}]$. The solution to the inhomogeneous p.d.e. given in (4.9) can then be obtained using Duhamel's principle

$$g^{(2)}(s, t) = \mathsf{E}(t)g_0^{(2)} - \int_0^t \mathsf{E}(t - \bar{t})\,\dot{g}^{(1)}(s, \bar{t})\,\mathrm{d}\bar{t}. \tag{4.18}$$

Hence, the problem of diffusionally–accommodated grain boundary sliding on a bicrystal model given in (3.8) is solved, if the eigenvalues γ_k and the eigenfunctions Z_k defined in (4.10) are found.

4.4   Extraction of eigenvalues/eigenvectors

We now describe the method used to extract the eigenvalues γ_k and eigenfunctions Z_k in finite dimension. Though the composite operator LS can be obtained directly using finite element method to approximate S and finite difference method to approximate L, corner stress concentrations described in §5.1.4 will lead to large numerical errors when using finite difference to approximate L.

To circumvent that problem, we use a method given in Sethian & Wilkening [38], where they solve the problem of electromigration due to grain boundary diffusion. Instead of constructing L directly using finite difference method, a "pseudo–inverse" A of the composite operator LS is constructed. That operator A has similar eigenfunctions Z_k to that of LS, and has eigenvalues ζ_k that are related to γ_k by

$$\zeta_k = \begin{cases} \gamma_k & \text{if } \gamma_k \neq 0 \\ 0 & \text{if } \gamma_k = 0 \end{cases}. \tag{4.19}$$

The operator A is defined as

$$\mathsf{A} = \mathsf{QBGQ}. \tag{4.20}$$

In Eq. (4.20), B is the inverse of S and maps interfacial stresses $\sigma_n^{(2)}$ to the gap $g^{(2)}$, G contains a Poisson operator and Q is a non-orthogonal projection operator. We now describe these operators and show how they are constructed in finite dimensional space.

4.4.1   Operator B

The operator B is defined as follows:

$$\mathsf{B} : \sigma_n^{(2)} \rightarrow g^{(2)}. \tag{4.21}$$

In essence, B is the inverse of S defined in (4.7) and maps the interfacial stresses $\sigma_n^{(2)}(s)$ to the interfacial gaps $g^{(2)}(s)$. The functions in the vectors $g^{(2)}$ and $\sigma_n^{(2)}$ can be approximated using conventional finite element hat functions $\psi_j(s)$
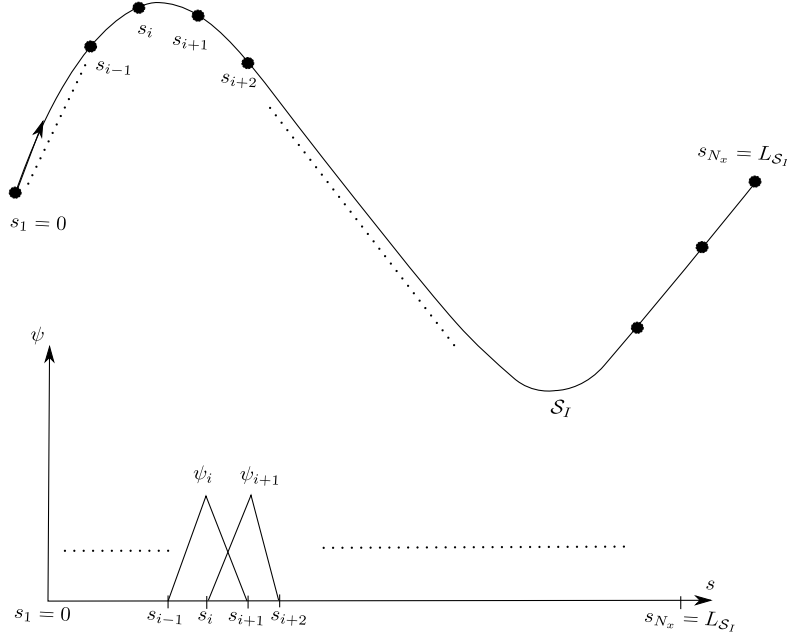
Figure 4.1: Linear shape functions $\psi_k(s)$ on $\mathcal{S}_I$

Figure 4.1 shows the schematic of the hat functions $\psi_j(s)$ defined along interface $\mathcal{S}_I$. We have denoted $L_{\mathcal{S}_I}$ as the length of that interface in the figure. The interfacial gaps and stresses are approximated using N_x hat functions by

$$g_n^{(2)}(s) = \sum_{j=1}^{N_x} \psi_j(s)\, \tilde{g}_{n,j}^{(2)}, \qquad g_s^{(2)}(s) = \sum_{j=1}^{N_x} \psi_j(s)\, \tilde{g}_{s,j}^{(2)}; \qquad (4.22\text{a,b})$$

and

$$\sigma_{nn}(s) = \sum_{j=1}^{N_x} \psi_j(s)\, \tilde{\sigma}_{nn,j}, \qquad \sigma_{ns}(s) = \sum_{j=1}^{N_x} \psi_j(s)\, \tilde{\sigma}_{ns,j}. \qquad (4.23\text{a,b})$$

In Eq. (4.22), $\tilde{g}_{n,j}^{(2)}$ and $\tilde{g}_{s,j}^{(2)}$ refer to the values of the normal gap and tangential gap at node j, whereas $\tilde{\sigma}_{nn,j}$ and $\tilde{\sigma}_{ns,j}$ in Eq. (4.23) refer to the values of the normal stress and tangential stress at node j. Henceforth, we use tilde to denote vectors containing the nodal values of

a function. Letting $\mathbf{\Psi}_2$ be a $2 \times 2N_x$ matrix containing these hat functions i.e.

$$\mathbf{\Psi}_2 = \begin{pmatrix} \psi_1(s) & \dots & \psi_{N_x}(s) & 0 & \dots & 0 \\ 0 & \dots & 0 & \psi_1(s) & \dots & \psi_{N_x}(s) \end{pmatrix}, \quad (4.24)$$

the vector function of interfacial gap $g^{(2)}$ and interfacial stress σ_n can be written compactly as

$$g^{(2)}(s) = \mathbf{\Psi}_2 \, \tilde{g}^{(2)} , \qquad \sigma_n^{(2)}(s) = \mathbf{\Psi}_2 \, \tilde{\sigma}_n^{(2)} , \qquad (4.25\text{a,b})$$

where $\tilde{g}^{(2)} = [\tilde{g}^{(2)}_{n,1}, \dots, \tilde{g}^{(2)}_{n,N_x}, \tilde{g}^{(2)}_{s,1}, \dots, \tilde{g}^{(2)}_{s,N_x}]^\mathrm{T}$ and $\tilde{\sigma}_n^{(2)} = [\tilde{\sigma}^{(2)}_{nn,1}, \dots, \tilde{\sigma}^{(2)}_{nn,N_x}, \tilde{\sigma}^{(2)}_{ns,1}, \dots, \tilde{\sigma}^{(2)}_{ns,N_x}]^\mathrm{T}$ are vectors of size $2N_x \times 1$. Mathematically, $\mathbf{\Psi}_2$ is also an operator that maps a $2N_x \times 1$ vector into a 2×1 vector of functions, i.e. $\mathbf{\Psi}_2 : \mathbb{R}^{2N_x} \to W_h^2$. Correspondingly, we denote its adjoint by $\mathbf{\Psi}_2^*$ that is define as follows

$$\mathbf{\Psi}_2^* h_2 \equiv \int_{S_I} \mathbf{\Psi}_2^\mathrm{T} h_2 \, \mathrm{d}s , \qquad (4.26)$$

where $h_2(s)$ is a 2×1 vector of functions defined along $\mathcal{S}_I$.

To obtain the finite dimensional operator $\mathbf{B} \in \mathbb{R}^{2N_x} \times \mathbb{R}^{2N_x}$ that maps the nodal values of the interfacial stresses $\tilde{\sigma}_n^{(2)}$ to the nodal values of the interfacial gaps $\tilde{g}^{(2)}$, i.e. $\mathbf{B} : \mathbb{R}^{2N_x} \to \mathbb{R}^{2N_x}$, we use the identity $\mathbf{\Psi}_2 \mathbf{B} \, \tilde{g}^{(2)} = \sigma_n^{(2)}(s) = \mathbf{B} \mathbf{\Psi}_2 \, \tilde{g}^{(2)}$ that results in

$$\mathbf{\Psi}_2 \mathbf{B} = \mathbf{B} \mathbf{\Psi}_2 . \qquad (4.27)$$

Multiplying (4.27) by the i-th direction unit vector $\tilde{e}_i$ and then applying the adjoint operator $\mathbf{\Psi}_2^*$ to the resulting expression leads to

$$\mathbf{\Psi}_2^* \, \mathbf{\Psi}_2 \, \mathbf{B} \tilde{e}_i = \mathbf{\Psi}_2^* \, \mathbf{B} \mathbf{\Psi}_2 \tilde{e}_i . \qquad (4.28)$$

Letting $\mathbf{M}_2 = \mathbf{\Psi}_2^* \, \mathbf{\Psi}_2$ and multiplying the above expression by $\mathbf{M}_2^{-1}$, the first column of $\mathbf{B}$, which is given by $\mathbf{B}\tilde{e}_i$, becomes

$$\mathbf{B} \tilde{e}_i = \mathbf{M}_2^{-1} \mathbf{\Psi}_2^* \mathbf{B} \mathbf{\Psi}_2 \tilde{e}_i . \qquad (4.29)$$

In Eq. (4.29), $\mathbf{M}_2$ is the "mass matrix" found in finite element formulation. We also note that in Eq. (4.29), the resultant of $\mathbf{B} \mathbf{\Psi}_2 \tilde{e}_i$ is the interfacial gaps $g^{(2)}(s) = [g_n^{(2)}(s), g_s^{(2)}(s)]^\mathrm{T}$ that is obtained from a given interfacial stress $\sigma_n^{(2)}(s) = \mathbf{\Psi}_2 \, \tilde{e}_i$, whereas $\mathbf{M}_2^{-1} \mathbf{\Psi}_2^* \, g^{(2)}(s)$ results in a $2N_x \times 1$ vector $\tilde{g}^{(2)}$ containing nodal values of interfacial gaps defined below (4.25). The

i–th column of **B**, therefore, contains nodal values of the interfacial gaps $\tilde{g}^{(2)}$ found from solving b.v.p.$^{(2)}$ with boundary conditions (4.5) replaced by

$$\sigma_{nn}^{(2)} = \begin{cases} \psi_i & \text{for} & i = 1, \ldots, N_x \\ 0 & \text{for} & i = N_x + 1, \ldots, 2N_x \end{cases} \quad ; \tag{4.30a}$$

$$\sigma_{ns}^{(2)} = \begin{cases} 0 & \text{for} & i = 1, \ldots, N_x \\ \psi_{i-N_x} & \text{for} & i = N_x + 1, \ldots, 2N_x \end{cases} \quad . \tag{4.30b}$$

The entire **B** matrix can therefore be populated by solving, repeatedly, for the nodal interfacial gaps $\tilde{g}^{(2)}$ using finite element method (described in §4.5) with the above boundary conditions for $i = 1, \ldots, 2N_x$.

4.4.2 Operator G

The operator G is defined as follows:

$$\mathsf{G} : \left[\frac{\mathrm{d}^2 \sigma_{nn}(s)}{\mathrm{d}s^2}, \ \sigma_{ns}(s) \right]^{\mathsf{T}} \rightarrow [\sigma_{nn}(s), \ -\mathcal{M}\sigma_{ns}(s)]^{\mathsf{T}} , \tag{4.31}$$

where σ_{nn} and σ_{ns} satisfy periodic boundary conditions at the two end points of $\mathcal{S}_I$. The operator G can be decomposed into two operators P and $\overline{\mathsf{G}}$ that operates on the functions σ_{ns} and $\mathrm{d}^2\sigma_{nn}/\mathrm{d}s^2$ separately, i.e.

$$\mathsf{P} : \sigma_{ns} \rightarrow -\mathcal{M}\sigma_{ns} , \tag{4.32a}$$

$$\overline{\mathsf{G}} : \frac{\mathrm{d}^2\sigma_{nn}}{\mathrm{d}s^2} \rightarrow \sigma_{nn} . \tag{4.32b}$$

In Eq. (4.32a), P simply multiply σ_{ns} by a scalar $-\mathcal{M}$ and can be represented, in finite dimension by

$$\mathbf{P} = -\mathcal{M}\mathbf{I} . \tag{4.33}$$

Here, $\mathbf{I} \in \mathbb{R}^{N_x} \times \mathbb{R}^{N_x}$ is the identity matrix. The operator $\overline{\mathsf{G}}$ defined in (4.32b) is referred here as a Poisson operator. That operator solves the Poisson equation with given function $h_1(s)$ and periodic boundary conditions for $\sigma_{nn}(s)$ i.e.

$$\frac{\mathrm{d}^2\sigma_{nn}}{\mathrm{d}s^2} = h_1(s) , \tag{4.34a}$$

$$\sigma_{nn}|_{s=0} = \sigma_{nn}|_{s=L_{\mathcal{S}_I}} \, , \tag{4.34b}$$

$$\left.\frac{\mathrm{d}\sigma_{nn}}{\mathrm{d}s}\right|_{s=0} = \left.\frac{\mathrm{d}\sigma_{nn}}{\mathrm{d}s}\right|_{s=L_{\mathcal{S}_I}} . \tag{4.34c}$$

We use finite element method to obtain $\overline{\mathbf{G}}$ in finite dimensional space. Denoting $v(s)$ as the test function, the weak formulation of (4.34) becomes

$$\int_{\mathcal{S}_I} \frac{\mathrm{d}\sigma_{nn}}{\mathrm{d}s}\frac{\mathrm{d}v}{\mathrm{d}s}\mathrm{d}s = -\int_{\mathcal{S}_I} v\, h_1 \,\mathrm{d}s . \tag{4.35}$$

The variables v, σ_{nn} and h_1 are approximated using hat functions ψ_k illustrated in Figure 4.1. Letting $\mathbf{\Psi}_1$ be a $1 \times N_x$ matrix containing these hat functions ψ_k i.e.

$$\mathbf{\Psi}_1 = [\psi_1, \ldots, \psi_{N_x}] , \tag{4.36}$$

these variables can be written as

$$v = \mathbf{\Psi}_1 \, \tilde{v}, \qquad \sigma_{nn} = \mathbf{\Psi}_1 \, \tilde{\sigma}_{nn}, \qquad h_1 = \mathbf{\Psi}_1 \, \tilde{h}_1 . \tag{4.37a, b, c}$$

In Eq. (4.37), $\tilde{v}$, $\tilde{\sigma}_{nn}$ and $\tilde{h}_1$ are, respectively, $N_x \times 1$ vectors containing the nodal values of the variables v, σ_{nn} and h_1. Substituting (4.37) into (4.35), the latter expression becomes

$$\mathbf{K_G}\, \tilde{\sigma}_{nn} = -\mathbf{M}_1\, \tilde{h}_1 \tag{4.38}$$

where $\mathbf{K_G}$ and $\mathbf{M}_1$ are $N_x \times N_x$ matrices given by

$$\mathbf{K_G} = \int_{\mathcal{S}_I} \frac{\mathrm{d}\mathbf{\Psi}_1^{\mathrm{T}}}{\mathrm{d}s}\frac{\mathrm{d}\mathbf{\Psi}_1}{\mathrm{d}s}\mathrm{d}s , \qquad \mathbf{M}_1 = \int_{\mathcal{S}_I} \mathbf{\Psi}_1^{\mathrm{T}}\mathbf{\Psi}_1 \,\mathrm{d}s . \tag{4.39a, b}$$

We note that $\mathbf{K_G}$ is the stiffness matrix found in finite element method, whereas $\mathbf{M}_1$ is the mass matrix analogous to $\mathbf{M}_2$ described below (4.29). Because the solution to (4.34) is not unique, $\mathbf{K_G}$ is not invertible. Hence, to obtain the finite dimensional Poisson operator $\overline{\mathbf{G}}$ so that

$$\tilde{\sigma}_{nn} = \overline{\mathbf{G}}\, \tilde{h}_1 , \tag{4.40}$$

we uses the singular value decomposition of $\mathbf{K}_G$ i.e.

$$\mathbf{K}_G = \mathbf{U\Sigma V}^{\mathrm{T}} \tag{4.41}$$

where $\mathbf{U}$, $\mathbf{V}$ and $\boldsymbol{\Sigma}$ are, respectively, the left–singular matrix, the right–singular matrix and a diagonal matrix containing the singular values of $\mathbf{K}_G$. We note that one of the singular value is zero. Letting $\boldsymbol{\Sigma}^*$ be a diagonal matrix having entries that are reciprocal of that in $\boldsymbol{\Sigma}$, and has zero entry if the corresponding entry in $\boldsymbol{\Sigma}$ is zero, the finite dimensional Poisson operator becomes

$$\overline{\mathbf{G}} = -\mathbf{V}\boldsymbol{\Sigma}^*\mathbf{U}^T\mathbf{M}_1\,. \tag{4.42}$$

Noting that $\mathbf{P}$ and $\overline{\mathbf{G}}$, which are defined respectively in (4.33) and (4.42), operate separately as described in (4.32), the operator G in finite dimension is given by

$$\mathbf{G} = \begin{pmatrix} \overline{\mathbf{G}} & 0 \\ 0 & \mathbf{P} \end{pmatrix}. \tag{4.43}$$

In Eq. (4.43), $\mathbf{G}$ is a $2N_x \times 2N_x$ matrix.

4.4.3 Projection Operator Q

The non–orthogonal projection operator Q is defined following Sethian & Wilkening [38] as

$$\mathsf{Q} = \mathsf{I} - \frac{(\mathfrak{e}, \cdot)}{(\mathfrak{e}, \mathsf{B}\mathfrak{e})}\mathsf{B}\mathfrak{e}\,, \tag{4.44}$$

where I is an identity operator and $\mathfrak{e}(s) = [1,0]^{\mathrm{T}}$ is a 2×1 vector of constants. Note: the projection operator Q defined here is equivalent to Q^* defined in Wilkening *et al.* [41]. In Eq. (4.44), the round brackets denote the inner product between two 2×1 vector functions $h_2(s)$ and $q_2(s)$ that are defined along $\mathcal{S}_I$ i.e.

$$(h_2, q_2) \equiv \int_{\mathcal{S}_I} h_2^{\mathrm{T}}\, q_2 \,\mathrm{d}s\,. \tag{4.45}$$

Operator Q is constructed to have its range for the first component restricted to the space of "mean zero" functions $L_{MZ}^2 := \left\{h \in L^2(\mathcal{S}_I);\ \int_{\mathcal{S}_I} h\,\mathrm{d}s = 0\right\}$. In other words, for a 2×1 vector of functions $h_2(s)$, the first component of the resultant mapping $\mathfrak{e}^T\mathsf{Q}\,h_2 \in L_{MZ}^2$. That operator Q also has kernel along $\mathsf{B}\mathfrak{e}$. Note: the resultant of $\mathsf{B}\mathfrak{e}$ is the interfacial gaps produced by interfacial stresses $\sigma_{nn} = \mathfrak{e} = 1$ and $\sigma_{ns} = 0$. The main purpose of Q is to restrict g_n (or $g_n^{(2)}$ because $g_n^{(1)}$ defined in (4.6a) $\in L_{MZ}^2$) to functions $\in L_{MZ}^2$. That restriction is required by mass conservation across $s = 0$ and $s = L_{\mathcal{S}_I}$, i.e. $\left.\frac{\mathrm{d}\sigma_{nn}}{\mathrm{d}s}\right|_{s=0} = \left.\frac{\mathrm{d}\sigma_{nn}}{\mathrm{d}s}\right|_{s=L_{\mathcal{S}_I}}$. To see that mass

conservation requires $g_n \in L^2_{MZ}$, we integrate (3.8d) with respect to s and find that

$$\frac{\partial}{\partial t} \int_{\mathcal{S}_I} g_n \, \mathrm{d}s = 0 \,. \tag{4.46}$$

From (4.46), , $g_n \in L^2_{MZ}$ at all time t if the normal interfacial gap has zero mean along the interface at $t = 0$.

We now consider the following mappings by QBG:

$$\begin{pmatrix} g_n^{(2)} \\ g_s^{(2)} \end{pmatrix} \xleftarrow{\ \mathsf{Q}\ } \begin{pmatrix} g_n^{(2)} \\ g_s^{(2)} \end{pmatrix} + c\, \mathsf{B}\mathfrak{e} \xleftarrow{\ \mathsf{B}\ } \begin{pmatrix} \sigma_{nn}^{(2)} + c \\ \sigma_{ns}^{(2)} \end{pmatrix} \xleftarrow{\ \mathsf{G}\ } \begin{pmatrix} \frac{\mathrm{d}^2 \sigma_{nn}^{(2)}}{\mathrm{d}s^2} \\ -\mathcal{M}^{-1} \sigma_{ns}^{(2)} \end{pmatrix} . \tag{4.47}$$

In Eq. (4.47), c is an integration constant introduced by the Poisson operator $\overline{\mathsf{G}}$ in G, and Q annihilate the additional terms produced by c. Comparing (4.47) to the mappings by LS:

$$\begin{pmatrix} g_n^{(2)} \\ g_s^{(2)} \end{pmatrix} \xrightarrow{\ \mathsf{S}\ } \begin{pmatrix} \sigma_{nn}^{(2)} \\ \sigma_{ns}^{(2)} \end{pmatrix} \xrightarrow{\ \mathsf{L}\ } \begin{pmatrix} \frac{\mathrm{d}^2 \sigma_{nn}^{(2)}}{\mathrm{d}s^2} \\ -\mathcal{M}^{-1} \sigma_{ns}^{(2)} \end{pmatrix} , \tag{4.48}$$

we thus find that the composite map QBG is the inverse of LS i.e.

$$\mathsf{QBGLS} = \mathsf{I} \,, \tag{4.49}$$

where I is the identity operator. Applying the expression given in (4.49) to Z_k and using (4.10), we find that

$$\gamma_k \mathsf{QBG} Z_k = Z_k \,. \tag{4.50}$$

The above equation (4.50), however, does not hold if $\gamma_k = 0$ or equivalently, when $Z_k \in \mathsf{B}\mathfrak{e} = \ker(\mathsf{LS})$. Because $\mathsf{Q}Z_k = Z_k$ when $Z_k \in L^2_{MZ}$, and $\mathsf{Q}Z_k = 0$ when $Z_k \in \mathsf{B}\mathfrak{e}$, we can insert Q between G and Z_k in the l.h.s. of (4.50) and applying Q to r.h.s. of that equation to obtain

$$\gamma_k \mathsf{QBGQ} Z_k = \mathsf{Q} Z_k \,. \tag{4.51}$$

Eq. (4.51) is thus satisfied for all values of γ_k and QBGQ has eigenfunctions Z_k that are similar to that of LS and eigenvalues ζ_k that are related to eigenvalues γ_k of LS by (4.19).

The operator Q in finite dimensional space, denoted here as $\mathbf{Q}$, can be obtained as follows. Letting $\tilde{\mathbf{e}} = (1, \ldots, 1)^{\mathrm{T}}$ be a $N_x \times 1$ vector of ones and $\tilde{\mathbf{z}} = (0, \ldots, 0)^{\mathrm{T}}$ be a $N_x \times 1$ vector of zeros, the vector $\mathfrak{e}(s)$ defined below (4.44) is given, in finite dimensional space, by $\tilde{\mathfrak{e}}^{\mathrm{T}} = (\tilde{\mathbf{e}}^{\mathrm{T}}, \tilde{\mathbf{z}}^{\mathrm{T}})$. To relate between $\mathfrak{e}(s)$ and $\tilde{\mathfrak{e}}$, we use

$$\mathfrak{e} = \mathbf{\Psi}_2 \, \tilde{\mathfrak{e}} \,. \tag{4.52}$$

Note: this form is analogous to the representation given in (4.25). Using (4.52), (4.27) and the definition given in (4.45), we find that the denominator in (4.44) becomes

$$(\mathbf{e}, \mathbf{B}\mathbf{e}) = \int_{\mathcal{S}_I} \tilde{\mathbf{e}}^T \mathbf{\Psi}_2^T \mathbf{\Psi}_2 \mathbf{B}\tilde{\mathbf{e}} \, ds = \tilde{\mathbf{e}}^T \mathbf{M}_2 \mathbf{B}\tilde{\mathbf{e}} \,. \tag{4.53}$$

We have use the definition of $\mathbf{M}_2$ given above (4.29) to obtain the last expression in the above equation. Similarly, one can prove using (4.52), (4.27) and the identity $\mathbf{Q}\mathbf{\Psi}_2 = \mathbf{\Psi}_2 \mathbf{Q}$ that

$$\mathbf{Q} = \mathbf{I} - \frac{\mathbf{B}\tilde{\mathbf{e}}\tilde{\mathbf{e}}^T \mathbf{M}_2}{\tilde{\mathbf{e}}^T \mathbf{M}_2 \mathbf{B}\tilde{\mathbf{e}}} \,. \tag{4.54}$$

Here, $\mathbf{Q}$ is a $2N_x \times 2N_x$ matrix and $\mathbf{I}$ is an identity matrix.

4.4.4   Steady state solution to b.v.p.[2]

The pseudo–inverse operator A defined in (4.20), in finite dimensional space, is

$$\mathbf{A} = \mathbf{QBGQ} \,, \tag{4.55}$$

where $\mathbf{Q}$, $\mathbf{G}$ are defined in (4.54), (4.43), respectively, and $\mathbf{B}$ is found using finite element method described below (4.30).
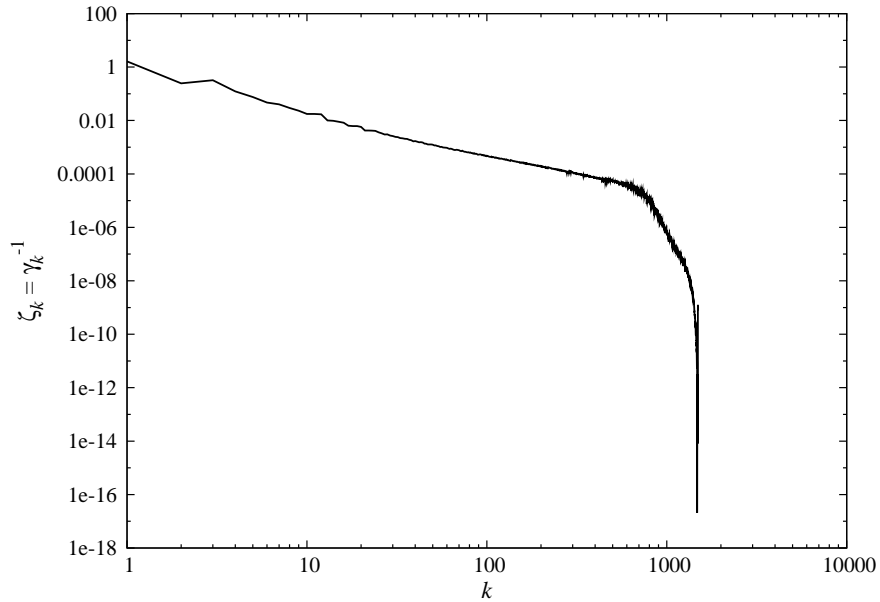

Figure 4.2: Eigenvalues γ_k as a function of k. Type S interface. $\varphi = 30°$. $N = 100$. $N_x = 748$.

Figure 4.2 shows the eigenvalues ζ_k of $\mathbf{A}$ obtained for the interface described in the caption. These eigenvalues are related to γ_k by (4.10). In the figure, the eigenvalues $\zeta_k > 0$ and correspondingly eigenvalues γ_k of LS are also greater than zero. The positivity of these eigenvalues γ_k thus ensures the solution $g^{(2)}$ given in (4.18) is bounded at all times.

To relate the eigenfunctions $Z_k(s)$ of LS to the eigenvectors $\tilde{Z}_k$, we use $Z_k(s) = \Psi_2 \tilde{Z}_k$. Using that relation and letting $\widetilde{\mathbf{\Phi}}_Z = [\tilde{Z}_1, \ldots, \tilde{Z}_{N_Z}]$ be a matrix containing eigenvectors, we find from (4.13) that

$$\mathbf{\Phi}_Z = \mathbf{\Psi}_2 \widetilde{\mathbf{\Phi}}_Z \,. \tag{4.56}$$

Substituting (4.56) into (4.17) and using the identity $\mathbf{E}\mathbf{\Psi}_2 = \mathbf{\Psi}_2\mathbf{E}$, we find that the source operator in finite dimension becomes

$$\mathbf{E}(t) = \widetilde{\mathbf{\Phi}}_Z e^{-\mathbf{\Lambda} t} \widetilde{\mathbf{\Phi}}_Z^{-1} \,. \tag{4.57}$$

From (4.18), the time evolution of the nodal gaps in b.v.p$^{(2)}$ becomes

$$\tilde{g}^{(2)}(t) = \mathbf{E}(t)\tilde{g}_0^{(2)} - \int_0^t \mathbf{E}(t - \bar{t})\dot{\tilde{g}}^{(1)}(\bar{t})\,\mathrm{d}\bar{t}\,, \tag{4.58}$$

where $\tilde{g}_0^{(2)}$ is the nodal values of the initial condition $g_0^{(2)}$ and $\dot{g}^{(1)}$ is the nodal values of $\dot{g}^{(1)}$ evaluated using (4.6). At steady state, the first r.h.s. term of (4.58) vanishes. Consequently, the steady–state solution for the interfacial gap is

$$\tilde{g}_{ss}^{(2)}(t) = \int_\infty^t \mathbf{E}(t - \bar{t})\dot{\tilde{g}}^{(1)}(\bar{t})\,\mathrm{d}\bar{t}\,. \tag{4.59}$$

This expression can be simplified further by substituting (4.57) and (4.6), and then evaluating that resultant integral to obtain

$$\tilde{g}_{ss}^{(2)}(t) = \widetilde{\mathbf{\Phi}}_Z\,\mathbf{D}_s\,\widetilde{\mathbf{\Phi}}_Z^{-1}\tilde{g}(0)^{(1)}e^{\mathrm{i}\omega t}\,. \tag{4.60}$$

In Eq. (4.60), $\mathbf{D}_s$ is a diagonal matrix with k-th component given as

$$\mathbf{D}_{s(k,k)} = \frac{\mathrm{i}\omega\gamma_k + \omega^2}{\omega^2 + \gamma_k^2}\,. \tag{4.61}$$

Denoting $\tilde{g}_{ss}^{(2)}(t) = \hat{g}_{ss}^{(2)}(\omega)e^{\mathrm{i}\omega t}$ where

$$\hat{g}_{ss}^{(2)}(\omega) = \widetilde{\mathbf{\Phi}}_Z\,\mathbf{D}_s\,\widetilde{\mathbf{\Phi}}_Z^{-1}\tilde{g}(0)^{(1)}\,, \tag{4.62}$$

the nodal values of σ_n can be found using

$$\tilde{\sigma}_n(\omega) = \mathbf{B}^{-1}\hat{g}_{ss}^{(2)}(\omega) \,. \tag{4.63}$$

Noting that $\sigma_n(\omega) \cdot g^{(1)}(0)/2$ is the projection of the interfacial stresses in the x–direction, the x–average shear stress at $y = \pm a$ becomes

$$\tau(\omega) = \frac{1}{2} \int_{\mathcal{S}_I} \tilde{\sigma}_n^{\mathrm{T}}(\omega)\boldsymbol{\Psi}_2^{\mathrm{T}}\boldsymbol{\Psi}_2\,\tilde{g}(0)^{(1)}\mathrm{d}s = \frac{1}{2}\tilde{\sigma}_n^{\mathrm{T}}(\omega)\mathbf{M}_2\tilde{g}(0)^{(1)} \,, \tag{4.64}$$

and the mechanical loss spectrum $\mathcal{L}(\omega)$ can then be calculated from its definition in (3.13).

4.5 Finite Element Method

Here we describe the finite element method used (i) to solve the b.v.p. described above (4.30) needed to generate the matrix $\mathbf{B}$, and (ii) to solve for the b.v.p. of elastically–accommodated grain boundary sliding posed below (3.10). To begin, we first derive the weak formulation of the b.v.p. described above (4.30).

4.5.1 Weak formulation

The Navier–Cauchy equation of elasticity given in (3.8a) is the resultant of the balance of linear momentum, the isotropic material constitutive equation and the small strain definition given, respectively, as

$$\sigma_{ij,j} = 0 \,, \tag{4.65a}$$

$$\sigma_{ij} = \frac{1}{1+\nu}\left(e_{ij} + \frac{\nu}{1-2\nu}e_{kk}\delta_{ij}\right) \,, \tag{4.65b}$$

$$e_{ij} = \frac{1}{2}\left(u_{i,j} + u_{j,i}\right) \,. \tag{4.65c}$$

We shall use these equations (instead of the Navier–Cauchy equation) to derive the weak formulation here. Letting v be the test function that is zero at boundaries having prescribed displacement, and v_i be its component, we take the inner product of Eq. (4.65a) with v and integrate the resultant expression over the entire material region $\mathcal{V}$ to obtain the weak formulation

$$\int_{\mathcal{V}} \sigma_{ij}v_{i,j}\,\mathrm{d}\mathcal{V} - \int_{\Gamma} \sigma_{ij}n_j v_i\,\mathrm{d}\Gamma = 0 \,. \tag{4.66}$$

In the above equation, $\mathcal{V}$ and Γ denotes, respectively, the combined volume and boundaries of grain 1 and grain 2, whereas n_j refers to the vector components of the outward normal along the boundaries. In arriving at (4.66), we have used the identity $\sigma_{ij,j}v_i = (\sigma_{ij}v_i)_{,j} - \sigma_{ij,j}v_{i,j}$ and the divergence theorem. We also note that the traction along boundary Γ is given by $t_i = \sigma_{ij}n_j$. Correspondingly, the second integral in (4.66) becomes $\int_{S_I} \sigma_{nn}v_n + \sigma_{ns}v_n \, ds$, where σ_{nn} and σ_{ns} are prescribed on $\mathcal{S}_I$.

To enforce the boundary conditions, we use the standard penalty method. For the general case when displacement $u = \pm U$ is prescribed at $y = \pm a$, and when a periodic boundary condition is imposed across $x = 0$ and $x = 2\pi$, we add terms scaled by a large positive penalty parameter P in the weak formulation (4.66) to obtain

$$
\underbrace{\int_{\mathcal{V}} \sigma_{ij}v_{i,j} \, d\mathcal{V} - \int_{\mathcal{S}_I} \sigma_{nn}v_n \, ds + \sigma_{ns}v_s \, ds}_{\text{traction b.c.}}
$$

$$
\underbrace{+ P \int_{-a}^{a} \{u_i(0,y) - u_i(2\pi, y)\} \, v_i(0,y) + \{u_i(2\pi, y) - u_i(0,y)\} \, v_i(2\pi, y) \, dy}_{\text{periodic b.c.}} \tag{4.67}
$$

$$
\underbrace{+ P \int_{0}^{2\pi} \{u_i(x,a) - U_i\} \, v_i(x,a) + \{u_i(x,-a) + U_i)\} \, v_i(x,-a) \, dx = 0 \,.}_{\text{displacement b.c.}}
$$

We note that the periodic and the displacement boundary conditions are exactly enforced in the limit as $P \to \infty$.

4.5.2 Discretization

Figure 4.3 shows the finite element discretization of grain 1. To capture the rounded corners in the interface $\mathcal{S}_I$, we increase the mesh density near corners. The expression given in (4.67) is now discretized using finite element method. Specifically, we approximate the displacement field u_i and the test function v_i in each element using bilinear shape functions $\phi_i(x,y)$ i.e.

$$
u_1 = \sum_{i=1}^{4} \phi_i(x,y) \, \tilde{a}_i, \qquad u_2 = \sum_{k=1}^{4} \phi_i(x,y) \, \tilde{a}_{i+4} \,, \tag{4.68a, b}
$$
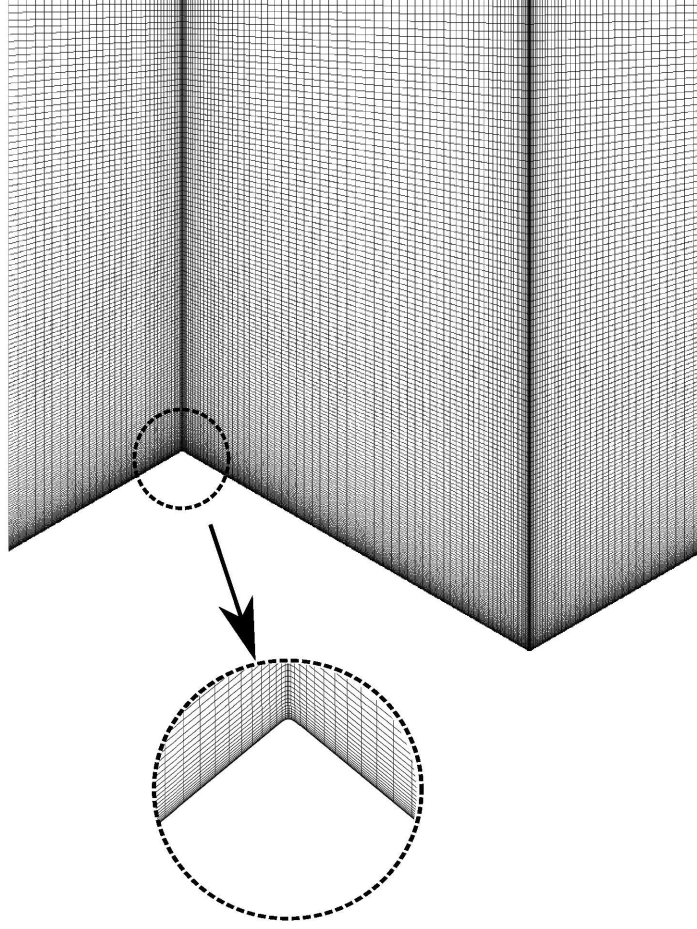
Figure 4.3: Finite element mesh in grain 1. 22200 nodes and 21903 elements. Type S, $a = 5$, $\varphi = 30°$, $N = 100$. Inset: mesh around a corner.

and

$$v_1 = \sum_{i=1}^{4} \phi_i(x, y)\, \tilde{b}_i, \qquad v_2 = \sum_{k=1}^{4} \phi_i(x, y)\, \tilde{b}_{i+4}. \tag{4.69a, b}$$

Here, $\tilde{a}_{1,\dots,4}$ and $\tilde{a}_{5,\dots,8}$ are, respectively, the $\hat{x}$-displacements and $\hat{y}$-displacements at the nodes of a quadrilateral element. Similarly, $\tilde{b}_i$ contains the values of the test function v at the nodes of an element. Letting $\tilde{a} = \{\tilde{a}_1, \cdots, \tilde{a}_8\}^{\mathrm{T}}$, $\tilde{b} = \left\{\tilde{b}_1, \cdots, \tilde{b}_8\right\}^{\mathrm{T}}$ and

$$\boldsymbol{\Phi} = \begin{bmatrix} \phi_1 & \phi_2 & \phi_3 & \phi_4 & 0 & 0 & 0 & 0 \\ 0 & 0 & 0 & 0 & \phi_1 & \phi_2 & \phi_3 & \phi_4 \end{bmatrix}, \tag{4.70}$$

Eqs. (4.69) can be written compactly as
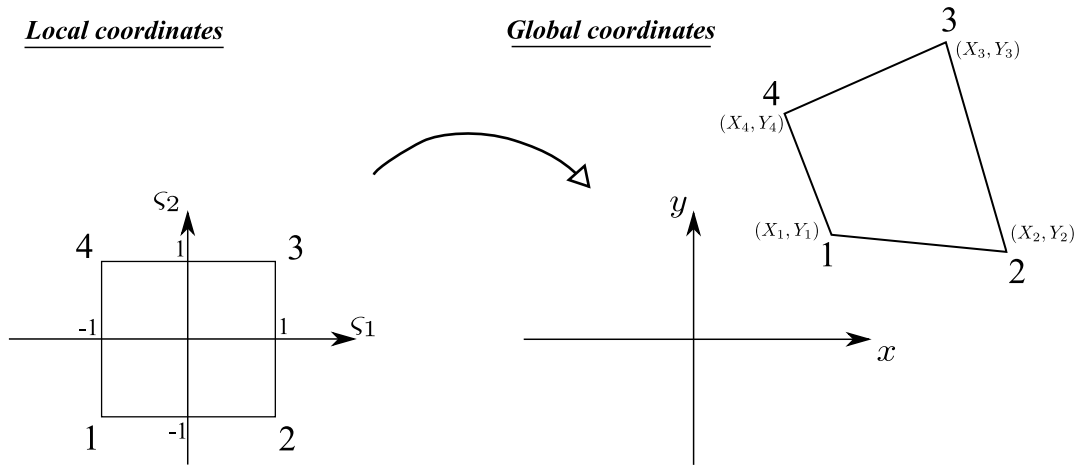
Figure 4.4: Isoparametric mapping.

$$u = \mathbf{\Phi}\,\tilde{a}, \qquad v = \mathbf{\Phi}\,\tilde{b}. \tag{4.71a, b}$$

Shape functions ϕ_i are usually defined using local coordinates ς_1, ς_2 of an element. These coordinates can be mapped onto the global coordinates x, y using isoparametric mapping

$$x(\varsigma_1, \varsigma_2) = \sum_{k=1}^{4} \phi_k(\varsigma_1, \varsigma_2) X_k \qquad y(\varsigma_1, \varsigma_2) = \sum_{k=1}^{4} \phi_k(\varsigma_1, \varsigma_2) Y_k\,. \tag{4.72a, b}$$

Here, $(X_k,\ Y_k)$ defines the $(x,\ y)$ position of the corners in an element and we give a schematic in Figure 4.4 to illustrate isoparametric mapping. In the local coordinates, the shape functions are then defined as follows

$$
\begin{aligned}
\phi_1 &= \frac{1}{4}(1 - \varsigma_1)(1 - \varsigma_2)\,, \\
\phi_2 &= \frac{1}{4}(1 + \varsigma_1)(1 - \varsigma_2)\,, \\
\phi_3 &= \frac{1}{4}(1 + \varsigma_1)(1 + \varsigma_2)\,, \\
\phi_4 &= \frac{1}{4}(1 - \varsigma_1)(1 + \varsigma_2)\,.
\end{aligned}
\tag{4.73}
$$

Discretization of volume integral

Using N_e quadrilateral elements to discretize the material domain $\mathcal{V}$, the leftmost integral given in (4.67) can be discretized and become

$$\sum_{m=1}^{N_e} \int_{\mathcal{V}_m} \sigma_{ij} \, v_{i,j} \, \mathrm{d}\mathcal{V}. \tag{4.74}$$

Using (4.65b), (4.65c) and (4.71), the above integral can be written as

$$\sum_{m=1}^{N_e} \int_{\mathcal{V}_m} \tilde{b}^{[m]\mathrm{T}} \left(\mathbf{D}\boldsymbol{\Phi}^{[m]}\right)^{\mathrm{T}} \mathbf{E}\left(\mathbf{D}\boldsymbol{\Phi}^{[m]}\right) \tilde{a}^{[m]} \, \mathrm{d}\mathcal{V}. \tag{4.75}$$

Here, the superscript $[m]$ is used to denote variables associated with element m. This notation is used in the remaining section. In Eq. (4.75), $\tilde{b}^{[m]}$ and $\tilde{a}^{[m]}$ therefore denote the nodal values of the displacements and test functions in element m. Correspondingly, $(\mathbf{D}\boldsymbol{\Phi})^{[m]}$ and $\mathbf{E}$ are matrices that contain, respectively, spatial derivatives of the shape functions in $\boldsymbol{\Phi}$ evaluated in element m and material constants. These matrices are defined as follows:

$$\mathbf{E} = \begin{bmatrix} \frac{2(1-\nu)}{(1-2\nu)} & \frac{2\nu}{(1-2\nu)} & 0 \\ \frac{2\nu}{(1-2\nu)} & \frac{2(1-\nu)}{(1-2\nu)} & 0 \\ 0 & 0 & 1 \end{bmatrix}, \qquad \mathbf{D}\boldsymbol{\Phi} = \begin{bmatrix} \frac{\partial}{\partial x} & 0 \\ 0 & \frac{\partial}{\partial y} \\ \frac{\partial}{\partial y} & \frac{\partial}{\partial x} \end{bmatrix} \boldsymbol{\Phi}. \tag{4.76a, b}$$

Defining the stiffness matrix of element m as

$$\mathbf{K}^{[m]} = \int_{\mathcal{V}_m} \left(\mathbf{D}\boldsymbol{\Phi}^{[m]}\right)^{\mathrm{T}} \mathbf{E}\left(\mathbf{D}\boldsymbol{\Phi}^{[m]}\right) \mathrm{d}\mathcal{V}, \tag{4.77}$$

the leftmost integral given in (4.67), after substituting (4.77) into (4.75), becomes

$$\sum_{m=1}^{N_e} \tilde{b}^{[m]\mathrm{T}} \mathbf{K}^{[m]} \, \tilde{a}^{[m]}. \tag{4.78}$$

Note: It is easier to evaluate the integral given in (4.77) using the local coordinates ς_1, ς_2.

Discretization of grain boundary integral

Using our previous definition of $\sigma_n = [\sigma_{nn}, \sigma_{ns}]^{\mathrm{T}}$ and noting that $v_n = -\sin\varphi(s)\,\hat{x} + \cos\varphi(s)\,\hat{y}$, $v_s = \cos\varphi(s)\,\hat{x} + \sin\varphi(s)\,\hat{y}$, we can re–write the second integral in (4.67) in a more compact form

$$\int_{\mathcal{S}_I} \sigma_{nn}v_n + \sigma_{ns}v_s \, \mathrm{d}s = \int_{\mathcal{S}_I} v^{\mathrm{T}} \mathbf{R}^{\mathrm{T}} \sigma_n \, \mathrm{d}s \tag{4.79a}$$
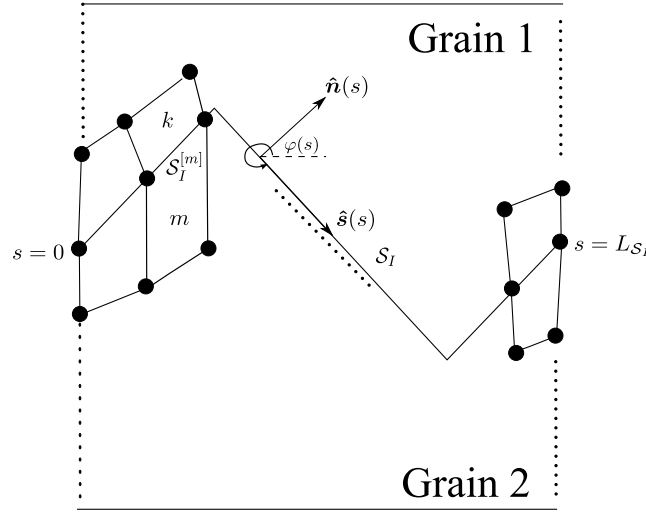
Figure 4.5: Finite element discretization along $\mathcal{S}_I$.

where

$$\mathbf{R} = \begin{pmatrix} -\sin\varphi(s) & \cos\varphi(s) \\ \cos\varphi(s) & \sin\varphi(s) \end{pmatrix}. \tag{4.79b}$$

Figure 4.5 illustrates the finite element discretization of the grain boundary $\mathcal{S}_I$. That boundary is shared by elements in grain 1 and grain 2, and correspondingly, each black dot ● along $\mathcal{S}_I$ in the figure represents two coinciding nodes (from grain 1 and 2). Letting $\mathbb{E}_{\mathcal{S}_1}$ be the set of elements $m \in$ grain 1 having boundary $\mathcal{S}_I^{[m]} \subset \mathcal{S}_I$, and $\mathbb{E}_{\mathcal{S}_2}$ be the corresponding set of elements $k \in$ grain 2 having boundary $\mathcal{S}_I^{[m]}$, the discretized form of (4.79), and hence of the second integral in (4.67), is given as

$$\sum_{m \in \mathbb{E}_{\mathcal{S}_1}} \int_{\mathcal{S}_I^{[m]}} \tilde{b}^{[m]\mathrm{T}} \mathbf{\Phi}^{[m]\mathrm{T}} \mathbf{R}^{\mathrm{T}} \sigma_n \, \mathrm{d}s + \sum_{k \in \mathbb{E}_{\mathcal{S}_2}} \int_{\mathcal{S}_I^{[m]}} \tilde{b}^{[k]\mathrm{T}} \mathbf{\Phi}^{[k]\mathrm{T}} \mathbf{R}^{\mathrm{T}} \sigma_n \, \mathrm{d}s. \tag{4.80}$$

Discretization of periodic boundary condition

Figure 4.6 illustrates the finite element discretization along the $x = 0$ and $x = 2\pi$. For simplicity in imposing periodic boundary condition, we create a mesh so that there is a one to one correspondence between element m that has a boundary on $x = 0$ and element k that has a boundary on $x = 2\pi$. The two nodes of element m on $x = 0$ are separated horizontally from the two nodes of element k on $x = 2\pi$ by a distance 2π. Denoting $\mathbb{E}_{\Gamma_L}$ and
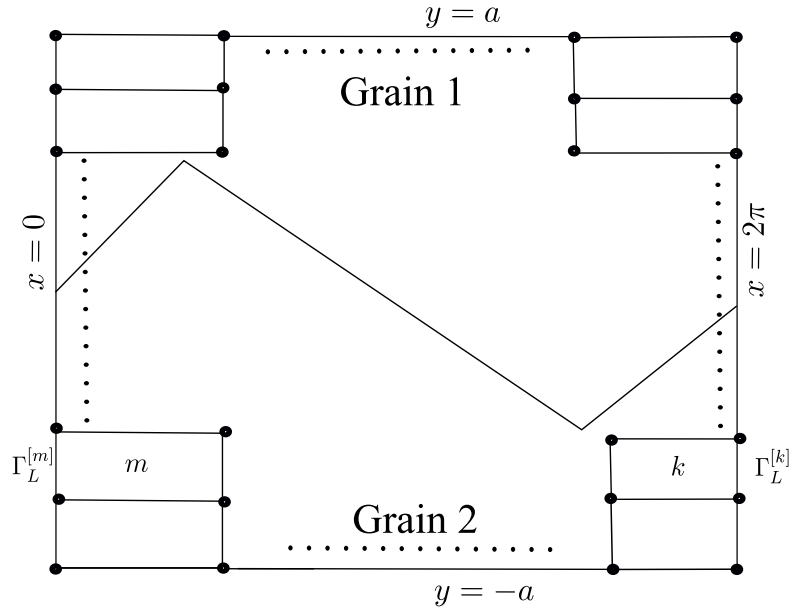
Figure 4.6: Finite element discretization on $x = 0$, $x = 2\pi$.

$\mathbb{E}_{\Gamma_R}$ be corresponding sets of elements m and k having boundaries $\Gamma_L^{[m]}$ on $x = 0$ and $\Gamma_R^{[k]}$ on $x = 2\pi$ respectively, the 3rd integral in (4.67), after substituting from (4.71), is discretized into

$$
P \sum_{m \in \mathbb{E}_{\Gamma_L}} \int_{\Gamma_L^{[m]}} \tilde{b}^{[m]^{\mathrm{T}}} \mathbf{\Phi}^{[m]^{\mathrm{T}}} \left(\mathbf{\Phi}^{[m]} \tilde{a}^{[m]} - \mathbf{\Phi}^{[k]} \tilde{a}^{[k]} \right) \mathrm{d}y
$$
$$
+ P \sum_{k \in \mathbb{E}_{\Gamma_R}} \int_{\Gamma_L^{[k]}} \tilde{b}^{[k]^{\mathrm{T}}} \mathbf{\Phi}^{[k]^{\mathrm{T}}} \left(\mathbf{\Phi}^{[k]} \tilde{a}^{[k]} - \mathbf{\Phi}^{[m]} \tilde{a}^{[m]} \right) \mathrm{d}y .
$$
(4.81)

Because the $\hat{y}$–coordinates defining elemental boundaries $\Gamma_L^{[m]}$ and $\Gamma_R^{[k]}$ are identical, the two integrals in (4.81) can be combined and the resultant can be written more compactly as

$$
\sum_{m \in \mathbb{E}_{\Gamma_L}} \begin{pmatrix} \tilde{b}^{[m]} \\ \tilde{b}^{[k]} \end{pmatrix}^{\mathrm{T}} \mathbf{K}_p^{[m]} \begin{pmatrix} \tilde{a}^{[m]} \\ \tilde{a}^{[k]} \end{pmatrix} ,
$$
(4.82a)

where $\mathbf{K}_p^{[m]}$ is the penalty matrix for enforcing periodic boundary conditions and is given by

$$
\mathbf{K}_p^{[m]} = P \int_{\Gamma_L^{[m]}} \begin{pmatrix} \mathbf{\Phi}^{[m]^{\mathrm{T}}} \mathbf{\Phi}^{[m]} & -\mathbf{\Phi}^{[m]^{\mathrm{T}}} \mathbf{\Phi}^{[k]} \\ -\mathbf{\Phi}^{[k]^{\mathrm{T}}} \mathbf{\Phi}^{[m]} & \mathbf{\Phi}^{[k]^{\mathrm{T}}} \mathbf{\Phi}^{[k]} \end{pmatrix} \mathrm{d}y .
$$
(4.82b)

Discretization of displacement boundary condition

The final integral given in (4.67) of the displacement boundary conditions is discretized here. Denoting $\mathbb{E}_{\Gamma_T}$ and $\mathbb{E}_{\Gamma_B}$ be sets of elements m and k having boundaries $\Gamma_T^{[m]}$ on $y = a$ and $\Gamma_B^{[k]}$ on $y = -a$, respectively, the final integral in (4.66), after substituting from (4.72), becomes

$$P \sum_{m \in \mathbb{E}_{\Gamma_T}} \int_{\Gamma_T^{[m]}} \tilde{b}^{[m]\mathrm{T}} \Phi^{[m]\mathrm{T}} \Phi^{[m]} \tilde{a}^{[m]} - \tilde{b}^{[m]\mathrm{T}} \Phi^{[m]\mathrm{T}} U \, \mathrm{d}x$$
$$+ P \sum_{k \in \mathbb{E}_{\Gamma_B}} \int_{\Gamma_B^{[k]}} \tilde{b}^{[k]\mathrm{T}} \Phi^{[k]\mathrm{T}} \Phi^{[k]} \tilde{a}^{[k]} + \tilde{b}^{[k]\mathrm{T}} \Phi^{[k]\mathrm{T}} U \, \mathrm{d}x \,. \tag{4.83}$$

Defining the $\mathbf{K}_d^{[m]}$ and $\mathbf{K}_d^{[k]}$ as the penalty matrices used to enforce displacement boundary conditions at $y = a$ and $y = -a$, respectively, i.e.

$$\mathbf{K}_d^{[m]} = P \int_{\Gamma_T^{[m]}} \Phi^{[m]\mathrm{T}} \Phi^{[m]} \, \mathrm{d}x \,, \qquad \mathbf{K}_d^{[k]} = P \int_{\Gamma_T^{[k]}} \Phi^{[k]\mathrm{T}} \Phi^{[k]} \, \mathrm{d}x \,; \tag{4.84a,b}$$

Eq. (4.83) can be written more compactly as

$$\sum_{m \in \mathbb{E}_{\Gamma_T}} \tilde{b}^{[m]\mathrm{T}} \mathbf{K}_d^{[m]} \tilde{a}^{[m]} + \sum_{k \in \mathbb{E}_{\Gamma_B}} \tilde{b}^{[k]\mathrm{T}} \mathbf{K}_d^{[k]} \tilde{a}^{[k]}$$
$$+ \sum_{m \in \mathbb{E}_{\Gamma_T}} P \int_{\Gamma_T^{[m]}} \tilde{b}^{[m]\mathrm{T}} \Phi^{[m]\mathrm{T}} U \, \mathrm{d}x + \sum_{m \in \mathbb{E}_{\Gamma_B}} P \int_{\Gamma_B^{[k]}} \tilde{b}^{[k]\mathrm{T}} \Phi^{[k]\mathrm{T}} U \, \mathrm{d}x \tag{4.85}$$

to give the discretized form of the final integral in (4.67).

4.5.3 Linear system of equations

Replacing the integrals in the weak formulation (4.67) by the discretized form given in (4.78), (4.80), (4.82) and (4.85), and then further imposing the condition that $\tilde{b}$ is arbitary (because the test function v is arbitrary) leads to a linear system of equations with the nodal displacements $\tilde{a}$ as unknowns. For details of assemblying the linear system of equations, refer to Zienkiewicz & Taylor [42]. We use a parallel sparse solver PARDISO from Intel®Fortran Compiler to solve that system of equations with penalty parameter $P \sim O(10^5)$. In a typical run using 2642700 nodes and 2638104 elements, which results in 5285400 number of degree of freedom, solving that system of equations with PARDSIO using 8 CPU of 3.00GHz and 16GB of memory takes about 4.5 minutes.

4.5.4 Elastically–accommodated grain boundary sliding

The b.v.p. of elastically–accommodated grain boundary sliding posed below (3.10) is solved using finite element method. This b.v.p. differs from the previous only in terms of the constitutive equations along the interface $\mathcal{S}_I$. The weak form of that b.v.p. is given as follows:

$$\int_{\mathcal{V}} \sigma_{ij} v_{i,j} \, \mathrm{d}\mathcal{V} - \underbrace{\int_{\mathcal{S}_I} \mathrm{i}\omega [u_s] v_s \, \mathrm{d}s}_{\text{b.c. (3.10b)}} + \underbrace{P \int_{\mathcal{S}_I} [u_n] v_n \, \mathrm{d}s}_{\text{b.c. (3.10a)}}$$

$$+ P \underbrace{\int_{-a}^{a} \{u_i(0,y) - u_i(2\pi,y)\} v_i(0,y) + \{u_i(2\pi,y) - u_i(0,y)\} v_i(2\pi,y) \, \mathrm{d}y}_{\text{periodic b.c.}} \tag{4.86}$$

$$+ P \underbrace{\int_{0}^{2\pi} \{u_i(x,a) - U_i\} v_i(x,a) + \{u_i(x,-a) + U_i)\} v_i(x,-a) \, \mathrm{d}x}_{\text{displacement b.c.}} = 0 \, .$$

In Eq. (4.86), the imposed displacements are $U_1 = 1$ and $U_2 = 0$. Comparing the weak form given here with that given in (4.67), we find that only the second integral in the latter equation is replaced by $\int_{\mathcal{S}_I} \mathrm{i}\omega [u_s] v_s + P [u_n] v_n \, \mathrm{d}s$. Consequently, the discretization of the volume integral, the periodic boundary condition and the displacement boundary conditions are the same with those given in the previous sub–sections. We now give the discretization of the second and the third integrals of (4.86).

Based on the grain boundary element discretization illustrated in Figure 4.5 and using the notation given below that figure, the second integral given in (4.86) in discretized form becomes

$$\mathrm{i}\omega \sum_{m \in \mathbb{E}_{\mathcal{S}_1}} \int_{\mathcal{S}_I^{[m]}} \tilde{b}^{[m]^\mathrm{T}} \mathbf{\Phi}^{[m]^\mathrm{T}} \hat{s}^\mathrm{T} \hat{s} \left(\mathbf{\Phi}^{[m]} \, \tilde{a}^{[m]} - \mathbf{\Phi}^{[k]} \, \tilde{a}^{[k]} \right) \mathrm{d}s$$

$$+ \mathrm{i}\omega \sum_{k \in \mathbb{E}_{\mathcal{S}_2}} \int_{\mathcal{S}_I^{[m]}} \tilde{b}^{[k]^\mathrm{T}} \mathbf{\Phi}^{[k]^\mathrm{T}} \hat{s}^\mathrm{T} \hat{s} \left(\mathbf{\Phi}^{[k]} \, \tilde{a}^{[k]} - \mathbf{\Phi}^{[m]} \, \tilde{a}^{[m]} \right) \mathrm{d}s \, . \tag{4.87}$$

We note here that the 2×2 matrix $\hat{s}^\mathrm{T} \hat{s}$ is an outcome of the product between $u_s = \hat{s}^\mathrm{T} \mathbf{\Phi} \, \tilde{a}$ and $v_s = \hat{s}^\mathrm{T} \mathbf{\Phi} \, \tilde{b}$. Noting that there is a one to one correspondence between element m in

$\mathbb{E}_{\mathcal{S}_1}$ and element k in $\mathbb{E}_{\mathcal{S}_2}$, the discretized form given in (4.87) can be written compactly as

$$\sum_{m \in \mathbb{E}_{\mathcal{S}_1}} \begin{pmatrix} \tilde{b}^{[m]} \\ \tilde{b}^{[k]} \end{pmatrix}^{\mathrm{T}} \mathbf{K}_{\mathrm{s}}^{[m]} \begin{pmatrix} \tilde{a}^{[m]} \\ \tilde{a}^{[k]} \end{pmatrix}, \tag{4.88a}$$

where $\mathbf{K}_{\mathrm{s}}^{[m]}$ is the penalty matrix used to enforce the periodic boundary conditions given below by

$$\mathbf{K}_{\mathrm{s}}^{[m]} = \mathrm{i}\omega \int_{\mathcal{S}_I^{[m]}} \begin{pmatrix} \boldsymbol{\Phi}^{[m]\mathrm{T}} \hat{s}^{\mathrm{T}} \hat{s}\, \boldsymbol{\Phi}^{[m]} & -\boldsymbol{\Phi}^{[m]\mathrm{T}} \hat{s}^{\mathrm{T}} \hat{s}\, \boldsymbol{\Phi}^{[k]} \\ -\boldsymbol{\Phi}^{[k]\mathrm{T}} \hat{s}^{\mathrm{T}} \hat{s}\, \boldsymbol{\Phi}^{[m]} & \boldsymbol{\Phi}^{[k]\mathrm{T}} \hat{s}^{\mathrm{T}} \hat{s}\, \boldsymbol{\Phi}^{[k]} \end{pmatrix} \mathrm{d}s. \tag{4.88b}$$
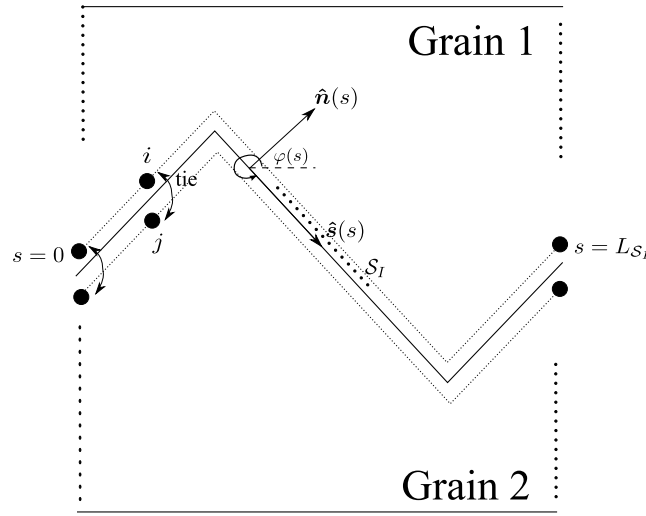

Figure 4.7: Enforcing continuous normal displacement between $i \in$ grain 1 and $j \in$ grain 2

For simplicity, we enforce boundary condition (3.10a) given by the third integral of (4.86) directly on the nodes. Figure 4.7 illustrates how that boundary condition is enforced. In the figure, the interfacial node $i \in$ grain 1 is tied directly to the corresponding interfacial node $j \in$ in grain 2. We note that i and j have the same coordinates on $\mathcal{S}_I$. We also let $\mathbb{N}_{\mathcal{S}_1}$ be the set of nodes $i \in$ grain 1 on $\mathcal{S}_I$ and $\mathbb{N}_{\mathcal{S}_2}$ to be the corresponding set of nodes $j \in$ grain 2 on $\mathcal{S}_I$. Denoting $\tilde{a}^{\{i\}}$ and $\tilde{b}^{\{i\}}$ respectively as the 2×1 displacement vector $\boldsymbol{u}$ and test function vector $\boldsymbol{v}$ at node i, the third integral in (4.86) can be discretized to become

$$P \sum_{i \in \mathbb{N}_{\mathcal{S}_1}} \begin{pmatrix} \tilde{b}^{\{i\}} \\ \tilde{b}^{\{j\}} \end{pmatrix}^{\mathrm{T}} \mathbf{K}_{\mathrm{n}}^{\{i\}} \begin{pmatrix} \tilde{a}^{\{i\}} \\ \tilde{a}^{\{j\}} \end{pmatrix}; \tag{4.89a}$$

where

$$\mathbf{K}_{\mathrm{n}}^{\{i\}} = \begin{pmatrix} \hat{\boldsymbol{n}}^{\mathrm{T}}\hat{\boldsymbol{n}} & -\hat{\boldsymbol{n}}^{\mathrm{T}}\hat{\boldsymbol{n}} \\ -\hat{\boldsymbol{n}}^{\mathrm{T}}\hat{\boldsymbol{n}} & \hat{\boldsymbol{n}}^{\mathrm{T}}\hat{\boldsymbol{n}} \end{pmatrix}. \tag{4.89b}$$

Here, the sub–matrices $\hat{\boldsymbol{n}}^{\mathrm{T}}\hat{\boldsymbol{n}}$ are 2×2 matrix and $\mathbf{K}_{\mathrm{n}}^{\{i\}}$ is, therefore, a 4×4 matrix.

A linear system of equations can be obtained by replacing the integrals in the weak formulation (4.86) with the discretized form given in (4.78), (4.82), (4.85), (4.88) and (4.89) and then imposing the condition that $\tilde{b}$ is arbitrary. This system of equation is complex because the boundary condition (3.10b) contains a time–derivative.

Chapter 5

Diffusionally-accommodated grain boundary sliding

Here we discuss the numerical results from the bicrystal model of diffusionally–accommodated grain boundary sliding. To begin, we derive analytical constraints in §5.1 to the mechanical loss spectrum for which the numerical solution must satisfy. These constraints are, specifically, the high and low frequency asymptotes to the spectrum.

In §5.2, we discuss our numercal results and show that they satisfy all the constraints set forth previously. We show that the mechanical loss spectrum contains a band of frequencies where the mechanical loss $\mathcal{L}$ decreases slowly with frequency ω when the timescales are widely separated i.e. $\mathcal{M} \ll 1$. That slowly–varying region is caused by corner stress concentrations and is sensitive to slope angle. For the two orthogonal sliding modes found in a regular array of hexagonal grains (see Figure 3.2), we show that the mechanical loss $\mathcal{L}$ varies approximately as $\omega^{-0.3}$. Beyond that slowly–varying region, the mechanical loss spectrum contains a mechanical loss peak that stands out from the absorption background.

We also extend our analysis to consider the effects of varying corner angles along a sliding interface on the slowly–varying region. We show that as a result of that variation, the slope of the mechanical loss spectrum decreases gradually and is eventually controlled by the corner having the most singular stress behaviour.

In §5.3, we compare the mechanical loss spectrum obtained from the bicrystal model with that from the experiments. We show that the mechanical loss scaling in the

slowly–varying region for the two orthogonal sliding modes found in an array of hexagonal grains is close to the scaling observed experimentally. We also give evidence to support our explanation that the scaling seen in the experiments is likely to be controlled by corner stress concentration at triple junctions. Though we are able to predict the loss scaling in the experiments using the bicrystal model, the magnitude of the mechanical loss $\mathcal{L}$ found using that model is still an order of magnitude less than that observed in the experiments. Thus, a numerical model that allows for the concurrent sliding along multiple planes in a polycrystal is necessary in order to predict the magnitude of the loss seen in the experiments.

5.1 Analytical constraints on the numerical solution

Here, we develop analytical constraints for which our numerical solution has to satisfy. We follow the scaling analysis found in Morris & Jackson [26] to derive the behaviour of the mechanical loss spectrum by evaluating the strain energy and the dissipation directly.

For the bicrystal system shown in Figure 3.1, the external power supplied at the sample boundaries is either dissipated at the time–independent grain interface $\mathcal{S}_I$ or stored as strain energy within the perfectly elastic grains, i.e.

$$4\pi\tau\frac{\mathrm{d}U}{\mathrm{d}t} = \dot{\Upsilon} + \frac{\mathrm{d}W}{\mathrm{d}t} \; ; \tag{5.1a}$$

$$W = \int_{\mathcal{V}} \left\{ \frac{\nu}{1-2\nu}e_{kk}^2 + e_{ij}^2 \right\} \mathrm{d}\mathcal{V}, \tag{5.1b}$$

$$\dot{\Upsilon} = \int_{\mathcal{S}_I} \frac{1}{\mathcal{M}}\sigma_{ns}^2 + \left(\frac{\mathrm{d}\sigma_{nn}}{\mathrm{d}s}\right)^2 \mathrm{d}s, \tag{5.1c}$$

define the strain energy function $W(t)$ and the dissipation rate $\dot{\Upsilon}(t)$. Here, $\mathcal{V}$ is the combined volume of the upper and the lower grains and τ is the x–averaged shear stress defined in (3.11).

5.1.1 Low–frequency asymptote

The low frequency (i.e. $\omega \ll 1$) behaviour of the mechanical loss $\mathcal{L}$ has been established in Morris & Jackson [26]. Because diffusion acts over the entire bicrystal

system at low frequencies, the strain energy function W and the dissipation rate $\dot{\Upsilon}$ do not depend on frequency ω. As a result, the time available for dissipation varies inversely with ω and the mechanical loss at low frequencies scales as

$$\mathcal{L} \sim \omega^{-1}. \tag{5.2}$$

Physically for $\omega \to 0$, the quality factor $Q = \mathcal{L}^{-1}$ is proportional to ω as one might expect from Taylor's theorem.

5.1.2 High–frequency asymptote

In the limiting case as $\omega \to \infty$, the displacement becomes continuous across the interface $\mathcal{S}_I$, i.e. $[u_n] = 0 = [u_s]$. However when the timescales are widely separated i.e. $\mathcal{M} \ll 1$, discontinuity in the normal displacement $[u_n] \to 0$ faster than the discontinuity in the tangential displacement $[u_s]$ as $\omega \to \infty$. The latter term therefore dominates the former. Correspondingly, the dissipation rate $\dot{\Upsilon}$ in (5.1c) is controlled by the shear stress σ_{ns} in the high frequency extreme and can be calculated by evaluating only the first term in the r.h.s of (5.1c).

The tangential shear σ_{ns} can be evaluated directly because the two grains behave as if they are welded at the interface in the limit as $\omega \to \infty$. As a result the sample deforms under simple shear and the stress components become $\sigma_{xy} = \tau$ and $\sigma_{xx} = 0 = \sigma_{yy}$. By the discussion following (3.10b), we may assume that $\tau(t) = \hat{\tau} \sin \omega t$ where the amplitude $\hat{\tau}$ is independent of t. Noting that the shear stress is given by $\sigma_{ns} = \tau \cos 2\varphi$ at the interface $\mathcal{S}_I$ under simple shear, we evaluate the dissipation rate $\dot{\Upsilon}$ and then integrate the resultant with respect to time t over one period i.e. from $t = 0$ to $t = 2\pi/\omega$ to show that

$$\Upsilon \sim \hat{\tau}^2 \frac{\pi}{\mathcal{M}\omega} \int_{\mathcal{S}_I} \cos^2 2\varphi \, ds. \tag{5.3}$$

The time mean strain energy $\bar{W}$ of the system can be obtained by using Hooke's law to evaluate (5.1b) and then time–averaging the resultant expression. The asymptotic expression of the time mean strain energy is given by

$$\bar{W} \sim \pi a \hat{\tau}^2. \tag{5.4}$$

Using (5.4), (5.3), and the interpretation of $\mathcal{L}$ given below (3.13), we find that in the limit as $\omega \to \infty$, $\mathcal{L}$ is given asymptotically by

$$\mathcal{L} \sim \frac{1}{2a\mathcal{M}\omega} g(\varphi); \tag{5.5a}$$

$$g(\varphi) = \frac{1}{2\pi} \int_{\mathcal{S}_I} \cos^2 2\varphi \, \mathrm{d}s. \tag{5.5b}$$

The geometric factor $g(\varphi)$ depends only on interface geometry. This quantity is a measure of the slip along the interface; in the limit $\omega \to \infty$, the amplitude of $\int [u_s]^2 \, \mathrm{d}s$ is proportional to g/ω^2. Evaluating (5.5b) for the type S and type TS interfaces shown in Figure 3.2, we find that

$$g = \begin{cases} \cos^2 2\varphi / \cos \varphi, & \text{type } S; \\ \frac{1}{2}(1 + \cos^2 2\varphi / \cos \varphi), & \text{type } TS, \end{cases} \tag{5.6}$$

The geometric factor varies inversely with $\cos \varphi$ because for fixed wavelength, the interface length increases with slope.

5.1.3 Sliding Peak

When the timescales are widely separated i.e. $\mathcal{M} \ll 1$, the effects of diffusion at high frequencies become negligibly small and the dissipation Υ is controlled by the boundary viscosity η. The b.v.p. then simplifies to that describing elastically–accommodated grain boundary sliding. For that case, which will be discuss further in chapter 6, the mechanical loss $\mathcal{L}$ is predicted to have a maximum in the spectrum at an angular frequency $\omega^* \sim t_\eta^{-1}$, or equivalently at the non-dimensional frequency $\omega \sim \mathcal{M}^{-1}$.

5.1.4 High frequency behaviour for $\mathcal{M} \to 0$

In the limiting state: $\mathcal{M} \to 0$, the interface $\mathcal{S}_I$ becomes inviscid i.e. $\sigma_{ns} = 0$ and the loss peak located at $\omega \sim \mathcal{M}^{-1}$ shifts into the high frequency extreme $\omega \to \infty$. The peak thus vanishes from the mechanical loss spectrum, and the features located within the band of frequencies $1 \ll \omega \ll \mathcal{M}^{-1}$ are extended towards the entire r.h.s of the spectrum. These features are study here.

For small slope angle φ, the high frequency behaviour of the mechanical loss $\mathcal{L}$ for an inviscid interface i.e. $\mathcal{M} \to 0$ is given in Morris & Jackson [26]. At high frequencies $\omega \to \infty$, the mechanical loss $\mathcal{L}$ varies as $1/\ln \omega$ when the interface has sharp corners. This result is an outcome of corner stress concentration, where the normal stress σ_{nn} varies inversely with distance r from the corner in the limit $\omega \to \infty$.

For finite slope φ, the form of the corner stress concentration changes and the small–slope logarithmic scaling no longer holds. Because the interfacial boundary conditions (3.8d) and (3.8e) approach those used in a local stress analysis by Picu & Gupta [33] : $[u_n] = 0 = \sigma_{ns}$ as $\omega \to \infty$, the interfacial normal stress σ_{nn} (in that limiting state) has to behave as described by them and is given by

$$\sigma_{nn} \sim r^{-\lambda} . \tag{5.7}$$

In Eq. (5.7), the stress exponent λ is a function of the corner angle and is restricted by $1 > \lambda > 0$. The first inequality ensures that the strain energy of the bicrystal system remains finite whereas the second inequality follows because stress is singular at $r = 0$ for sharp corners.
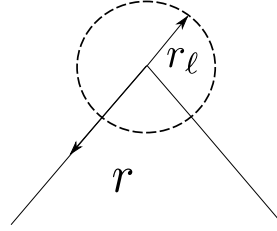

Figure 5.1: Definition sketch to describe corner singularity

In our model, the interfacial normal stress σ_{nn} is not singular at the corners as a result of either diffusion (occurring at finite ω) or geometric rounding of the corners. Letting r_ℓ be the distance over which σ_{nn} is smoothed (See Figure 5.1), there is a separation of lengthscales when $r_\ell \ll d$. Under that condition, σ_{nn} varies with r according to (5.7) at distance $r_\ell \ll r \ll d$ and the cut–off length r_ℓ determines the form of the loss spectrum. Using (5.7) to estimate the strain energy W in (5.1b) and the dissipation Υ in (5.1c), we find that they vary as

$$W \sim \int_{r_\ell}^{d} \sigma_{nn}^2 r \, \mathrm{d}r \sim 1 - \left(\frac{r_\ell}{d}\right)^{2-2\lambda} , \tag{5.8a}$$

$$\Upsilon \sim \frac{1}{\omega} \int_{r_\ell}^{d} \left(\frac{\mathrm{d}\sigma_{nn}}{\mathrm{d}r}\right)^2 \, \mathrm{d}r \sim \frac{1}{\omega} \left(\frac{d}{r_\ell}\right)^{1+2\lambda} . \tag{5.8b}$$

We note that r appears in the integrand in Eq. (5.8a) because the integration is carried out over an annular region defined by $r_\ell < r < d$. The resultant strain energy function W in (5.8a) is found to be insensitive to r_ℓ because $\lambda < 1$ and the lengthscales are widely separated i.e. $r_\ell \ll d$. The last condition $d/r_\ell \gg 1$ has also been used to obtain the final expression in (5.8b). According to the interpretation of mechanical loss $\mathcal{L}$ as the ratio of Υ to W given below (3.13), $\mathcal{L}$ is thus controlled by the dissipation Υ through the cut–off length r_ℓ and the stress exponent λ. The length r_ℓ can be set either by diffusion or by an imposed corner radius r_c.

In the first case, the cut off length r_ℓ is set by the diffusive lengthscale $\ell_d \sim \omega^{-1/3}$ defined in (3.6). Replacing r_ℓ in (5.8b) by ℓ_d , we find that the behaviour of the mechanical loss in the spectrum can be described using a power–law relation

$$\mathcal{L} \sim \omega^\alpha \tag{5.9a}$$

where

$$\alpha = \frac{2}{3}(\lambda - 1) \ . \tag{5.9b}$$

Eq. (5.9) holds except for a type S interface with slope angle $\varphi = 45°$. For that angle, the interface coincides with the direction of the principal stresses as described in 6.1.1. As a result, the grains are deformed under simple shear with interfacial normal stress $\sigma_{nn} \to \pm\tau$ at high frequencies. Because σ_{nn} approaches a constant as $\omega \to \infty$, the stress exponent $\lambda = 0$. Substituting that value of λ into (5.9), we find that the mechanical loss $\mathcal{L}$ varies as $\omega^{-2/3}$ for this specific interface.

In the second case, the cut–off length r_ℓ is imposed by the geometric rounding of corners. That occurs when the corner radius $r_c > \ell_d$, or equivalently when $\omega \gg (d/r_c)^3$. Unlike the diffusive lengthscale ℓ_d, the corner radius r_c (and d/r_c) does not depend on frequency. Consequently, the dissipation Υ in (5.8b) and the mechanical loss $\mathcal{L}$ varies as ω^{-1}. That scaling applies to all interfaces when $\omega \gg (d/r_c)^3$.

5.1.5 Features in the mechanical loss spectrum

Figure 5.2 summarizes the main features in the loss spectrum predicted by the scaling arguments given above. If the frequencies defining each region of the spectrum are

widely separated (i.e. $1 \ll (d/r_c)^3 \ll \mathcal{M}^{-1}$), the mechanical loss $\mathcal{L}$ should scale accordingly as defined in the figure. We test that prediction in §5.2.
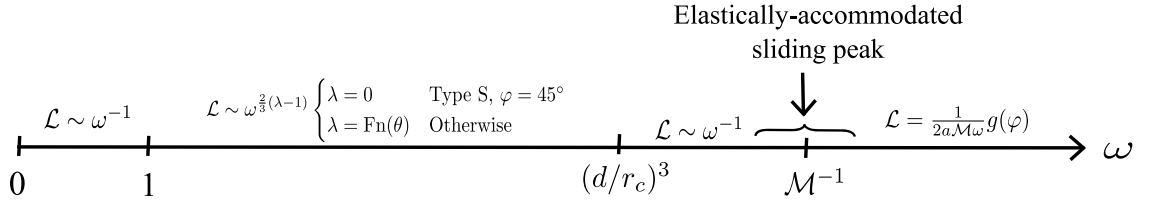

Figure 5.2: Schematic of the mechanical loss spectrum

5.2 Discussion of numerical results

Figure 5.3 shows the shear rigidity G computed as a function of the angular frequency ω with $\mathcal{M}$ as a parameter for a type S interface with $\varphi = 30°$. That interface has a wavelength to corner radius ratio $N \sim 100$. The mechanical loss spectrum $\mathcal{L} = \tan \arg G$ and the sample rigidity $|G|$ are shown, respectively, in the upper and lower figures.

Figure 5.3a confirms the prediction summarized in Figure 5.2: that if the band of frequencies that define each region are widely separated, all features predicted in §5.1 are present in the mechanical loss spectrum. That result is shown by the curve for $\mathcal{M} = 10^{-13}$. For $\omega \ll 1$, the mechanical loss $\mathcal{L}$ varies as ω^{-1}. At higher frequencies $1 \ll \omega \ll 10^6$, corner stress concentrations control the spectrum. For that interface with corners subtending at an angle equal to $120°$, we find that the mechanical loss $\mathcal{L} \sim \omega^{-0.3}$ for that band of frequencies. With this value of power–law exponent $\alpha = -0.3$, the stress exponent calculated from (5.9) has a value $\lambda = 0.55$, close to the prediction of $\lambda = 0.58$ given by the local solution of Picu & Gupta [33] in their Figure 5.[1] To make that comparison, we have used the stress exponent associated with that of an anti–symmetric stress field about the corner because our solution (see Figure 5.6) shows that σ_{nn} is anti–symmetric about the corner. Subsequently at even higher frequencies $10^7 \ll \omega \ll 10^8$, the diffusion lengthscale ℓ_d become smaller than the corner radius r_c. As a result, stresses are smoothed over by a distance $\sim r_c$ and the mechanical loss, as described above §5.1.5, then scales as $\mathcal{L} \sim \omega^{-1}$.

[1]Note: In Figure 5 of Picu & Gupta [33], the curve labels are switched i.e. the dashed and the solid lines should correspond to the symmetric eigenfunction and the anti–symmetric eigenfunction, respectively. Also in Figure 6, the eigenvectors in (a) and (b) should correspond, respectively, to the anti–symmetric fields and the symmetric fields instead.
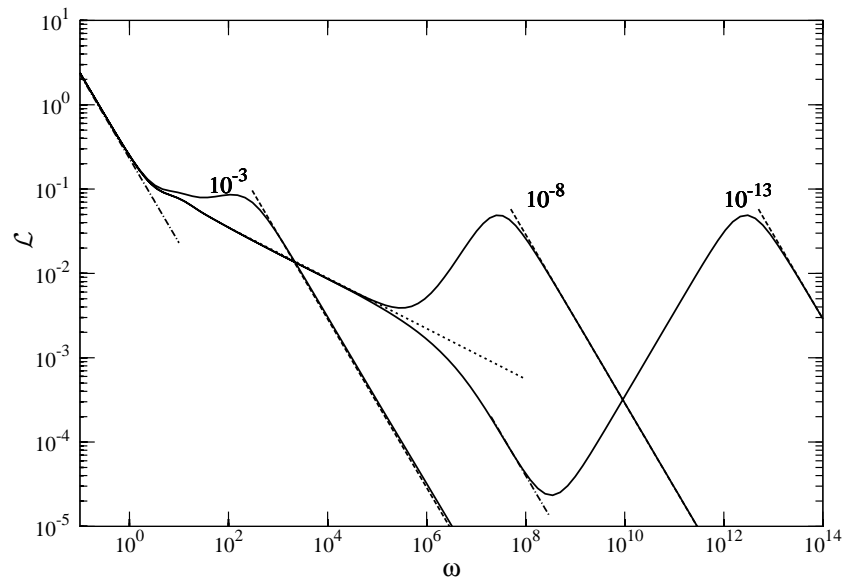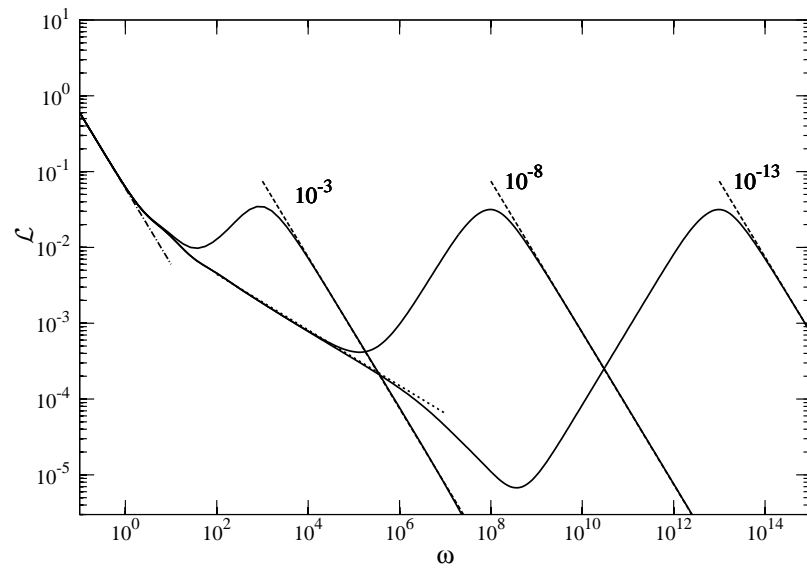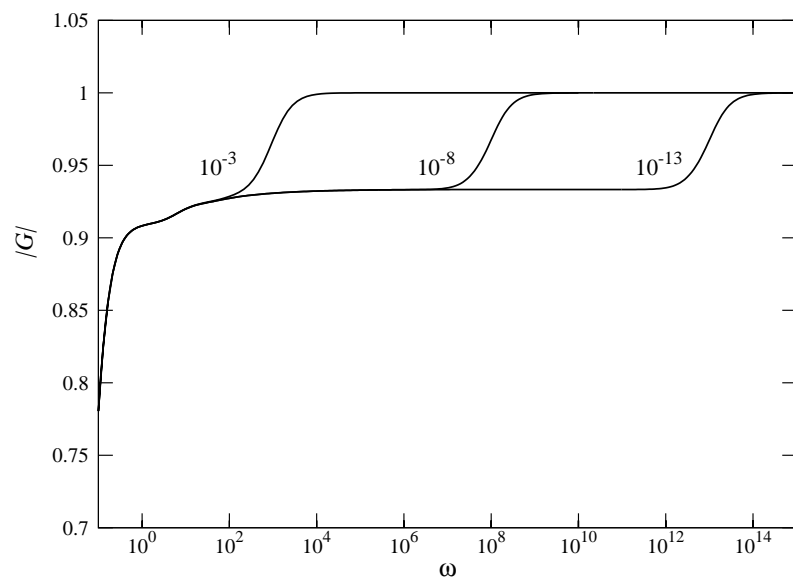
(a) $\mathcal{L}$
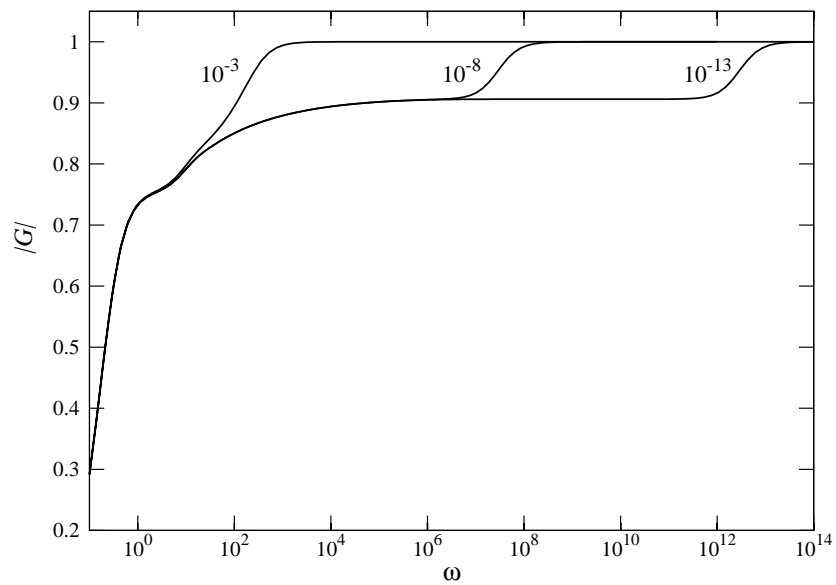
(b) $|G|$

Figure 5.3: Rigidity as a function of ω with $\mathcal{M}$ as a parameter. Type S interface, $N = 100$, $a = 5$, $\varphi = 30°$, $\nu = 0.3$. (a) $\mathcal{L} = \tan \arg G$; (b) $|G|$. Curve labels give values of $\mathcal{M}$. - - - - - asymptote Eq. (5.5). ·········· asymptote Eq. (5.9). –·–·–· asymptote Eq. (5.2).

(a) $\mathcal{L}$

(b) $|G|$

Figure 5.4: Rigidity as a function of ω with $\mathcal{M}$ as a parameter. Type *TS* interface, $N = 100$, $\varphi = 60°$. (a) $\mathcal{L} = \tan \arg G$; (b) $|G|$. Curve labels give values of $\mathcal{M}$. - - - - - asymptote Eq. (5.5). ·········· asymptote Eq. (5.9). – · – · – asymptote Eq. (5.2). Refer to Figure 5.3 for other parameters.

Lastly, a local maximum due to elastically–accommodated grain boundary sliding is found at $\omega \sim 10^{-13}$ and the mechanical loss $\mathcal{L}$ varies according to (5.5) after the peak. That peak has a magnitude of about 0.05 that is invariant with $\mathcal{M}$.

The peak and the slowly varying region is, however, not present in the curve for $\mathcal{M} = 10^{-3}$ because the timescales are not widely separated. As a result, the mechanical loss $\mathcal{L}$ decreases rapidly as ω^{-1} in most parts of the spectrum. For that same reason, the region at which the corner radius sets the cut-off lengthscale (i.e. $(d/r_c)^3 \ll \omega \ll \mathcal{M}^{-1}$) is not found when $\mathcal{M} = 10^{-8}$. Instead, the loss peak follows immediately after the slowly–varying region $(1 \ll \omega \ll 10^6)$ in the mechanical loss spectrum.

In Figure 5.3b, we show that the corresponding sample rigidity for the loss spectrum obey the physical constraint $|G| \leq 1$: that the sample cannot be made stronger than the individual grains. The figure shows that as frequency $\omega \to \infty$, the sample rigidity $|G|$ approaches unity because the two grains then behaved as if they are welded together at the interface, i.e. $[u_n] = 0$ and $[u_s] = 0$. For $1 \ll \omega \ll \mathcal{M}^{-1}$ where the mechanical loss $\mathcal{L}$ decreases slowly with frequency ω, the sample rigidity $|G|$ increases slowly with frequency.

Figure 5.4 shows that the slowly–varying region in the mechanical loss spectrum also depends on corner orientation, whereas the general features described in Figure 5.2 and shown in Figure 5.3 does not depend interface type. Comparing Figure 5.4a and Figure 5.3a, the mechanical loss $\mathcal{L}$ scales differently only in the slowly–varying region. Though corners also subtend an angle equal to 120° in type TS interface having slope angle $\varphi = 60°$, the mechanical loss $\mathcal{L}$ scales differently because the normal stress distribution (see Figure 5.6) is an even function with respect to the corner (instead of an odd function as in type S interface with $\varphi = 30°$). For a type TS interface with $\varphi = 60°$, the mechanical loss $\mathcal{L} \sim \omega^{-0.37}$ and the corresponding stress exponent λ obtained from (5.9) is found to be 0.45. That value is equal to the prediction of $\lambda = 0.45$ given in Figure 5 of Picu & Gupta [33] for a symmetric stress field of σ_{nn}.

So as to concentrate on the essential features in the loss spectrum not affected by slip–viscosity η, we now set the interface to be inviscid i.e. $\eta = 0$ or $\mathcal{M} = 0$ and show that the slowly–varying region is sensitive to slope angle φ.
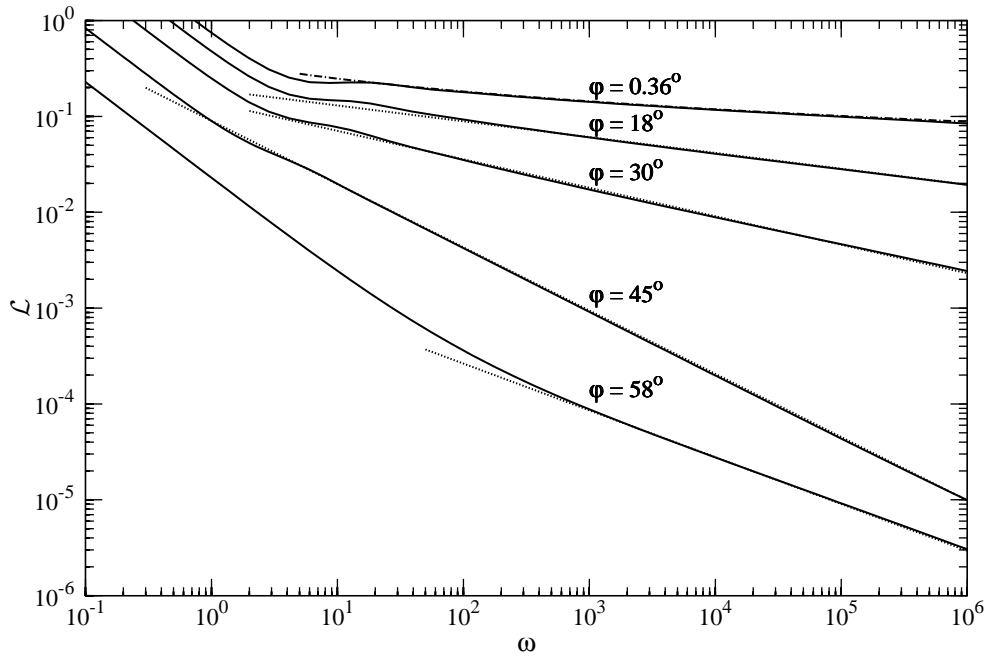
Figure 5.5: Mechanical loss $\mathcal{L}$ as a function of angular frequency ω when the interface is inviscid i.e. $\eta = 0$ or $\mathcal{M} = 0$. Type S interface. $N = 500$. ·········· asymptotes Eq. (5.9) with λ given in Table 1. –··–··– Eq. (39b) of Morris & Jackson [26]. Refer to Figure 5.3 for other parameters.

5.2.1 Sensitivity of slowly–varying region to φ

Figure 5.5 shows the mechanical loss $\mathcal{L}$ as a function of the angular frequency ω with slope angle φ as a parameter for a type S interface. The figure confirms the scaling argument stated above and shows that the mechanical loss scaling in the slowly–varying region depends on the interface corner angle. For a small–slope interface (i.e. $\varphi = 0.36°$), the figure shows that the mechanical loss $\mathcal{L}$ varies as $1/\ln \omega$ in the slowly–varying region That result is consistent with the prediction given in Morris & Jackson [26]. For a finite–slope interface however, the mechanical loss $\mathcal{L}$ varies as ω^α in the slowly–varying region. In Table 5.1, we give the values of α for the finite–slope interfaces found in Figure 5.5. The stress exponents λ are calculated using (5.9). Because the normal stress distribution for a type S interface is an odd function with respect to the corner, these stress exponents λ are compared to the eigenvalues λ_{PG} associated with an anti–symmetric eigenfunction in the local analysis by Picu & Gupta [33] given in their Fig. 5. Due to a lack of parity in the normal stress distribution for a type TS interface (see Figure 5.6b), we did not use that

φ	α	λ	λ_{PG}
18°	-0.17	0.75	0.77
30°	-0.3	0.55	0.58
45°	-0.66	0	0.26
58°	-0.49	0.26	0.26

Table 5.1: Comparison of stress exponent λ derived from the mechanical loss scaling with that λ_{PG} obtained from Picu & Gupta [33]. See text for explanation.

interface for comparison here. From the table, we find that the computed stress exponents λ are close to those obtained from the Picu & Gupta local analysis, except when $\varphi = 45°$. For that specific case, λ vanishes and the mechanical loss scales as $\mathcal{L} \sim \omega^{-2/3}$ as explained below (5.9).

Figure 5.6 shows the interfacial normal stress σ_{nn} distribution near a corner for the interfaces described in the caption. Because the inner solution of the normal stress must match the outer Picu & Gupta solution given by (5.7) at $r = \ell_d \sim \omega^{-1/3}$, the inner solution of $\sigma_{nn} \sim \ell_d^{-\lambda}$. Consequently, graphing the normal stress distribution using variables $\sigma_{nn}\omega^{-\lambda/3}$ and $r\omega^{1/3}$ for different frequencies should define a single curve near corner. This self–similar behaviour of σ_{nn} is evident in the figure. For a type S interface, the local behaviour of the stress is anti–symmetric with respect to the corner. By comparison, the local stress behaviour of a type TS interface does not display a strong parity.

5.2.2 Implication of the scaling analysis

Because the total dissipation Υ along an interface can be found by summing up the contribution from each region surrounding a corner, our scaling analysis suggests that the mechanical loss behaviour in polycrystals at high frequencies i.e. $\omega \to \infty$ will be controlled by the corner having the largest stress exponent λ.

To test this prediction, we consider a type TS interface that is illustrated in Figure 5.7 by the solid line. Dotted line in that figure shows the original type TS interface when $\phi_1 = \phi_2$. Along the interface, there are two different corners C_1 and C_2 that have angles $\phi_1 = 175°$ and $\phi_2 = 107°$, respectively. For these two corners C_1 and C_2, the local analysis by Picu & Gupta (1996) predicts the stress exponent λ to be about 1 and 0.5, respectively. The behaviour of the mechanical loss $\mathcal{L}$ at high frequencies is therefore expected to be controlled by C_1.
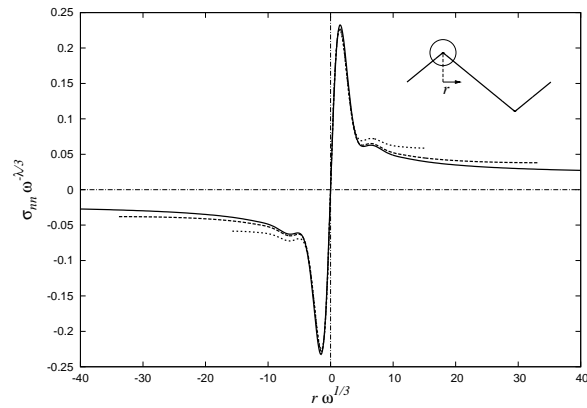
(a) Type *S* interface ($\varphi = 30°$)
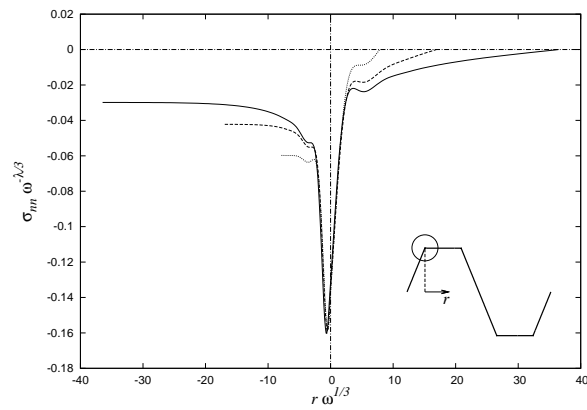
(b) Type *TS* interface ($\varphi = 60°$)
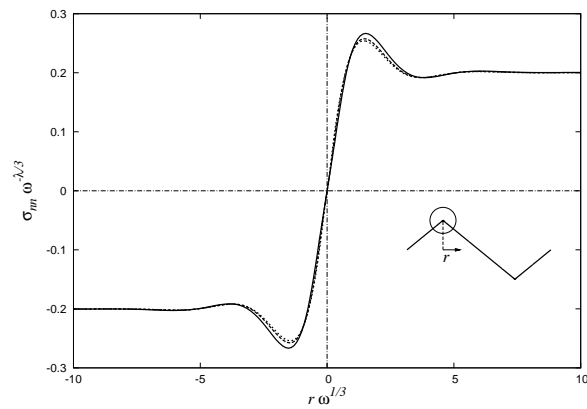
(c) Type *S* interface ($\varphi = 45°$)

Figure 5.6: Normal stress σ_{nn} distribution near corner. Inset shows geometry. ——— $\omega = 10^5$. ----- $\omega = 10^4$. ·········· $\omega = 10^3$. (a) Type *S* interface. $\varphi = 30°$. $\lambda = 0.55$. (b) Type *TS* interface. $\varphi = 60°$. $\lambda = 0.45$. (c) Type *S* interface. $\varphi = 45°$. $\lambda = 0$. Refer to Figure 5.3 for other parameters.
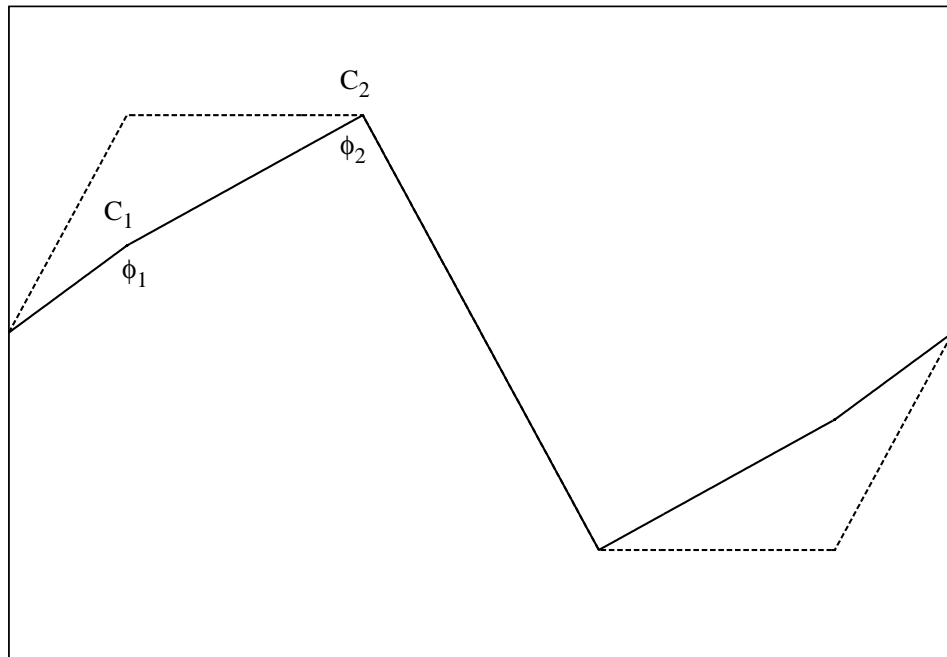
Figure 5.7: Type *TS* interface having two different corner angles. C_1 and C_2 refer to corners. ----- Original *TS* interface with $\phi_1 = \phi_2$.

Figure 5.8 shows the mechanical loss spectrum obtained for the interface given in Figure 5.7 with different corner angles. There are two main features in the figure. First, the behaviour of the mechanical loss is consistent with the above prediction and appears to approach a logarithmic scaling i.e. $1/\ln \omega$ that correspond to a stress exponent $\lambda = 1$ at C_1. The graph is truncated at $\omega = 5 \times 10^8$ due to a lack of numerical resolution at higher frequencies. Second, the slope decreases gradually with frequency in the slowly–varying region due to the diminishing effects from the other corner C_2. To show that the effect of C_2 indeed diminishes with increasing frequency ω , we also graph the scaling $\mathcal{L} \sim \omega^{-0.33}$ produced by C_2.

5.3   Comparison with experiments

Our result thus suggests that the mild frequency–dependent behaviour of the mechanical loss $\mathcal{L}$ that is observed in the experiments is likely to be caused by local stress concentrations near triple junctions. Because corner stress concentration does not depend
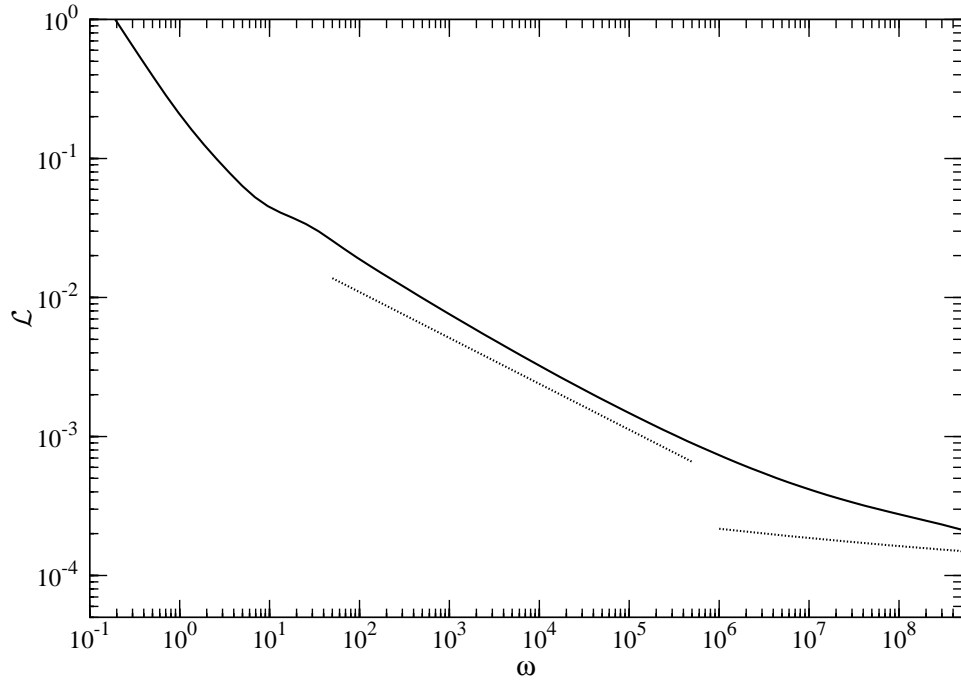
Figure 5.8: Mechanical loss $\mathcal{L}$ as a function of angular frequency ω for the geometry given in Figure 5.7. $\phi_1 = 175°$, $\phi_2 = 107°$. Dotted lines: $\mathcal{L} \sim \omega^{-0.33}$ and $\mathcal{L} \sim 1/\ln \omega$. Refer to text for explanation.

on large scale geometries, its effect also should not depend on these details. Hence, we expect the effect of corner stress concentration to persist even in polycrystals. Microstructures from experimental samples also support that argument. From Figure 11 in Faul *et al.* [9], we find that the ratio of grain size to corner radius in a typical triple junction ~ 200 even when melt, which give rise to rounded corners, is present. According to the predicted form of the loss spectrum given in Figure 5.2, the band of frequencies over which the mechanical loss $\mathcal{L}$ decreases mildly with frequencies would then be large (spanning over 7 decades in frequency).

Figure 5.9 shows the comparison of the mechanical loss behaviour from the bicrystal model with that from the experiments. In the figure, the steady–state creep viscosity η_{ss} of the bicrystal model is calculated from the low frequency behaviour of the rigidity $G(\omega)$; a Fourier transform is applied to $G(\omega)$ to obtain the corresponding time–response when a constant stress is applied to the sample.

From the figure, we find that the mild–frequency dependent behaviour occurs
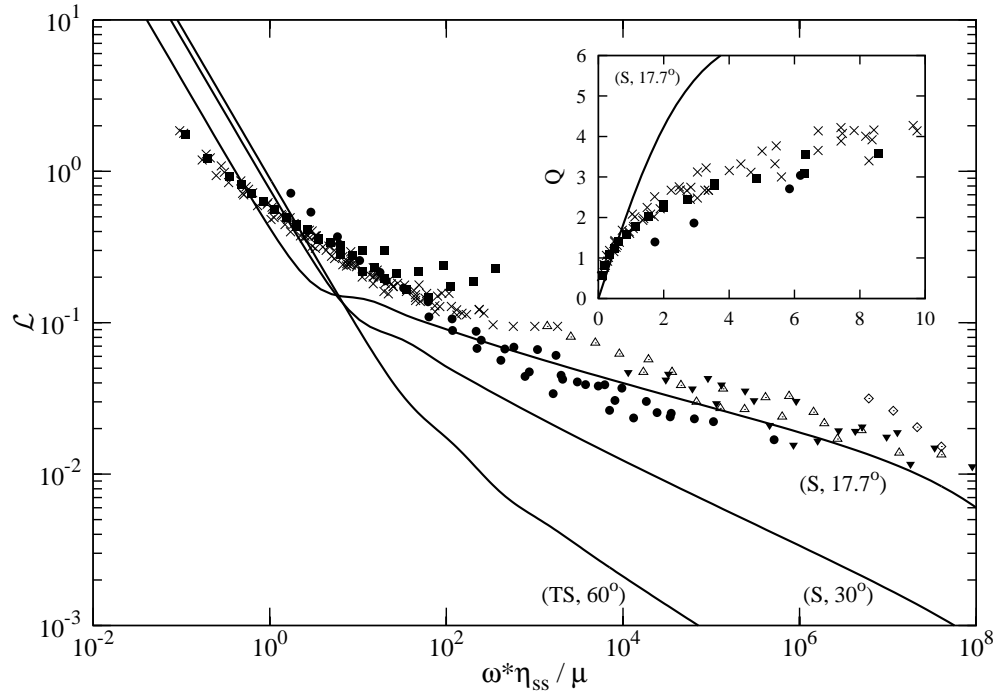
Figure 5.9: Mechanical loss $\mathcal{L}$ as a function of $\omega^*\eta_{\text{ss}}/\mu$. Data points: experiments. Refer to Figure 2.4 for explanation of symbols. Solid lines: bicrystal model (interface, φ). Inset: Quality factor $Q = \mathcal{L}^{-1}$ as a function $\omega^*\eta_{\text{ss}}/\mu$ at low frequency.

over a large band of frequencies in the experiments and the mechanical loss scaling is close to that predicted by the two interfaces found in an array of hexagonal grains i.e. type *S* and *TS* interface with $\varphi = 30°$ and $\varphi = 60°$, respectively. However, these interfaces under predict the mechanical loss $\mathcal{L}$ found in the experiments by roughly an order of magnitude (for a type *S* interface). Because each of these two interfaces only account for part of the loss found in a regular array of hexagonal grains, a larger mechanical loss is expected when concurrent sliding along multiple interfaces of that array is allowed. Numerical models of polycrystal are therefore necessary in order to predict the magnitude of the mechanical loss $\mathcal{L}$ found in the experiments.

Transition between the low–frequency behaviour and the high–frequency behaviour of the mechanical loss $\mathcal{L}$ in the experiments is also not well predicted by the bicrystal model. Closer examination of the experiments however show the ANU data appears to approach gradually towards the low–frequency behaviour of the two interface, whereas the other data appears to approach that behaviour at a lower frequency. That

transition is gradual as opposed to that from the bicrystal model because the transition frequency depends on interface slope φ and the diffusive timescale t_D that are expected to be widely distributed in a polycrystal.

In the figure, the mechanical loss becomes less sensitive to frequency ω with increasing frequencies in the experiments. This result is consistent with our prediction that a gradual decrease in the slope of the mechanical loss spectrum is an outcome when the angles differ from corner to corner along a sliding surface. Given that corner angle in triple junctions vary spatially along any sliding surfaces in a polycrystal, that behaviour is also expected to be found in polycrystal.

An effective slope angle φ_{eff} that matches the data from the experiments may also be derived using a type S interface. Though some discrepancies are found at lower frequencies, an effective slope angle $\varphi_{\text{eff}} = 17.7°$ is found to match the experimental results closely at high frequencies, as shown in the figure. The behaviour of the quality factor $Q = \mathcal{L}^{-1}$ at low frequency is shown in the inset using linear scale. At low frequency, the quality factor Q approaches linearly to zero in the bicrystal model with an effective slope angle $\varphi = 17.7°$ whereas the experimental data, specifically from Bunton [5] and Sundberg & Cooper [40], approach the origin at a faster rate.

5.4 Summary

In summary, the general features found in the mechanical loss spectrum for a bicrystal model of diffusionally–accommodated grain boundary sliding at finite slope is consistent with the prediction by the small–slope analysis [26]. When the timescales are widely separated i.e. when $\mathcal{M} \ll 1$, the two key features found in the spectrum for a finite–slope interface are:

1. A slow–varying region of the mechanical loss $\mathcal{L}$ at frequencies $1 \ll \omega \ll \mathcal{M}^{-1}$ for interface having sharp corners. In that region, the mechanical loss has a power–law dependence on frequency i.e. $\mathcal{L} \sim \omega^{\alpha}$, where the power–law exponent α depends on the corner stress concentration. Owing to the constraint of the stress exponent λ, the power–law exponent is bounded by $-2/3 \leq \alpha < 0$. When corner angle varies along the interface, the slope of the mechanical loss decreases with increasing frequency, and is ultimately controlled by the corner having the most singular stress behaviour.

2. A local maximum near frequency $\omega \sim \mathcal{M}^{-1}$. That peak stands out from the high–temperature or absorption background caused by diffusion.

To assess the sensitivity of the mechanical loss peak to factors that were proposed to explain for the broader and weaker peak found in the experiments (described in §2.2.1), we now isolate the peak from the absorption background and consider the case of elastically–accommodated grain boundary sliding using the bicrystal model.

Chapter 6

Elastically–accommodated grain boundary sliding

Here, we use the bicrystal model to study the mechanical loss peak caused by elastically–accommodated grain boundary sliding. Specifically, we isolate the loss peak from the high–temperature background by suppressing diffusion along the grain boundary. The resultant b.v.p. is posed below (3.10).

In §6.1, we derive analytical constraints of our numerical solution for that b.v.p. These constraints are, namely, (i) a new elementary solution of the bicrystal model for a type S interface with slope angle $\varphi = 45°$, (ii) the high and low frequency asymptotes in the mechanical loss spectrum, (iii) the local solution from Picu & Gupta [33] and (iv) the perturbation solution obtained for a small slope interface from Morris & Jackson [26]. The high and low frequency asymptotes are used to obtain master variables for the mechanical loss spectrum.

In §6.2, we discuss the numerical results. We show that our numerical solution satisfy all the constraints stated above. We then extend our analysis to study the effects of non–uniform grain size and non–uniform viscosity in §6.3. Using these results, we evaluate three proposed suggestions used to explain the small and broad peak commonly found in the experiments. These proposed suggestions are described in §2.1.4 and are restated here:

- variation in grain size by Pezzoti [31],

- variation in boundary viscosity η by Cooper [8],

- sharp corners at triple junctions by Faul *et al.* [9].

Our result suggests that of the three proposed explanations, only a large variation in boundary viscosity η along grain boundaries is able to broaden the loss peak significantly. Concurrent with that effect, all the proposed explanations are also found to be able to reduce the loss peak moderately, but is unlikely to completely suppress its presence in the mechanical loss spectrum when the timescales are widely separated.

6.1 Analytical constraints on the numerical solution

6.1.1 A simple shear solution

For all interface shapes, the simple shear field given by

$$u = \frac{y}{a}e^{i\omega t}\hat{x} \tag{6.1}$$

satisfies all governing equations except the slip condition (3.10b). For an arbitrary interface shape, (6.1) does not satisfy that condition because the left hand side (l.h.s.) vanishes, but the right hand side (r.h.s.) is non–zero in general. However, for a type S interface with $\varphi = \pm 45°$, the interface coincides with the principal axes of stress calculated from (6.1). Consequently for that special case, the shear stress on the interface vanishes. Eq. (6.1) then satisfies the b.v.p. of elastically–accommodated grain boundary sliding described below (3.10) exactly. The two grains are thus effectively welded together and for all ω, $G = 1$ for a type S interface with $\varphi = 45°$. In particular, the mechanical loss vanishes identically for this case.

6.1.2 Asymptotes for high frequency and for low frequency

Because mechanical energy is only dissipated by viscous shearing along the interface $\mathcal{S}_I$, the dissipation rate is controlled by the shear stress σ_{ns}. As a result, the dissipation rate in (5.1c) becomes

$$\dot{\Upsilon} = \int_{\mathcal{S}_I} \sigma_{ns}^2 \, ds \,. \tag{6.2}$$

We note that $\dot{\Upsilon}$ here is non–dimensionalized using the sliding timescale t_η.

High–frequency limit

In the limit as $\omega \to \infty$, (3.10b) requires $[u_s] \to 0$. Together with the boundary condition (3.10a), that limiting case is equivalent to the condition stated in §5.1.2. Correspondingly, the mechanical loss at high frequencies varies inversely with frequency according to (5.5). Setting $\mathcal{M} = 1$ to rescale the frequency according to the sliding timescale t_η, Eq. (5.5) becomes

$$\mathcal{L} \sim \frac{1}{2a\omega} g(\varphi). \tag{6.3}$$

The geometric factor $g(\varphi)$ in (6.3) is given for both type S and type TS interfaces in Eq. (5.6).

Low–frequency limit

In the limit as $\omega \to 0$, (3.10b) simplifies to $\sigma_{ns} = 0$. Consequently, the sample behaviour again becomes perfectly elastic. The energy balance (5.1a) then simplifies: the l.h.s. balances the second term on the r.h.s.; power supplied at the sample boundary now balances the rate of increase of stored strain energy. Integrating that simplified balance in time, we find that at zero frequency, the rigidity and strain energy are related by

$$G_0 = \frac{1}{2\pi} W_0 \, a. \tag{6.4}$$

Here, W_0 is calculated from (5.1b) using the solution of the b.v.p stated below (3.10) for $\omega = 0$ and $u = \pm 1$ at $y = \pm a$. We have used the relation $\tau \sim G_0 U/a$ where $G_0 = \lim_{\omega \to 0} G(\omega)$.

Next, using successive approximations, and assuming that the displacement vector varies sinusoidally in time so that $u(x, y, t) = \hat{u}(x, y) \sin \omega t$, we find that the first correction to the shear stress at the interface is given by $\sigma_{ns} = \omega [\hat{u}_s] \cos \omega t$. Here $[\hat{u}_s]$ is calculated from the solution of the b.v.p. posed immediately below (6.4). Using the expression given in (6.2) for the dissipation rate $\dot{\Upsilon}$, we find that $\dot{\Upsilon} = \omega^2 \cos^2 \omega t \int [\hat{u}_s]^2 \, ds$. Integrating that relation over one period, we find that

$$\Upsilon \sim \pi \omega \Phi_0 ; \tag{6.5a}$$

$$\Phi_0 = \int_{\mathcal{S}_I} [\hat{u}_s]^2 \, ds \tag{6.5b}$$

is the mean square slip at $\omega = 0$. Similarly, the mean strain energy is given by $\bar{W} = \frac{1}{2} W_0$, where W_0 is obtained by using u to evaluate (5.1b). Using the interpretation of $\mathcal{L}$ given

below (3.13), we obtain

$$\mathcal{L} \sim \frac{\Phi_0}{2W_0}\omega. \tag{6.6}$$

Although Φ_0 and W_0 need to be computed numerically to obtain the low frequency asymptote, this result, nevertheless, enables us to verify that our numerical solution is self-consistent.

6.1.3 Master variables for the mechanical loss curve

Using the above asymptotes, we introduce master variables allowing numerical results for different interface geometries to be represented on a single curve. According to (6.3) and (6.6), in the extremes of high and of low frequency, the mechanical loss depends on interface geometry solely through the parameters Φ_0/W_0 and $g(\varphi)/a$. Defining new variables ω', $\mathcal{L}'$ by

$$\omega' = \frac{\omega}{\omega_m}, \qquad\qquad \mathcal{L}' = \frac{\mathcal{L}}{\mathcal{L}_m}, \tag{6.7a,b}$$

then choosing the scales ω_m and $\mathcal{L}_m$ so that the asymptotes (6.3) and (6.6) become respectively $\mathcal{L}' \sim 1/\omega'$ and $\mathcal{L}' \sim \omega'$, we find that

$$\omega_m = \sqrt{\frac{W_0 g(\varphi)}{a\Phi_0}}, \tag{6.8a}$$

$$\mathcal{L}_m = \frac{1}{2}\sqrt{\frac{\Phi_0 g(\varphi)}{aW_0}}. \tag{6.8b}$$

Provided no additional processes enter at intermediate frequencies, values of $\mathcal{L}$ computed for different interface geometries should define a single curve when $\mathcal{L}/\mathcal{L}_m$ is graphed against ω/ω_m. This prediction is tested in §6.2.

We may note that the master variables are particularly useful because as N is increased above about 10, the interface length rapidly approaches that of the limiting forms given in Eq. (3.15), so the geometric factor $g(\varphi)$ can be calculated using the results for a piecewise linear interface. By contrast, both W_0 and Φ_0 prove to converge slowly as N is increased, making it useful to be able to present results for differing N in terms of a single curve.

6.1.4 Local solution of Picu & Gupta

For interfaces having sharp corners, the stress obtained by solving the b.v.p. of elastically–accommodated grain boundary sliding proves to be singular at corners. The asymptotic behaviour near the corner must be compatible with a local analysis given by Picu & Gupta [33]. Specifically, because the displacements are finite, boundary condition (3.10b) requires the shear stress on the interface to remain finite as the distance r from the corner vanishes. Within the grains however, the stress becomes infinite as $r \to 0$. Compared with that infinity, the interfacial stress appears to vanish, and so, the effective interfacial boundary condition is $\sigma_{ns} = 0$ on the interface near a corner. The local problem applying near the corner is defined by the b.v.p. of elastically–accommodated grain boundary sliding but with (3.10b) replaced by the simplified condition $\sigma_{ns} = 0$. As described above (5.7), that local problem admits a separable solution in which the stress $\sigma \propto r^{-\lambda}$, where r is defined in Figure 5.1 and λ satisfying the constraints given below (5.7). The Picu-Gupta solution shows that, owing to the condition of finite strain energy, the displacement must be continuous at the corner, i.e. as the corner O is approached along any path, the difference $|u - u_O| \to 0$. In his numerical solution for a hexagonal array, Ghahremani [12] imposed, without discussion, the equivalent condition of vanishing relative displacement of the grains at corners. In §6.2, we demonstrate that our numerical solution of the b.v.p. for elastically–accommodated grain boundary sliding is consistent with that local analysis.

6.1.5 Perturbation solution for small–slope interface

The numerical solution also has to satisfy the small–slope perturbation solution from Morris & Jackson [26]. To obtain the small–slope solution of elastically–accommodated grain boundary sliding, we use Eqs. (14), (17), (31) and (32) from Morris & Jackson. We replace $\omega \mathcal{M}$ by ω and then set $\mathcal{M} = 0$ in these equations. Letting

$$b_1 = \frac{1}{2(1 - \nu)} \sum_{n=1}^{\infty} n^3 f_n^2, \tag{6.9a}$$

$$b_2 = \tfrac{7}{2} \sum_{n=1}^{\infty} n^2 f_n^2, \tag{6.9b}$$

we find that the boundary shear stress τ is then given by $\tau = \tau^{(0)} + \varepsilon^2 \tau^{(2)} + O(\varepsilon^4)$;

$$\tau^{(0)} = \frac{2i\omega}{1 + 2ia\omega} U; \tag{6.10a}$$

$$\tau^{(2)} = \frac{b_1 + ib_2\omega}{(1 + 2ai\omega)^2} U.$$
(6.10b)

Equation (6.10a) gives the boundary stress for the flat interface corresponding to $\varepsilon = 0$, and (6.10b) gives the first correction caused by the interface topography that enters the calculation for characteristic slope $\varepsilon \neq 0$.

For time–periodic forcing, the constitutive equation for a standard linear solid in simple shear is

$$\{1 + i\omega A\}\tau - \{C + i\omega B\}U = 0.$$
(6.11)

In our case, the material constants A, B, C for the sample are functions of interface slope to be determined.

To prove that the mechanical system shown in Figure 3.1 behaves as a standard linear solid, at least to the order ε^2 to which we have carried the perturbation analysis, we substitute (6.10) into (6.11), then multiply by the denominator of (6.10b). The result is a cubic polynomial in ω. Equating the coefficients of that polynomial to zero, we obtain an over–determined system of 4 linear equations for 3 unknowns A, B and C. Noting that those equations themselves involve an error of order ε^4, we solve them correct to $O(\varepsilon^2)$, and find that

$$A = 2a + \varepsilon^2 a(b_2 - 2ab_1) + O(\varepsilon^4),$$
(6.12a)

$$B = 2 + \varepsilon^2(b_2 - 2ab_1) + O(\varepsilon^4),$$
(6.12b)

$$C = \varepsilon^2 b_1 + O(\varepsilon^4).$$
(6.12c)

(To $O(\varepsilon^2)$, the b.v.p. of elastically–accommodated grain boundary sliding also satisfies the extra equation making the system over–determined.) We conclude that the mechanical system shown in Figure 3.1 behaves as a standard linear solid with an error $O(\varepsilon^4)$. The zero–frequency (relaxed) rigidity G_0, and the relaxation time $t_\gamma = A$ at constant strain are given by

$$G_0 = \varepsilon^2 ab_1,$$
(6.13a)

$$t_\gamma = 2a + \varepsilon^2 a(b_2 - 2ab_1);$$
(6.13b)

$$W_0/\Phi_0 = \frac{1}{4}\varepsilon^2 b_1,$$
(6.13c)

because in the limit as $\varepsilon \to 0$, $[\hat{u}_s] = 2 + O(\varepsilon^2)$ by Morris & Jackson [26] in Eqs. (17b) and (20a).

In the limit as $\varepsilon \to 0$, the geometric factor $g(\varphi) \to 1$, and the scales defined by (6.8a) and (6.8b) become

$$\omega_m = \frac{1}{2}\varepsilon \sqrt{\frac{b_1}{a}} = \sqrt{G_0}/t_\gamma + O(\varepsilon^3) \tag{6.14a}$$

$$\mathcal{L}_m = \frac{1}{\varepsilon \sqrt{ab_1}} = \frac{1}{\sqrt{G_0}} + O(\varepsilon^3) \tag{6.14b}$$

Forming the expression for $\mathcal{L} = \tan \arg G$ from (6.11) and (6.12), rewriting in terms of the master variables ω', $\mathcal{L}'$ defined by (6.7), then taking the limit as $\varepsilon \to 0$ (fixed ω'), we find that

$$\mathcal{L}' = \frac{\omega'}{1 + \omega'^2}. \tag{6.15}$$

According to (6.15), in the limit as $\varepsilon \to 0$, the maximum loss of $\frac{1}{2\sqrt{G_0}}$ occurs at angular frequency $\omega = \sqrt{G_0}/t_\gamma$. Because $G_0 \ll 1$, these results are consistent with usual theory for the standard linear solid, in which the maximum loss is given by $(1 - G_0)/2\sqrt{G_0}$.

For comparison with the numerical solution, we use (6.14b) to derive an expression giving $\mathcal{L}_m$ as a function of the number $\bar{N}$ of terms included in the Fourier series representation of the interface given in Eq. (11) of Morris & Jackson [26]. We note that $\bar{N}$ is approximately equal to the ratio N of corner radius to wavelength as defined in (3.14). For type S and type TS interfaces, b_1 is given by the expression

$$(1 - \nu)b_1 = \frac{32\beta}{\pi^4} \sum_{n=1,3,5,\ldots}^{\bar{N}} n^{-1}$$

$$= \frac{16\beta}{\pi^4}\left\{ \ln(2\bar{N} + 2) + \gamma_E \right\} + O(\bar{N}^{-2}). \tag{6.16}$$

(A standard sum has been used.) The Euler constant $\gamma_E = 0.577\ldots$, and the numerical factor β takes the value 1 or 2 according as the interface is type S or TS respectively. According to (6.13a), (6.14b) and (6.16), the zero–frequency rigidity increases logarithmically with $\bar{N}$ for small slopes. That result holds for large fixed $\bar{N}$ in the limit as $\varepsilon \to 0$; and is consistent with the local analysis of Picu & Gupta [33]. That analysis shows that in the limit as the angle subtended by a corner approaches π, the stress in the elastic solution varies locally as r^{-1}, so that the strain energy diverges logarithmically.

6.2 Discussion of numerical results

Figure 6.1a shows the computed values of $\mathcal{L}$ graphed using the master variables defined by (6.7). Results are shown for slope angles including those appropriate for a regular hexagonal array. The solid curve shows the prediction of the small slope analysis, as given by (6.15). A similar master plot is also possible for $|G|$. Because Fig. 6 of Ghahremani [12] shows that an array of regular hexagons behaves as a standard solid, we assume and then verify that the same is true of the Raj–Ashby bicrystal system. For a standard solid, however, $(1 - |G|^2)/(1 - G_0^2)$ depends only on $\omega \sqrt{G_0}/\omega_{\mathrm{m}}$, where G_0 is the rigidity at zero frequency, and we have identified the time scale for the loss curve with ω_{m}^{-1}. Substituting for G_0 and ω_{m} from (6.4) and (6.8) respectively, we find that if the sample behaves as a standard solid, values of $|G|$ computed for different N and φ will define a curve when $(1 - |G|^2)/(1 - G_0^2)$ is graphed against $\omega a \sqrt{\Phi_0/2\pi g(\varphi)}$. Figure 6.1b confirms that prediction. The bicrystal system therefore behaves as a standard solid. This result also justifies our having used the physical interpretation of $\mathcal{L}$ given below (3.13) to define the asymptotes given in §6.1.2.

We note that although Ghahremani [12] also concludes that elastically accommodated grain boundary sliding can be fitted to the constitutive equation for a standard solid, our procedure above differs from his. Whereas Ghahremani fitted numerical results for a single geometry (hexagonal array) to the response curve for a standard solid, we instead have used Figure 6.1 to show that the results for many different geometries (i.e. values of φ and N) obey the same similarity principle as the standard solid. Moreover, the response curves shown in Figure 6.1 are not fitted curves. As described in §6.1.5, they are, in fact, calculated analytically as part of the small–slope analysis, and proved to be identical with the corresponding response curves for a standard solid.

Owing to the self–similarity demonstrated in Figure 6.1, at arbitrary frequency, the values of N and φ affect G purely through their influence on the elastic solution for $\omega = 0$. In particular, the mechanical loss $\mathcal{L}$ is controlled by the quantity W_0/Φ_0.

Figure 6.2 shows W_0/Φ_0 as a function of φ with N as a parameter. For the N–values included there, the numerical solution approaches the perturbation solution when $\varphi < 10°$. In Figure 6.2a, the vertical line corresponds to the simple shear solution described in in §6.1.1; for that solution $\Phi_0 = 0$, so that W_0/Φ_0 is infinite. The dotted curve shows
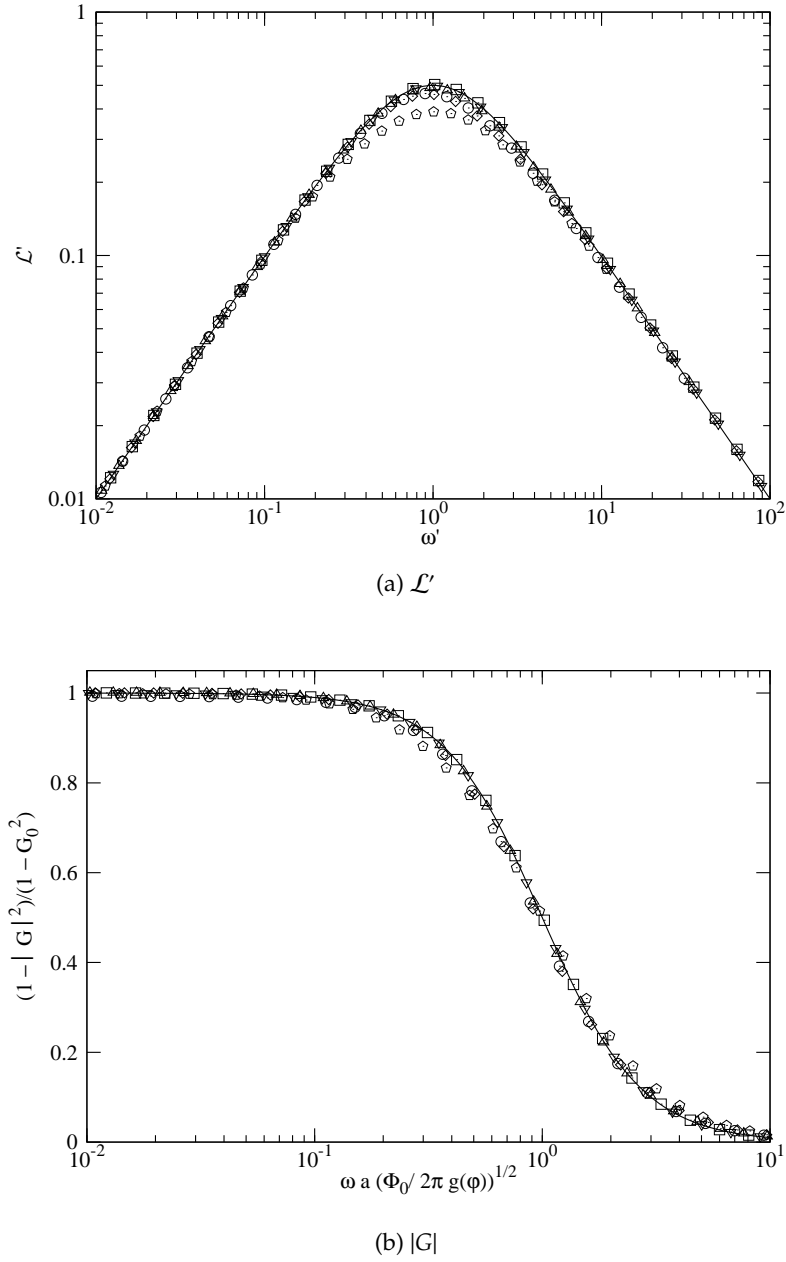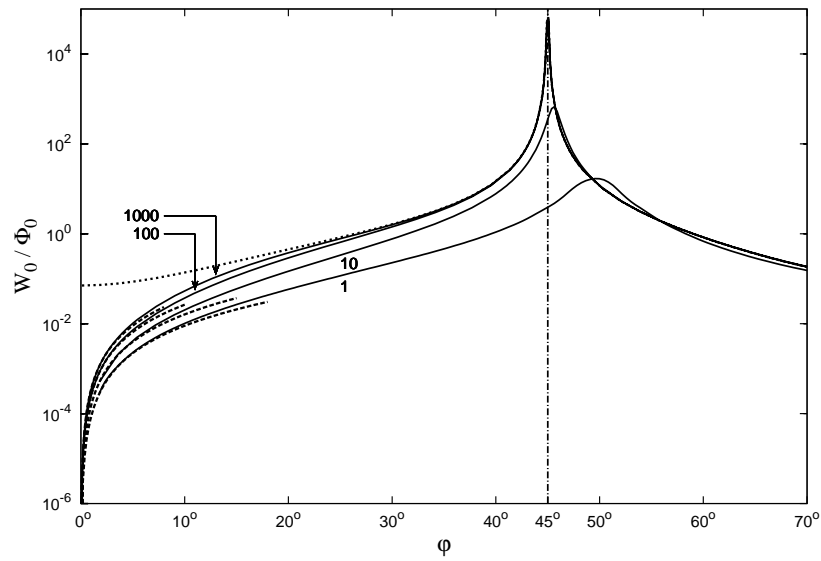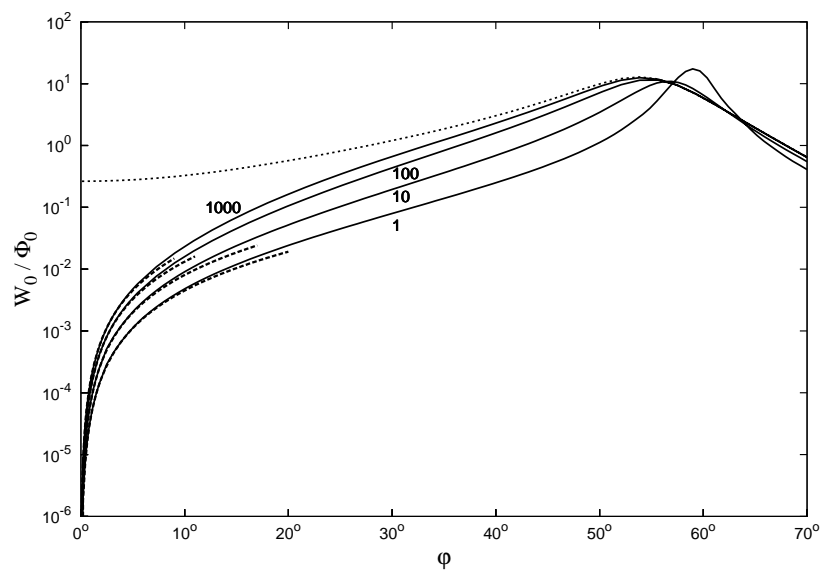
(a) $\mathcal{L}'$

(b) $|G|$

Figure 6.1: (a) $\mathcal{L}'$ as a function of ω'. (b) $(1 - |G|^2)/(1 - G_0^2)$ as a function of $\omega a \sqrt{\Phi_0/2\pi g(\varphi)}$
. $\mathcal{L}'$ and ω' are defined in (6.7); $g(\varphi)$ is defined in (5.6); W_0, Φ_0 and G_0 are computed numerically. Numerical solution of $(N, \varphi, \text{interface})$ are $(10, 17.6°, S)$ □, $(100, 51.8°, S)$ ○, $(1000, 30°, S)$ △, $(10, 17.6°, TS)$ ▽, $(100, 32.4°, TS)$ ◇, $(1000, 60°, TS)$ ⬠. Solid curves indicate perturbation solution. Other parameters: $a = 5$, $\nu = 0.3$.

(a) Type *S*

(b) Type *TS*

Figure 6.2: W_0/Φ_0 as a function of φ with N as a parameter. Curve labels give value of N. Dotted line, pinned corners solution. Dashed line, perturbation solution (6.13c). For values of a and ν, see caption in Figure 6.1.

Interface	φ	N	$\max_\omega \mathcal{L}$
S	30°	10	0.068
		∞	0.047
TS	60°	∞	0.040

Table 6.1: Maximum mechanical loss $\mathcal{L}$ for Raj and Ashby's two sliding modes

the solution obtained for a piecewise linear interface, but using the Ghahremani (pinned corner) boundary condition, namely that $[u] = 0$ at a vertex. That solution, computed for a large value of N, is independent of the parameter N itself. Apart from the curve for $N = 1$, the behaviour is independent of N for sufficiently large φ; and as N is increased (so that the corners are made tighter), the dependence on N is confined to a range of φ of decreasing size. We infer that in the limit as $N \to \infty$ (fixed $\varphi \neq 0$), W_0/Φ_0 approaches the solution obtained when the corners are pinned.

The existence of that limiting state strongly constrains the effect of rounding corners on the loss and frequency scales defined by (6.8). For a type S sliding surface in a regular hexagonal array, the slope angle $\varphi = 30°$ and, according to Figure 6.2a, increasing N from 1 to ∞ causes W_0/Φ_0 to vary about tenfold. The corresponding variation in the frequency and loss scales is only about a factor of three. The effect is even weaker for the TS surface. For it, $\varphi = 60°$ and, according to Figure 6.2b, W_0/Φ_0 is then essentially independent of N.

To emphasize this conclusion, in Table 6.1 we give a numerical example. Comparing lines 1 and 2 in the table, we see that for the type S interface with $\varphi = 30°$, increasing N from 10 to ∞ causes the maximum value of $\mathcal{L}$ to decrease by only about 30%; according to Figure 6.2a, the limiting case shown in line 2 is attained for $N \geq 100$. In line 3, we show only the limiting case, as explained at the end of the previous paragraph. These values are equal to the magnitude of the peaks found in Figure 5.3a and Figure 5.4a for diffusionally–accommodated grain boundary sliding. We note that these values of maximum loss are roughly half the corresponding value reported by Ghahremani [12] for elastically accommodated sliding in an array of regular hexagons. In that array, sliding occurs simultaneously on 2 orthogonal surfaces, and a larger loss is to be expected.

The function W_0/Φ_0 is, in the limit as $N \to \infty$, clearly discontinuous at $\varphi = 0$. In that case, the interface is plane and the displacement imposed on the sample is completely

accounted for at zero frequency by slip; consequently $W_0 = 0$. By contrast, Figure 6.2 shows that for pinned corners, $W_0/\Phi_0 \neq 0$. Because the response is discontinuous in the limit, W_0/Φ_0 always depends on N within a sufficiently small neighbourhood of the origin, as demonstrated by (6.13c) and (6.16) of the perturbation analysis for $\varphi \to 0$. The convergence of the solution as $N \to \infty$ is thus non–uniform in φ, i.e. the solution has an inner–and–outer structure with respect to φ.

Figure 6.3 shows the zero frequency rigidity $G_0 = W_0 a/2\pi$ as a function of φ. We note that $G_0 \leq 1$, in agreement with the physical constraint that the sample can not have a rigidity exceeding that of the individual grains. Further, G_0 is a non–monotonic function of φ. For the type S interface, that non–monotonicity is a consequence of the simple shear solution for $\varphi = 45°$, as discussed in §6.1.1. Figure 6.3b shows that even for the type TS interface, G_0 has a maximum at around $50°$.

Figure 6.4 shows the distribution of slip $[u_s]$ along the interface for the parameter values given in the caption. The slip decreases monotonically as N increases and the corners become sharper. That is consistent with the requirement that the total strain energy of the sample is finite. That condition requires that the stress tensor varies with distance r from a sharp corner in such a way that $r\sigma_{ij} \to 0$ as $r \to 0$, and the local solution of Picu & Gupta [33] then requires the slip to vanish at the corner. This result is evident from the figure. By increasing N, the slip distribution approaches the limiting case when the corners are numerically pinned, as assumed by Ghahremani [12]. We also note that the weak dependence of slip $[u_s]$ on N is consistent with the result shown in Figure 6.2a: that the ratio W_0/Φ_0 becomes almost independent of N when $\varphi = 30°$.

Figure 6.5 shows, as a function of distance r from the origin shown in the inset, the computed shear stress $\sigma_{r\Theta}$ on the interface at $\Theta = 0°$. The origin sets a corner length scale at which the stresses are smoothed out. From the figure, we find that $\sigma_{r\Theta}$ scales with $r^{-0.95}$ when $\varepsilon = 0.001$. This result is close to the $1/r$ scaling predicted by the perturbation solution in Morris & Jackson [26], and explains the logarithmic scaling for G_0 found in that solution. Consistent with the local solution by Picu & Gupta [33], our numerical solution also predicts that the stress singularity weakens as φ increases. When $\varphi = 32.5°$, our eigenvalue $\lambda = 0.53$. That result is close to the solution given in Fig. 5 of Picu & Gupta [33] where we estimate, using our slope angle definition, their eigenvalue $\lambda = 0.55$ at $\varphi = 32.5°$. The weakened singularity with $\lambda < 1$ thus ensures that the strain energy W remains finite.
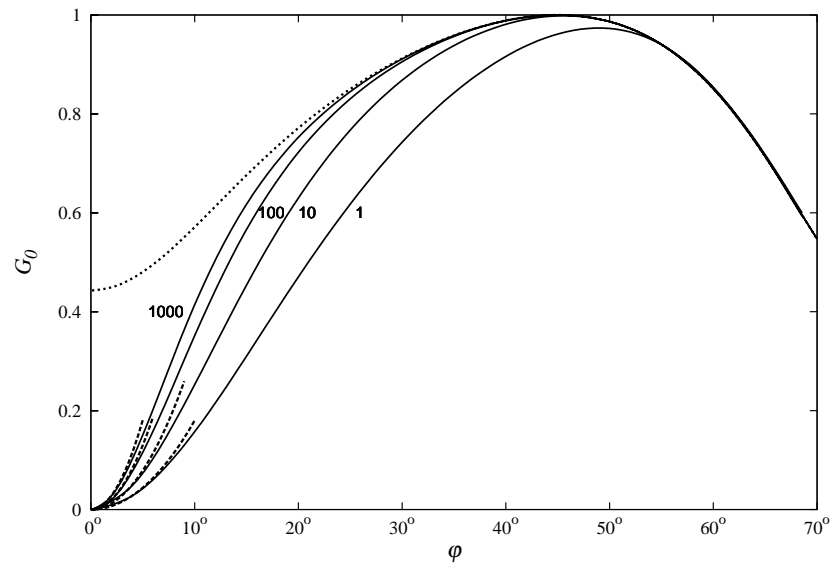
(a) Type *S*
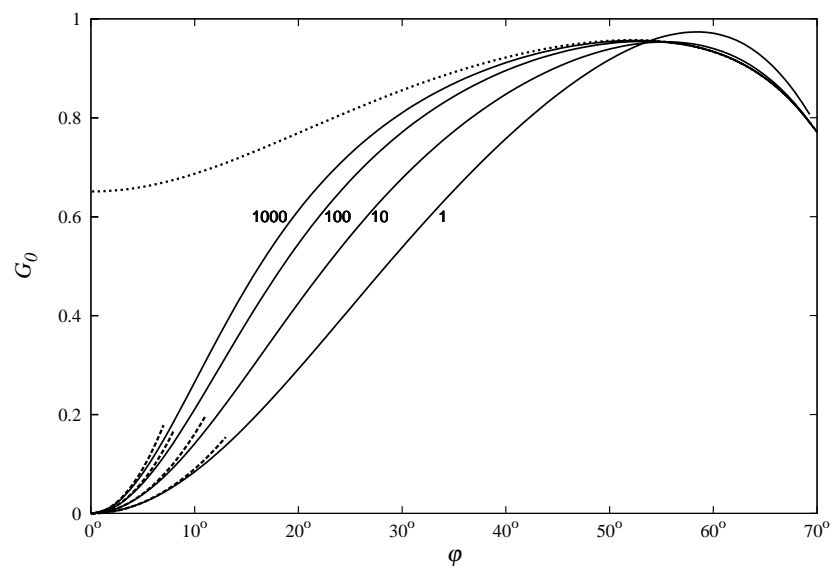
(b) Type *TS*

Figure 6.3: G_0 as function of φ with N as a parameter. Curve labels give value of N. Dotted line, pinned corners solution. Dashed line, perturbation solution (6.13a). For values of a and ν, see caption in Figure 6.1.
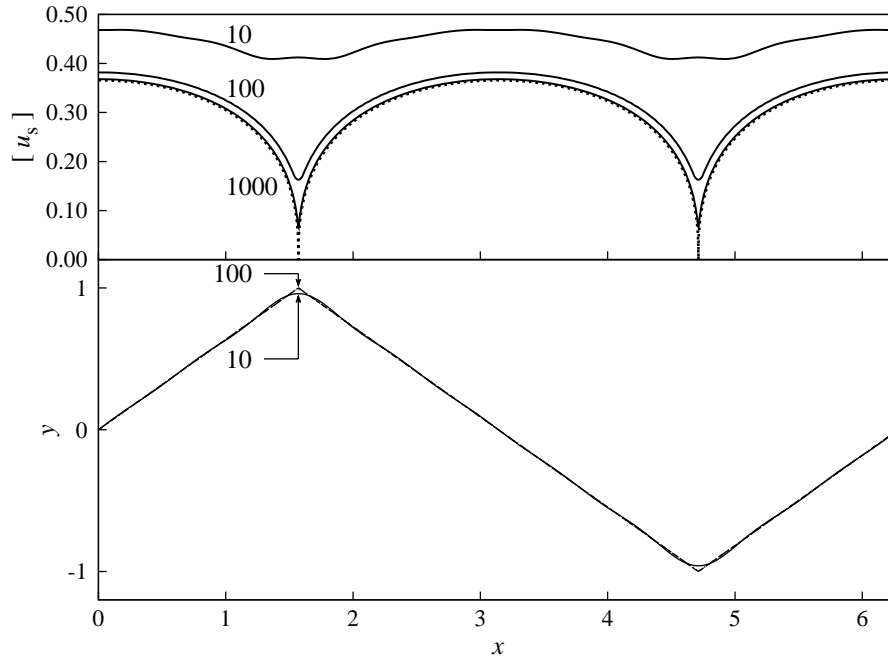
Figure 6.4: Upper part, zero frequency slip $[u_s]$ as a function of position with $\varphi = 30°$. Curve labels give value of N. Dotted line, pinned corners solution. Lower part, type S interfaces using above values of N, curves 100 and 1000 are graphically identical. For values of a and v, see caption in Figure 6.1.

6.3   Effects of non-uniform grain size and viscosity

The idealization of a constant grain size d and a constant boundary viscosity η is usually not found in real polycrystalline solids. Even in experiments on synthetic samples, e.g. in Faul *et al.* [9], grain size can vary by about a factor of 4. The boundary viscosity η may also vary by about an order of magnitude as described in Ashby [2]. This non-uniformity of grain size and viscosity is often invoked to explain the broad absorption peak (instead of a single Debye peak) commonly found in experiment, e.g in Schaller & Lakki [37]. We test these suggestions using the bicrystal model.

Figure 6.6 shows the type S interfaces used to assess these effects. In the left figure, there are two adjacent grains of equal size d with viscosities η_1 and η_2 along their interface. The right figure shows 5 adjacent grains of two different sizes d_1 and d_2. In that figure, the total area occupied by the "small" grains is equal to that of the "big" grain, and the viscosities along their interface are η_2 and η_1, respectively. We note the total interfacial length available for sliding is the same in both configurations. Four systems are considered
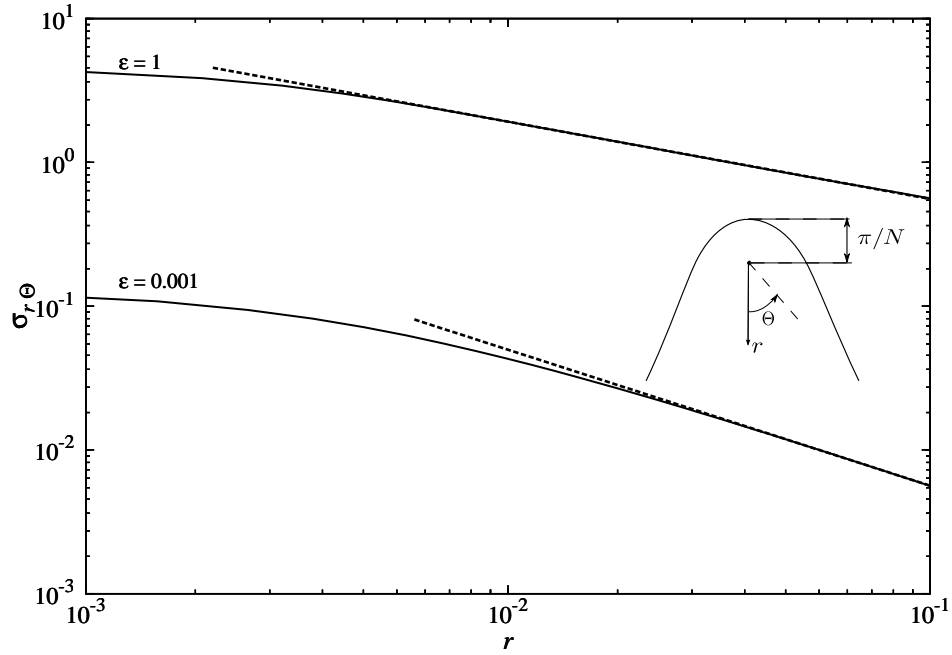
Figure 6.5: $\sigma_{r\Theta}$ at $\Theta = 0°$ as a function of r when $\omega = 0$ and $N = 900$ for $\varepsilon = 0.001$ and $\varepsilon = 1.0$ (i.e $\varphi = 32.5°$) of a type S interface. Dashed lines indicates fitted $r^{-\lambda}$ scaling. Coordinate system is shown in the inset figure. For values of a and v, see caption in Figure 6.1.

here:

1. configuration 1 with $\eta_1 = \eta_2 = \eta$ (Uniform grain size and viscosity);

2. configuration 1 with $\eta_1 = \eta$ and $\eta_2 = 10\eta$ (Non-uniform viscosity);

3. configuration 2 with $d_1 = d$, $d_2 = d_1/4$ and $\eta_1 = \eta_2 = \eta$ (Non-uniform grain size);

4. configuration 2 with $d_1 = d$, $d_2 = d_1/4$, $\eta_1 = 10\eta$ and $\eta_2 = \eta$ (Non-uniform viscosity and grain size).

In Figure 6.7, we graphed the mechanical loss spectra obtained from these systems. There are two main features in the figure. First, the loss peak weakens as well as broadens when boundary viscosity η varies with position, i.e. in systems (ii) and (iv). Second, comparing systems (i) to (iii) and (ii) to (iv), we find that, when grain size varies spatially, the loss peak only weakens without any significant change to its shape.

The two effects (broadening and weakening) are caused by a difference in the sliding frequency t_η^{-1} across adjacent interfaces. Because sliding frequency t_η^{-1} depends

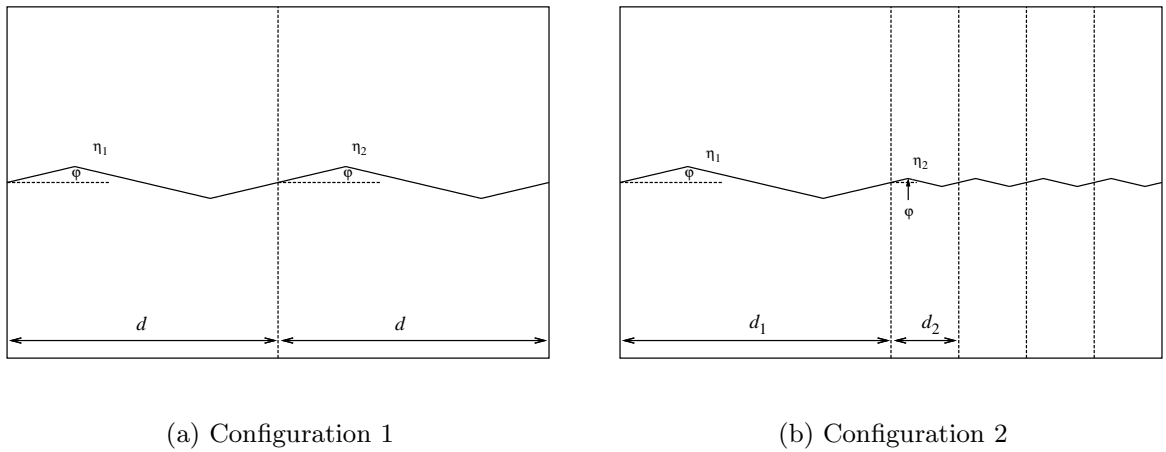(a) Configuration 1   (b) Configuration 2

Figure 6.6: Two configurations having type S interface. (a) uniform grain size: d. (b) non-uniform grain sizes: $d_1 = d$ and $d_2 = d/4$. Adjacent grains are separated by dashed line.
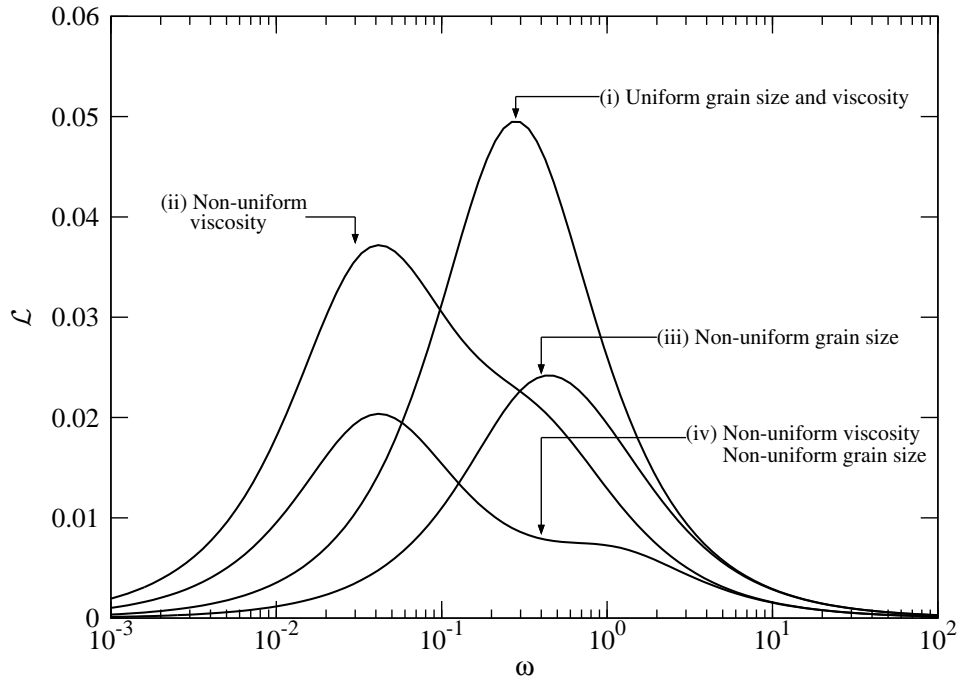

Figure 6.7: $\mathcal{L}$ as a function of ω for the four systems (i)–(iv). Slope angle $\varphi = 30°$.

on grain size and the boundary viscosity as defined in (3.5a), sliding in systems (ii) – (iv) occurs at two different timescales and the peak broadens as a result. In the figure, the broadening effect caused by a spatial variation in boundary viscosity in system (ii) is more

significant than that caused by non-uniform grain size in system (iii) because the difference in timescale is larger in the former.

φ	$\max_\omega \mathcal{L}$			
	(i)	(ii)	(iii)	(iv)
5°	1.300	1.200	0.773	0.698
15°	0.288	0.242	0.148	0.123
30°	0.049	0.037	0.024	0.020
45°	0.000	0.000	0.000	0.000
60°	0.079	0.058	0.038	0.033

Table 6.2: Maximum mechanical loss $\mathcal{L}$ for systems (i) – (iv) with φ as a parameter. For definition of systems (i) – (iv), see Figure 6.7.

Besides broadening the peak, the presence of multiple sliding frequencies within a system also cause the peak to weaken because the amount of sliding along an interface is constrained by the slip along the adjacent interface. Consequently, the response is controlled by the interface having a smaller sliding frequency. This result is evident in the figure where the peak is consistently located close to the smaller of the two sliding frequencies in systems (ii) – (iv).

Here, we note that according to the definition of the mechanical loss given in (3.13), the peak magnitude is invariant to both boundary viscosity and grain size if these two quantities are constant in a sample. When these two quantities change entirely within a system, the loss spectrum simply shifts along the frequency axis and remains self-similar to a Debye peak. Thus, the weakening of the loss peak found here is caused purely by a spatial variation in grain size and in boundary viscosity; and the amount of weakening depends on the degree of variation, as well as the distribution of these two quantities within a system.

In Table 6.2, we give, for different slope angles φ, the numerical values of the maximum mechanical loss $\mathcal{L}$ in systems (i) – (iv). Except at $\varphi = 45°$ when the systems are under simple shear as discussed in §6.1.1, we find that, in system (iii), where grain size is non-uniform, the loss peak decreases by about 50% when compared to system (i) with uniform grain size and boundary viscosity. That decrease is insensitive to slope angle φ. By contrast, the weakening effect caused by a non-uniform viscosity interface is stronger when the slope angle φ is large. In system (ii) with slope angle $\varphi = 60°$, the loss peak decreases by about 25% when viscosity varies spatially by an order of magnitude; whereas

at $\varphi = 5°$, we find that the peak only decreases slightly by about 8%. Combining these two effects in system (iv), the loss peak can decrease up to about 60%.

6.4   Summary

We now summarize our findings on the sensitivity of the mechanical loss spectrum of elastically–accommodated grain boundary sliding to (i) variation in boundary viscosity, (ii) rounding of corners and (iii) variation in grain size, all obtained using the bicrystal model. The effects due to these factors are as follows:

(a) When boundary viscosity η varies by an order of magnitude across adjacent interface, the loss peak becomes significantly broader and its magnitude is reduced. According to Table 6.2, the loss peak decreases up to about 25% and the amount of reduction depends on the interface slope angle φ.

(b) When corners are made sharper, the loss peak remains self-similar to a single Debye peak and weakens. That effect becomes insensitive to the rounding of corners once the corner radius is less than a tenth of the wavelength of the spatially periodic interface (i.e. $N > 10$). For a type S interface with slope angle $\varphi = 30°$, the loss peak decreases by about 30% when an interface with corner radius about a tenth of the wavelength is replaced with one that has infinitely sharp corners.

(c) When the grain size d is non–uniform, the loss peak weakens. A fourfold variation in grain size roughly halves the peak height which remains nearly self–similar to a single Debye peak.

Our results, thus suggests, that it is unlikely, that all three factors can produce a reduction of the peak magnitude (of several decades) that is require to completely eliminate the peak when timescales are widely separated as shown in Figure 5.3a and Figure 5.4a. Even when these factors are combined (see Table 6.2), the bicrystal model only predicts a reduction less than a decade. We therefore conclude that unless other physical processes enter into the system, the effect of elastically–accommodated grain boundary sliding should be easily observed in the experiments if the timescales are widely separated i.e. $t_\eta \ll t_D$ and the samples are oscillating near the effective sliding frequency t_η^{-1}.

Chapter 7

Conclusion

We have made the numerical calculations for the bicrystal model of diffusionally–accommodated grain boundary sliding and elastically–accommodated grain boundary sliding using a finite slope interface, and our results are consistent with the analytical constraints derived by us.

We show that the general structure of the mechanical loss spectrum predicted in the small–slope analysis when timescales are widely separated i.e. $\mathcal{M} \ll 1$ is preserved even at finite–slope. The key features found in the spectrum for a bicrystal having finite–slope interface are as follows:

(a) a slowly–varying region in the mechanical loss spectrum that is an outcome of corner stress concentration. The mechanical loss scaling in this region can be described by $\mathcal{L} \sim \omega^{\alpha}$, where the power–law exponent α is sensitive slope angle and is constrained within $-2/3 \leq \alpha < 0$. For the two orthogonal sliding modes found in an array of hexagonal grains, the mechanical loss $\mathcal{L}$ varies approximately as $\omega^{-0.3}$. When corner angle varies along an interface, the slope in the mechanical loss spectrum decreases with increasing frequency.

(b) a mechanical loss peak that stands out from the absorption (or high temperature) background. The mechanical loss peak is self–similar to a Debye peak and can be weaken moderately by an increase in corner radius, a variation in boundary viscosity η along the interface and a variation in grain size. The peak can also be broaden significantly when η varies along the interface.

Because triple junctions of the polycrystalline samples used in the experiments are sharp i.e. $N \geq 200$, our result suggests that the mild frequency dependence of the mechanical loss $\mathcal{L}$ that is observed in the experiments on finely grained mantle mineral is likely to be caused by corner stress concentration. Two of our results support that argument. First, our predicted scaling in the slowly–varying region for the two orthogonal modes found in an array of hexagonal grains is close to that observed experimentally [18], [13], [40]. Second, our prediction that the slope in the mechanical loss spectrum decreases gradually with frequency when corner angles vary along an interface is also consistent with experiments.

Despite being able to predict the mechanical loss scaling seen in the experiments, the bicrystal model is not sufficient to predict the magnitude of loss found in the experiments. Comparison with experiment (see Figure 5.9) shows that the bicrystal model under predicted by the mechanical loss for the two sliding modes found in an array of hexagonal grains mechanical loss; a result that is expected because the bicrystal model does not account for the concurrent sliding along multiple planes. Model that accounts for the concurrent sliding along multiple planes is therefore necessary to predict the magnitude of the mechanical loss found in experiment.

7.1 Future extension of current work

We now describe briefly some of the directions one may undertake to extend the current work.

(a) *Models having a more realistic geometry to address the limitations of the bicrystal model.* As stated above, the model should be able to account for the concurrent sliding along different interfacial geometries in polycrystal to predict the magnitude of the mechanical loss $\mathcal{L}$ seen in experiments.

(b) *Homogenization techniques to obtain an effective mechanical loss scaling for polycrystalline solids.* Because triple junction angles are not constant and vary randomly within a sample, a homogenization model of diffusionally–accommodated grain boundary sliding will be useful to determine the aggregate effect of the corner stress concentrations (which depend on corner angles) on the mechanical loss spectrum. Naively, one can expand a model iteratively with some random grain boundaries geometry of

constant mean grain size until the loss spectrum becomes insensitive to the expansion to obtain the homogenized loss spectrum.

(c) *Singular basis shape function in finite element method for fast computation.* Due to corner stress concentration, conventional finite element requires a very fine corner mesh to capture that rapid behaviour of stress with distance. Consequently, accurate results require large amount of memory and long computation time. By using singular basis shape functions near corners, one can reduce the required corner mesh density and speed up the computation.

Bibliography

[1] S.-i. Karato A. Shito and J. Park. Frequency dependence of q in earth's upper mantle inferred from continuous spectra of body waves. *Geophys. Res. Lett.*, 31:L12603, 2004.

[2] M.F. Ashby. Boundary defects and atomistic aspects of boundary sliding and diffusional creep. *Surf. Sci.*, 31:498–542, 1972.

[3] A. Barnhoorn, I. Jackson, J.D. Fitz Gerald, and Y. Aizawa. Suppression of elastically accommodated grain–boundary sliding in high–purity MgO. *J. Eur. Ceram. Soc.*, 27:4697–4703, 2007.

[4] D. R. Bland. *The theory of linear viscoelasticity*. PERGAM, 5th edition, 1960.

[5] J.H. Bunton. *The impact of grain size on the shear creep and attenuation behaviour of polycrystalline olivine*. University of Wisconsin–Madison, 2001.

[6] F. Cammarano, B. Romanowicz, L. Stixrude, C. Lithgow-Bertelloni, and W. Xu. Inferring the thermochemical structure of the upper mantle from seismic data. *Geophys. J. Int.*, 179:1169–1185, 2009.

[7] R.L. Coble. A model for boundary diffusion controlled creep in polycrystalline materials. *J. Appl. Phys.*, 34(6):1679–1682, 1963.

[8] R. F. Cooper. Seismic wave attenuation: Energy dissipation in viscoelastic crystalline solids. *Reviews in Mineralogical Society of America*, 51:253–290, 2002.

[9] U.H. Faul, J.D. Fitz Gerald, and I. Jackson. Shear wave attenuation and dispersion in melt bearing olivine polycrystals: 2. microstructural interpretation and seismological implications. *J. Geophys. Res.*, 109(B06202):doi:10.1029/2003JB002407, 2004.

[10] U.H. Faul and I. Jackson. Diffusion creep of dry, melt–free olivine. *J. Geophys. Res.*, 112(B04202):doi:10.1029/2006JB004586, 2007.

[11] H.J. Frost and M.F. Ashby. *Deformation–Mechanism maps*. Pergamon Press, 1982.

[12] F. Ghahremani. Effect of grain boundary sliding on anelasticity of polycrystal. *Int. J. Solids Struct.*, 16:825–845, 1980.

[13] T. T. Gribb and R. F. Cooper. Low–frequency shear attenuation in polycrystalline olivine: Grain boundary diffusion and the physical significance of the andrade model for viscoelastic rheology. *J. Geophys. Res.*, 103(B11):27267–27279, 1998.

[14] Y. Gung and B. Romanowicz. *Q* tomography of the upper mantle using three–component long period waveforms. *Geophys. J. Int.*, 157:813–830, 2004.

[15] M. Ishii and J. Tromp. Normal-mode and free-air gravity constraints on lateral variation in velocity and density of earth's mantle. *Science*, 285:1231–1236, 1999.

[16] I. Jackson, U.H. Faul, J.D. Fitz Gerald, and S.J.S Morris. Contrasting viscoelastic behaviour of melt–free and melt–bearing olivine: Implications for the nature of grain boundary sliding. *Mater. Sci. Eng., A*, 442:170–174, 2006.

[17] I. Jackson, U.H. Faul, J.D. Fitz Gerald, and B.H. Tan. Shear wave attenuation and dispersion in melt bearing olivine polycrystals: 1. specimen fabrication and mechanical testing. *J. Geophys. Res.*, 109(B06201):doi:10.1029/2003JB002406, 2004.

[18] I. Jackson, J.D. Fitz Gerald, U.H. Faul, and B.H. Tan. Grain–size–sensitive seismic wave attenuation in polycrystalline olivine. *J. Geophys. Res.*, 107(B12):2360, doi:10.1029/2001JB001225, 2002.

[19] I. Jackson and M.S. Paterson. A high–pressure, high–temperature apparatus for studies of seismic wave dispersion and attenuation. *Pure appl. geophys.*, 141(445–466), 1993.

[20] S. I. Karato. *The dynamic structure of the deep earth*. Princeton University Press, 2003.

[21] S. I. Karato. *Deformation of earth materials*. Cambridge University Press, 2008.

[22] T.S. Kê. Experimental evidence of the viscous behaviour of grain boundaries in metals. *Phys. Rev.*, 71(8):533–546, 1947.

[23] T.S. Kê. Fifty–year study of grain–boundary relaxation. *Metall. Mater. Trans. A*, 30A:2267–2295, 1999.

[24] J.F. Lawrence and M.E. Wysession. QLM9: A new radial quality factor Q_μ model for the lower mantle. *Earth Planet Sc. Lett.*, 241:962–971, 2006.

[25] J.B. Minster and O.L. Anderson. A model of dislocation controlled rheology for the mantle. *Philos. Trans. R. Soc.*, 299:319–356, 1981.

[26] S.J.S Morris and I. Jackson. Diffusionally-assisted grain boundary sliding and viscoelasticity of polycrystals. *J. Mech. Phys. Solids*, 57(4):744–761, 2009.

[27] S.J.S Morris and I. Jackson. Implications of the similarity principle relating creep and attenuation in finely grained solids. *Mater. Sci. Eng., A*, 521–522:124–127, 2009.

[28] D.R. Mosher and R. Raj. Use of the internal friction technique to measure rates of grain boundary sliding. *Acta Metall.*, 22(12):1469–1474, 1974.

[29] A.S. Nowick and B.S. Berry. *Anelastic relaxation in crystalline solids*. Academic Press, 1972.

[30] R. O'Connell and B. Budiansky. Measures of dissipation in viscoelastic media. *Geophys. Res. Lett.*, 5:5–8, 1978.

[31] G. Pezzotti. Internal friction of polycrystalline ceramic oxides. *Phys. Rev. B: Condens. Matter*, 60(6):4018–4029, 1999.

[32] G. Pezzotti, K. Ota, and H.-J. Kleebe. Grain boundary relaxation in high-purity silicon nitride. *J. Am. Ceram. Soc.*, 79(9):2237–2246, 1996.

[33] C. R. Picu and V. Gupta. Stress singularities at triple junctions with freely sliding grains. *Int. J. Solids Struct.*, 33(11):1535 – 1541, 1996.

[34] R. Raj. Transient behaviour of diffusion-induced creep and creep rupture. *Metall. Trans. A*, 6:1499 – 1509, 1975.

[35] R. Raj and M.F. Ashby. On grain boundary sliding and diffusional creep. *Metall. Trans.*, 2(4):1113–1127, 1971.

[36] A.E. Ringwood. *Composition and Petrology of the earth's mantle*. McGraw-Hill, 1975.

[37] R. Schaller and A. Lakki. Grain boundary relaxation in ceramics. *In: Mechanical Spectroscopy 2001, Material Science Forum*, 366-368:315–340, 2001.

[38] J.A. Sethian and J. Wilkening. A numerical model of stress driven grain boundary diffusion. *J. Comput. Phys.*, 193:275–305, 2003.

[39] A. Shito, S. Karato, K. Matsukage, and Y. Nishihara. Towards mapping the three–dimensional distribution of water in the upper mantle from velocity and attenuation tomography. *In: Earth's Deep Water Cycle, eds. S. Jacobsen & S. van der Lee, AGU Monograph*, pages 225–236, 2006.

[40] M. Sundberg and R.F. Cooper. A composite viscoelastic model for incorporating grain boundary sliding and transient diffusion creep; correlating creep and attenuation response for materials with a fine grain size. *Philos. Mag.*, 90(20):2817–2840, 2010.

[41] J. Wilkening, L. Borucki, and J.A. Sethian. Analysis of stress–driven grain boundary diffusion. Part I. *SIAM J. Appl. Math.*, 64:1839–1863, 2004.

[42] O. C. Zienkiewicz and R. L. Taylor. *The Finite Element Method*, volume 1. McGraw Hill Book Company, London, 5th edition, 2000.